Taylor & Francis
Taylor & Francis Group

Quantum cascade transitions in nanostructures

TAPASH CHAKRABORTY[1]* and VADIM M. APALKOV[2]†

[1]Institute of Mathematical Sciences, Chennai 600 113, India
[2]University of Utah, Physics Department,
Salt Lake City, UT 84112-0830, USA

Abstract

In this article we review the physical characteristics of quantum cascade transitions (QCTs) in various nanoscopic systems. The quantum cascade laser which utilizes such transitions in quantum wells is a brilliant outcome of quantum engineering that has already demonstrated its usefulness in various real-world applications. After a brief introduction to the background of this transition process, we discuss the physics behind these transitions in an externally applied magnetic field. This has unravelled many intricate phenomena related to intersubband resonance and electron relaxation modes in these systems. We then discuss QCTs in a situation where the quantum wells in the active regions of a quantum cascade structure are replaced by quantum dots. The physics of quantum dots is a rapidly developing field with its roots in fundamental quantum mechanics, but at the same time, quantum dots have tremendous potential applications. We first present a brief review of those aspects of quantum dots that are likely to be reflected in a quantum-dot cascade structure. We then go on to demonstrate how the calculated emission peaks of a quantum-dot cascade structure with or without an external magnetic field are correlated with the properties of quantum dots, such as the choice of confinement potentials, shape, size and the low-lying energy spectra of the dots.

Contents

*Author for correspondence. e-mail: tapash@imsc.res.in
†e-mail: apalkov@physics.utah.edu

1. Introduction

Nanoscale science and technology are rapidly developing fields which have emerged around the premise that new materials, devices and systems can be created through control of matter on the nanometre length scale. In the last couple of decades, rapid advances in microfabrication technology have allowed laboratories around the world to routinely fabricate ultrathin structures with effects dominated by quantum physics. The field of nanostructured systems is exceedingly rich with a multitude of possibilities to explore many enticing physical systems. The turning point in our understanding of nanometre-scale electronic properties was the development of atomically precise heterojunctions with which various nanostructured systems are made. In 1994, Capasso *et al.* invented a novel laser known as the quantum cascade laser (QCL) based on such a nanostructured system. The properties of this new laser depend upon having appropriate control of the electron motion through a system created by molecular beam epitaxy (MBE). In the ensuing years of hectic activities that followed, this laser has proven to be a most powerful and extremely useful device for a wide range of applications. In its classic design, the mechanism of photon generation is based upon transitions between quantized conduction band excited states (intersubband transitions) of coupled quantum wells
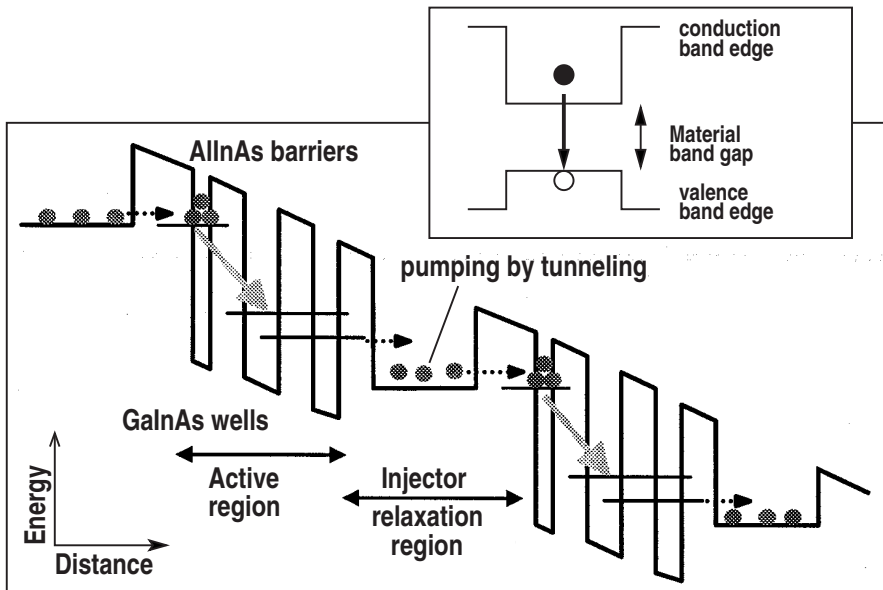
Figure 1. Schematic picture of the functioning of a conventional semiconductor laser and the quantum cascade transition (QCT) scheme for a QC laser. In the standard lasing process (top inset) a photon is generated from recombination of an electron (●) with a hole (○). In the QCL, the conduction band profile is engineered to have staircase-like structures in an applied voltage. The horizontal line in each quantum well corresponds to the lowest energy subband and the location of the energy level is related to the thickness of the well. In the active regions, each consisting of three quantum wells, electrons cascade down the energy levels (transition from the top level to the intermediate level) emitting photons in the process and tunnel through the barriers to the injector/relaxation regions that isolate the active regions. The active regions usually number 25–75 in a QCL device.

characterized by an ultrashort excited state lifetime that is limited by electron–longitudinal optical (LO) phonon scattering, and on electron resonant tunnelling as the pumping mechanism (figure 1). The population inversion between the states of the laser transition is designed by reducing the final state lifetime using resonant optical phonon emission and by suppressing tunnelling from the excited states via an electron Bragg reflector [1–4].

Unlike in conventional semiconductor lasers where the light originates from recombination of electrons and holes across the energy gap that exists between the conduction band and valence band of the crystal (figure 1), in QC lasers the wavelength is essentially determined by quantum confinement, i.e. by the thickness of the active region layer rather than by the bandgap of the material. The advantage of this is that the laser wavelength can be tailored over a wide range using the same heterostructure material. Since the initial report of QC lasers in 1994 [1, 2], emission wavelengths in the 3.4–13 μm range have been achieved [5, 6], using AlInAs–GaInAs heterostructures grown by MBE on InP substrates. High power operation of mid-infrared (mid-IR) QC lasers at room temperature or even above room temperature was also reported [7, 8]. These high optical powers are a direct consequence of the cascade scheme because an electron, after it has emitted a laser photon in the first active region of the device, is reinjected into the next stage that follows, where it

emits another photon. Therefore, an injected electron creates, in principle, N_{st} laser photons as it traverses the device. Here N_{st} is the number of stages.

Since its very first demonstration in 1994 by Capasso *et al.*, the QCL has undergone very rapid development. Room temperature operation has been reported in pulsed operation in the range 3.6–11.5 μm, with extremely high output powers up to half a watt [9, 10]. In the 5–8 μm wavelength region continuous wave operation at $T > 120$ K produces output power of 2–20 mW and ~ 200 mW at $T = 80$ K [10]. Near (and above) room temperature, QCLs operate only in pulsed mode. Recently, pulsed operation up to 425 K for wavelengths of ~11 μm has been reported in QCLs, and this has yet to be demonstrated by any other semiconductor laser [11]. In section 2, we present a brief account of the physics of intersubband transitions in quantum wells, which is the primary mechanism behind this laser. This is a well-researched and well-reviewed topic and we touch upon only those aspects that are relevant for our main topic of review—quantum cascade transitions (QCTs) in nanostructured systems. In section 3, we briefly review the fundamentals of the QCT as applied to a quantum-well based QCL. We begin by describing the basic working principles of the laser device and discuss some of the latest developments in design and performance. We then discuss the vast potential applications of QCLs where they surpass most other semiconductor lasers. In section 4, we explain the role of disorder on QCT and describe the QCT in some novel situations, viz. application of an external magnetic field that is parallel, tilted, or perpendicular to the electron plane. Work on magneto-transport and magneto-optical measurements and their interpretation in terms of various relaxation processes is also presented in this section. Section 5 provides a brief background on quantum dots.[1] These atom-like devices are of great interest because of their spectrally sharp energy levels and other 'atomic' properties. We explain how these dots are made and the physics that emerge from application of an external magnetic field. We also present a brief list of the application potentials of QDs. Section 6 describes the theoretical results available as yet on QCTs in quantum-dot cascade structures (QDCSs). We describe the physical properties of these systems and demonstrate the dependence of the optical properties of QDCSs on the size and shape of the quantum dots. Some of the physical properties of quantum dots, such as shell filling, magic numbers, etc. are also expected to be present in a QDCS. We describe how these atom-like properties of QDs profoundly influence the luminescence spectra of QDCSs. We conclude in section 7 with a brief look at the open questions and theoretical challenges that lie ahead in our understanding and application of the QCT in nanostructured systems. We wish to point out that in this article we do not intend to review the development of QCL devices. Our intention here is primarily to highlight the interesting physical properties associated with the QCT. Readers looking for a more up-to-date review of the technical aspects of the QCL should refer to [14].

2. Intersubband transitions in quantum wells

In the last couple of decades, rapid progress in growing high-quality quantum well (QW) structures has allowed researchers to investigate unique phenomena associated

---

[1]Reviews of the physical properties of QDs are already available in the literature (see for example [12, 13]). Section 5 highlights some of the properties of QDs that are expected to be relevant for cascade structures with QDs in the active regions.
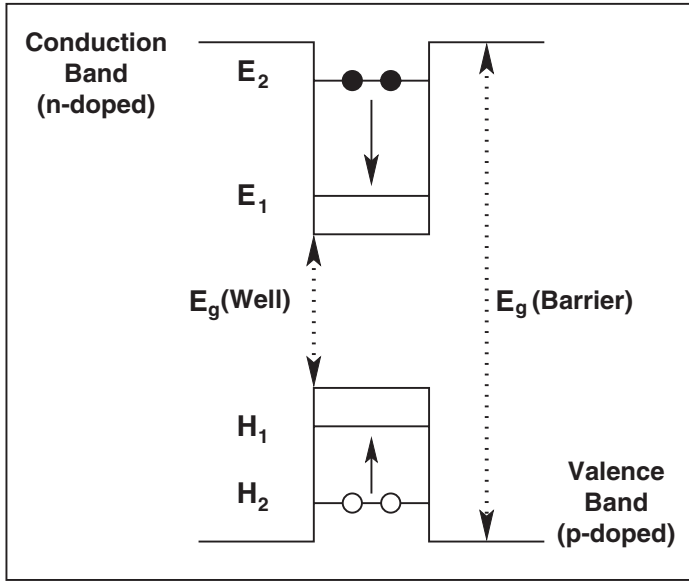
Figure 2.   Schematic of a quantum well and the intersubband emission between quantized energy levels for electrons E_1 and E_2, or for holes H_1 and H_2 in the well. These quantized energy levels can be tuned by adjusting the quantum well width and thickness.

with quantum confinement in these structures. Intersubband transitions in QW structures is a case in point, since they have been very successfully applied to novel devices such as QW infrared photodetectors [15] and the quantum cascade laser, the subject of the present review. As we shall see below, the large oscillator strength of the transition and the possibility of controlling the resonance by structural parameters of the QW, viz. its width and barrier height, make it attractive for engineering opto-electronic devices based on these transitions [16, 17].

Intersubband transitions occur between energy levels within the same conduction or valence band (intraband transitions), as shown schematically in figure 2. These energy levels arise from confinement of electron motion in QWs of low-bandgap material (e.g. GaAs) sandwiched between layers of a higher-bandgap semiconductor (e.g. $Al_xGa_{1-x}As$) [18, 19]. The energy levels of an electron in a well between two walls of infinite extent and parabolic bands are

$$E_n = \left(\frac{\hbar^2\pi^2}{2m^*L_w^2}\right)n^2$$

where L_w is the width of the QW, m^* is the effective mass in the well and n is an integer. These energies correspond to the motion of the electron across the plane. Electron motion in the plane is that of a free particle. The intersubband transition energy between the lowest and first excited states is then

$$E_{21} = E_2 - E_1 = \left(\frac{3\hbar^2\pi^2}{2m^*L_w^2}\right).$$

The dipole matrix element for this transition

$$\langle z \rangle = 16 L_{\mathrm{w}}/9\pi^2 \simeq 0.18 L_{\mathrm{w}}$$

is large [18]. The oscillator strength corresponding to this transition

$$f \equiv \frac{2m^*}{\hbar^2}(E_2 - E_1)\langle z \rangle^2 \simeq 0.96$$

is also very large [18]. By changing the QW width L_{w}, the intersubband transition energy can be varied over a wide range.

At high electron densities, usually present in semiconductor QWs and hetero-structures, many-body effects are important. The effect of electron–electron interactions on intersubband transitions have been a long-standing active area of research [17, 20]. The interelectron interaction affects the resonance energy in two ways [21]:

- The resonance energy is shifted by the energy difference $E_{21} = E_2 - E_1$ between the ground subband and the excited subband due to collective excitations of the electron gas in the QWs (the plasmon mode). This is the well-known depolarization shift.
- The exciton interaction arises from the interaction of an excited electron with the hole in the Fermi sea it leaves behind. This has a tendency to decrease the resonance energy. This effect is, however, much smaller than the first effect in GaAs QWs.

Usually the intersubband transitions are studied experimentally by light absorption or by creating quasi-equilibrium electron distributions where a number of electrons are located in the second subband of a QW. In the latter case the intersubband transitions result in relaxation of the electron system. Electron relaxation in quantum wells has been the subject of intensive theoretical and experimental research. Understanding the nature of these processes is important both for analysing the fundamental physical behaviour and for technological applications. The relaxation processes with emission of a photon are the most important in QCL systems. Such processes occur with the conservation of the in-plane electron momentum and the energy of the emitted photon is equal to the difference of the energy of the lowest two subbands, E_{12}. The typical relaxation time due to this processes is about 1 ns. Although the optical transitions in a QCL are the main concern, the main relaxation processes have a different origin. The main mechanisms that are responsible for intersubband electron relaxation in QWs are: (i) emission of longitudinal optical phonons, (ii) emission of acoustical phonons, and (iii) electron–electron or electron–impurity scattering.

The general expression for the electron relaxation rate follows from Fermi's golden rule:

$$\tau_r^{-1} = \frac{2\pi}{\hbar} \sum_f |\langle \psi_i | V_{\mathrm{int}} | \psi_f \rangle|^2 \delta(E_f - E_i - \hbar\omega). \tag{1}$$

Relaxation occurs in the form of a transition from the initial state $\langle \psi_i |$ of the second subband into the final state $\langle \psi_f |$ of the first subband. The potential V_{int} determines the mechanism of relaxation and the energy $\hbar\omega$ stands for the energy of emitted phonon in the case of inelastic scattering. The wave functions of the electron in the initial and final states have the form $\chi_{i(f)}(z)\exp(i\mathbf{k} \cdot \boldsymbol{\rho})$, where $\chi_{i(f)}(z)$ is the envelope

wave function of the electron in the second (initial) and the first (final) subbands, respectively, and **k** is the two-dimensional electron wave vector.

Electron–impurity scattering is an elastic process and in the case of interaction with ionized impurities the interaction potential is given by

$$V_{int}(\rho, z) = \frac{2\pi e^2}{\varepsilon \mathcal{A}} \sum_i \sum_{\mathbf{Q}} \frac{1}{Q} \exp(-Q|z - z_i|) \exp[i\mathbf{Q} \cdot (\boldsymbol{\rho} - \boldsymbol{\rho}_i)], \tag{2}$$

where $\mathcal{A}$ is the sample area, $(\boldsymbol{\rho}_i, z_i)$ is the impurity position and ε is the effective dielectric constant.

The electron–phonon interaction potential has the form

$$V_{int}(\rho) = -\sum_{\mathbf{Q}} \frac{M(\mathbf{Q})}{\sqrt{V}} \left[\exp(i\mathbf{Q} \cdot \mathbf{r}) b_{\mathbf{Q}}^+ + c.c. \right], \tag{3}$$

where $b_{\mathbf{Q}}^+$ and $b_{\mathbf{Q}}$ are the creation and annihilation operators of a phonon with wave vector $\mathbf{Q}$, and V is the normalization volume. The strength of the electron–phonon interaction in the isotropic approximation is given by the expression

$$|M(\mathbf{Q})|^2 = 2\pi \hbar \omega_{LO} \frac{e^2}{Q^2} \left(\frac{1}{\varepsilon_\infty} - \frac{1}{\varepsilon_0} \right) \tag{4}$$

for optical (LO) phonons, where ε_∞ and ε_0 are the high-frequency and low-frequency permittivities of the system, and

$$|M(Q)|^2 = \frac{\hbar}{2\rho_0 s Q} \left[\beta^2 + \Xi_0^2 Q^2 \right], \tag{5}$$

for acoustical phonons, where ρ_0 is the mass density, β and Ξ_0 are the parameters of the piezoelectric and deformation potential couplings, respectively, and s is the speed of sound.

The optical phonons are assumed to be dispersionless with frequency ω_{LO} and for acoustic phonons usually the Debye approximation with the linear dependence of the phonon frequency on the wave vector, $\omega(Q) = sQ$, is used. The (x, y)-component of the electron wave function results in conservation of in-plane momentum, while the z-component of the wave function gives the form factor $Z(Q_z)$,

$$Z(Q_z) = \int dz\, e^{iQ_z z} \chi_i(z) \chi_f(z). \tag{6}$$

In calculating the relaxation rates, the influence of the heterojunctions or multiwell structures on the phonon dispersion law and on the strength of the electron–phonon interaction is usually disregarded.

When electron relaxation due to emission of LO phonons is allowed in quantum wells it is the leading relaxation mechanism in such systems. The relaxation time in this case is of the order of 1 ps [22–25] and the experimental results for the value of the relaxation time are in good agreement with theoretical predictions. This case is realized in QCL structures, where the quantum wells are narrow enough. The energies of the electron in the initial and final states differ by the LO phonon energy, which in GaAs is about 36 meV.

A more interesting situation occurs in wider quantum wells where the separation between subbands is smaller than the LO-phonon energy. As a result, direct emission of LO phonons is forbidden. Then the dominant mechanism of intersubband electron relaxation is the acoustic phonon interactions or electron–electron scattering [26, 27], which can yield a much longer electron relaxation time compared to the case of narrow quantum wells [22, 28]. A wide range of relaxation times, from about 2 ps to 1000 ps, has been reported experimentally. The relaxation time in this case has a strong dependence on the electron temperature. This is because the temperature tails in the electron distribution in the second subband can open the channel for electron intersubband transitions with emitting LO phonons [29–31]. As a result a transformation of the relaxation mechanism from emission of acoustic phonons to emission of LO phonons can be observed with increasing temperature, and fast relaxation can be achieved at high temperature. QCL structures in which the LO-phonon relaxation mechanism is energetically forbidden will emit light in the terahertz region (1–10 THz) [32]. Recently such devices have been fabricated experimentally [33, 34]. Here the relaxation mechanism in the active region was dominated by the carrier–phonon scattering processes, which gives a lifetime of the order of 1 ps for the electron non-radiative relaxation transition from the upper subband to the lower subbands of the active region.

Another important effect in quantum well structures is the influence of the electric field applied in the growth direction on the intersubband transition rate. This problem becomes especially important for QCLs, which are designed to operate in an external electric field. The main influence of the electric field on the relaxation time is through the deformation of the carrier wave functions [22]. This results in a strong increase of the intersubband relaxation time for both multiple quantum well structures and for a single quantum well. Finally, when a magnetic field is applied perpendicular to the electron plane of a quantum well, each subband is quantized into a ladder of discrete Landau levels. The situation is different when the magnetic field is applied parallel to the electron plane or tilted from the direction perpendicular to the plane. The cyclotron and subband energies are then coupled. These cases will be discussed in detail in section 4.

3.   Quantum cascade transitions

As mentioned earlier, the QC laser is the first semiconductor structure to utilize intersubband transitions from a cascade structure[2] for laser action [1, 2]. The original device of Capasso *et al.* consisted of 25 radiative stages, each stage containing an active region with three quantum wells. The lasing for this device was 4.2 μm ($T < 100$ K).

3.1. *Basic principles*

The QCT takes place in the discrete electronic states due to quantum confinement, normal to the electron plane in the quantum wells. The electron motion is free in the plane and therefore the electronic states correspond to plane waves. The energy subbands being almost parallel, photons released due to radiative transitions

[2]The original work on QCLs was in fact largely motivated by an earlier proposal [35], where the possibility of light amplification in intersubband transitions from a cascade structure [36] was discussed theoretically.
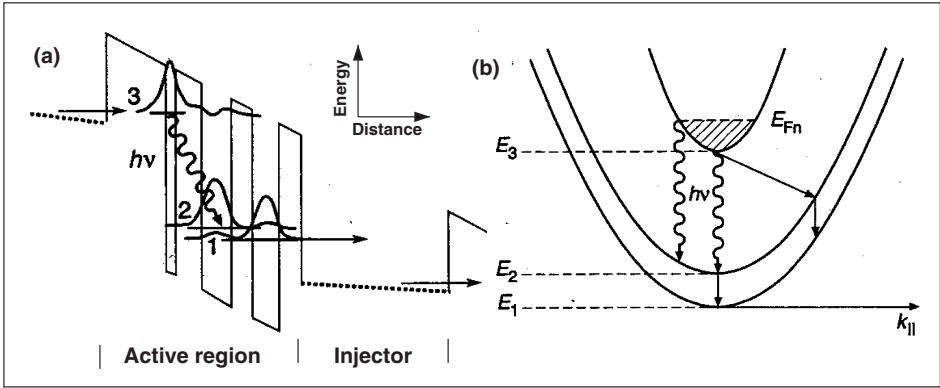
Figure 3. (*a*) The active region of the quantum-well cascade laser of Capasso *et al*. [1], depicting a QCT between two energy levels. (*b*) Energy versus the in-plane wave vector corresponding to the process in (*a*). Only the lowest subbands of the quantum wells are shown here, where the bottom of the subbands correspond to the energy levels indicated in (*a*).

of electrons to a lower subband (say, from $n = 3$ to $n = 2$) will all have the same frequency ν with energy $h\nu = E_3 - E_2$.

Proper design of the active layers is a vital step for the QCT. In order to generate the proper transition energies, transition probabilities and transport characteristics, one must carefully choose the layer thicknesses. The conduction band energy diagram of a portion (active region and injector) of the QC laser where the very first results were reported is shown in figure 3(*a*). Application of a voltage of appropriate polarity changes the conduction band diagram into a staircase shape. Electrons are injected through an AlInAs barrier into the $n = 3$ energy level of the quantum well (GaInAs). The *population inversion* between the $n = 3$ state and the $n = 2$ state of the quantum well separated by an AlInAs barrier from the former QW is achieved by the reduced spatial overlap between these states and is also due to the strong coupling to an adjacent GaInAs well through the AlInAs barrier. The moduli squared of the relevant wave functions are also shown in figure 3(*a*). The third QW is responsible for strong inelastic relaxation by means of optical phonons with nearly zero momentum transfer between the $n = 2$ and $n = 1$ subbands. Finally, electrons tunnel out of the $n = 1$ state at an extremely fast rate, thereby enhancing the population inversion. Electrons relax in the injector regions and are then injected by tunnelling into the $n = 3$ excited state of the next active region and the whole process is repeated.

The energy dispersion of the $n = 1, 2$ and 3 states parallel to the electron plane in the active regions is shown schematically in figure 3(*b*). The energy levels $n = 1, 2, 3$ are in fact the bottom of these subbands. The wavy arrows denote radiative transitions originating from the filled region (shaded) of the $n = 3$ state. They are essentially of the same wavelength. The intersubband optical-phonon scattering processes are indicated by the straight arrows. The relaxation processes with near-zero momentum transfer between the $n = 1$ and $n = 2$ subbands are very fast (subpicosecond). The laser transition is diagonal in real space, i.e. between states with reduced spatial overlap. This increases the lifetime of the upper state and also decreases the escape rate of electrons into the continuum. A third state, located approximately one phonon energy below the lower state of the lasing transition, is

added. The resonant nature of the optical phonon emission between these two states reduces the lifetime of the lower one to about 0.6 ps.

3.1.1. *Minibands and minigaps*

The injector (relaxation) regions consist of a multilayer structure, or superlattice, with QWs coupled by very thin barriers. As a result, the electronic states extend over many layers and form *minibands* separated by minigaps. These minigaps prevent the electron from tunnelling out of the $n = 3$ state. This dramatically enhances the electron lifetime in this state. At the other end of the active region, the design of the superlattice injector allows fast extraction of electrons from the active region, since a miniband faces the energy levels $n = 2$ and $n = 3$. The photons that are generated in the process are held and directed by a surrounding waveguide material. The waveguide geometry is similar to that used in conventional semiconductor lasers. Details are available in [37, 14]. The relevant material parameters for the $Ga_{0.47}In_{0.53}As/Al_{0.48}In_{0.52}As$ coupled-well structure are: conduction band discontinuity $\Delta E_c = 0.52$ eV, $m_e^*(GaInAs) = 0.043 \ m_0$; $m_e^*(AlInAs) = 0.078 \ m_0$. The non-parabolicity coefficient (the dependence of mass on energy) is $\gamma = 1.3 \times 10^{-18}$ m^2 [38]. These parameter values are important for theoretical studies of the QC structures discussed in the following sections.

3.1.2. *Vertical transitions*

A laser structure based on a vertical transition, i.e. with the initial and final states centred in the same well was first reported in 1995 [3, 4]. Being less sensitive to interface roughness and impurity fluctuations, this type of laser is expected to exhibit a narrower gain spectrum and therefore a lower threshold, provided that the resonant phonon emission scheme is sufficient to obtain a population inversion and that electrons in the upper state can be prevented from escaping into the continuum.

The coupled-well active region was engineered in such a way that at a threshold field, the ground states of the two QWs have anticrossed (figure 4). This leads to a short lifetime between the $n = 1$ and $n = 2$ states as their energy separation is resonant with the optical phonon. The electron lifetime in the $n = 3$ state is longer since from this state the optical phonon emission is associated with a large momentum transfer. The injector/relaxation region is designed to suppress the escape of electrons from the $n = 3$ excited state of the QW into the continuum while allowing their extraction from the lower $n = 1$ state of the well.

3.1.3. *GaAs/AlGaAs quantum cascade lasers*

Until 1998, lasing in QCLs was restricted to a single material system, $Al_{0.48}In_{0.52}AS/Ga_{0.47}In_{0.53}As/InP$. However, in principle, the QCL should not depend on the type of semiconductor system used because here the lasing is entirely due to a fundamental process, the intersubband transitions. In recent years, reports on the fabrication of a unipolar light emitter based on GaAs/AlGaAs systems showing electroluminescence [39–41], optically pumped intersubband lasers [42, 43], and finally, electrically pumped lasing [44], have appeared in the literature. The GaAs/AlGaAs material systems are the most common low-cost semiconductor compounds and are technologically mature materials. Additionally, the crystal structure of GaAs matches perfectly with that of AlGaAs, offering significant flexibility in QC laser design. The device of Sirtori *et al.* [44] operated up to 140 K
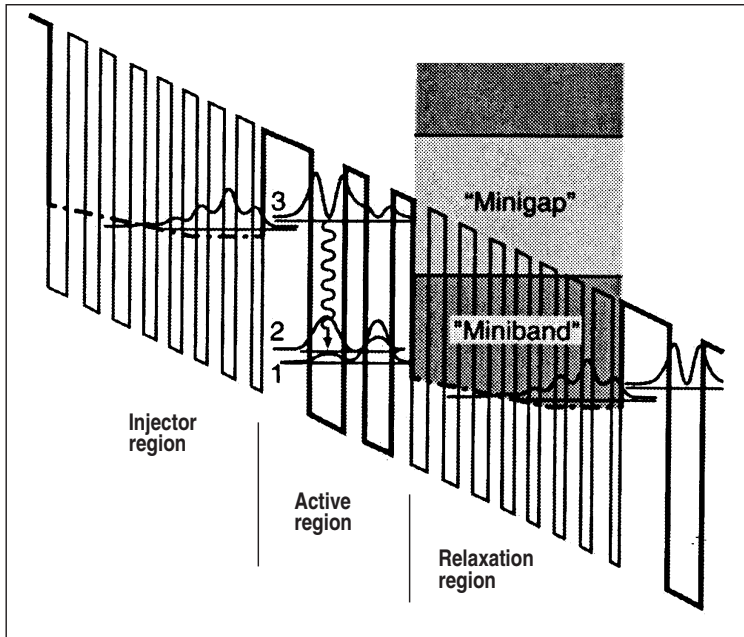
Figure 4. Vertical transitions in the active region of a QC laser [3, 4]. The area labelled 'miniband' indicates the energy range and spatial extent of band-like states. This superlattice is also designed to create a 'minigap' whose role is to block the escape of electrons from level 3.

in the technologically important (8–12 μm) atmospheric window. Keightley *et al.* [45] compared the performance of their GaAs/AlGaAs and InGaAs/AlInAs quantum cascade laser structures. They observed that the threshold current density measured for the GaAs laser exhibits a sudden increase above 100 K, in contrast to the InGaAs laser. Hvozdara *et al.* [46] reported the application of a GaAs-based QCL in gas spectroscopy. As of now, pulsed operation of a GaAs/AlGaAs QCL upto 258 K and emission wavelength of 11.3 μm have been reported [47]. Room temperature (300 K), pulsed mode operation of a GaAs/$Al_{0.45}Ga_{0.55}As$ QC laser based on a conventional three-well active region design and emitting at ≈ 9μm was reported in [48]. A collection of articles on various aspects of QCLs can be found in [49].

3.1.4. *QCLs based on superlattice structures*

Superlattice QC lasers (SL-QCLs) based on optical transitions between conduction minibands have been demonstrated to have several advantages over conventional QCLs in their performance [50–53]. A semiconductor superlattice (SL) comprises a periodic stack of layers of two materials (quantum wells and barriers). The period of these layers is typically much larger (∼ 5 nm) than the lattice constant of the bulk constituent materials (∼ 0.5 nm). It is well known that the external periodic potential splits the conduction and valence bands in a series of minibands that are separated by minigaps, along the direction normal to the layers. The miniband and minigap widths can be controlled by the optimal choice of the layer thicknesses. SL-QCLs with interminiband transitions are best suited for long-

wavelength emission, with wavelengths extending well beyond the atmospheric windows. In the case of conventional QCLs with intersubband transitions, extension to such a long wavelength is very difficult [52]. In interminiband transitions, the lasing action occurs between states at the edge of the first minigap of several SL regions, where electrons are extracted from the lowest miniband of the previous SL and injected into the second miniband of the following one. One major advantage of this process over conventional QCLs, where the carriers are injected into single-electron subbands, is that the wide energy minibands can carry large current densities. A unique feature of SL-QCLs is the high oscillator strength of the radiative transition between the two minibands [50]. Very recently, a GaAs/AlGaAs superlattice QCL was reported to emit at 12.6 μm at temperatures as high as 40°C [54].

3.1.5. *Type-II quantum cascade lasers*

There are also recent reports in the literature of type-II QCLs [55–58] that combine the advantages of a cascade design and the interband transitions of the conventional diode laser. While this type of laser design retains the advantage of carrier recycling, non-radiative relaxation due to optical phonon scattering, which causes severe sample heating and is also believed to be the reason for the high threshold current density in type-I QCLs, can be suppressed. In this design, the conduction band of one semiconductor overlaps the valence band of the adjacent semiconductor. An electron tunnelling between a quantum well in the conduction band of indium arsenide (InAs) and the valence band of indium gallium antimonide (InGaSb) emits a photon and is then re-injected in the next successively connected active region, and so on. The main advantage of this laser is the higher efficiency as compared to the standard QCL. Type-II interband cascade lasers have achieved an efficiency where every electron injected into the laser creates, on average, about six photons, and near-room-temperature operation has also been reported [59]. Intersubband electroluminescence from InAs/GaSb/AlSb type-II structures, grown by MBE, has also been demonstrated [60].

3.1.6. *Recent developments*

Gmachl *et al.* reported a type of QCL that can be operated bidirectionally [61]. Through careful design of the injector region, a tailored asymmetry can generate lasing at two different wavelengths, depending upon the polarity. According to these researchers, this new laser may benefit trace gas analysis in remote sensing applications. Gmachl *et al.* also demonstrated 'tapping' into the cascade by creating a QCL with a heterogeneous cascade [62]. Some of the other recent developments in QCL research are: an intersubband staircase laser [63], Si/SiGe quantum cascade structures [64], and long wavelength (15 μm and 23 μm) GaAs/AlGaAs QCLs [65]. A terahertz laser based on interminiband transitions in a GaAs/AlGaAs heterojunction has been reported [33]. A simulation scheme to model these QCLs has been developed where the carrier–phonon and carrier–carrier interaction mechanisms are taken into account to calculate the current–voltage characteristics [66].

3.2. *Applications: sense-ability and other qualities*

The major success of the QCL is its potential for wide-ranging and important real-world applications. Capasso *et al.* have written several excellent articles [67–70] on the vast application potential of QCLs, in particular, in gas-sensing applications.

There are two optical transmission windows in the atmosphere[3] (3–5 μm and 8–14 μm) where mid-IR optical systems can be used for a wide range of applications. These include military, space and commercial applications. Through these two atmospheric windows QCLs can be used to detect many trace gases and vapours that include chemicals such as CO, CH_4, NH_3, N_2O, SO_2, HCL and HNO_3, and many organic compounds. In the short-wavelength atmospheric window, there are competing systems other than the QCL such as type-II heterostructure and InAsSb interband lasers [72, 73]. However, for the long-wavelength atmospheric window, a QCL is still the only successful device available as yet.

The advantage of the QCL over the conventional semiconductor laser is its increased efficiency. A conventional semiconductor laser producing light by electron–hole recombination can only produce one photon per electron. QCL, on the other hand, generates a photon at every active region and therefore a single electron can produce on average about as many photons as the number of stages in the QCL device. Because of its high power, tuning range and ability to operate at room temperature, the QCL is set to provide an important tool for the detection of minute amounts of gases. Important applications may be in long- and short-range sensing of toxic chemicals or hazardous gases. This can prove useful for law enforcement and military applications, or in non-invasive medical diagnostics (such as a breath analyser) [74]. The QC laser can also be used for mid-IR atmospheric optical communication systems for data transmission through the two transparent atmospheric windows [75, 76]. The QCL is expected to find important applications in space exploration in the form of a QC laser spectrometer [71]. Clearly, the QC laser is a very important breakthrough in the field of laser research, whose application potential is undoubtedly far superior to that of other nanostructured light sources. The laser device is now commercially available.

4. Quantum cascade transitions in novel situations

In the QCL based on quantum well systems described above, electron motion is free along the plane, and energy bands are continuous (figure 3). Various attempts to reduce the dimensionality of the system from two to zero by quantizing the electron motion in the plane have been reported in the literature. The energy spectrum in a zero-dimensional system is fully discrete and in such a situation it is commonly expected that electron–optical-phonon scattering will be suppressed.

4.1. *External magnetic field*

Suppression of intersubband non-radiative transitions in quantum well laser devices by applying a magnetic field perpendicular to the epitaxial layers has been suggested by various authors [77, 78]. The idea is simple: due to the presence of a magnetic field the subbands are quantized into discrete Landau levels. Therefore, by an appropriate choice of the magnetic field strength, one can forbid various non-radiative transition processes (optical [77] and acoustic [78] phonons) due to the new energy conservation requirements.

---

[3]The atmosphere is relatively transparent in these regions and is therefore of great use in detecting small traces of both environmental and toxic gases and vapours down to sensitivities of parts per billion in volume [71].
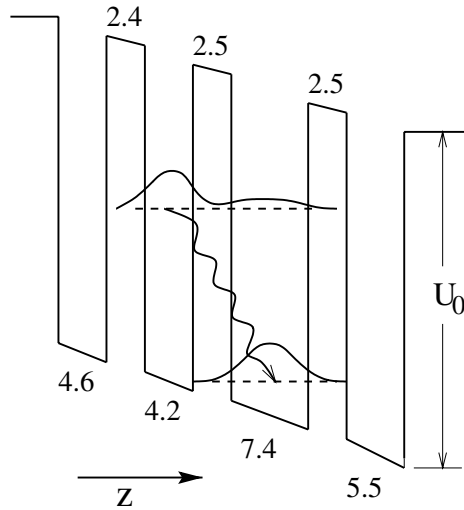
Figure 5.   Energy band diagram (schematic) of the active region of a QCL structure used
        for parallel magnetic field studies by Blaser *et al.* [80]. Only one period of the
        structure is shown here. The relevant wave functions (moduli squared) are also
        shown. The thickness of the layers is indicated in nanometres. The conduction band
        discontinuity, U_0, is 520 meV. The energy difference between the two levels where the
        optical transition takes place is 132 meV [81].

Following the proposal of Blank and Feng [77], Ulrich *et al.* [79] investigated the
magnetic field effect of intersubband luminescence in a QC structure. These authors
investigated a structure with a subband separation below the longitudinal optical
(LO)-phonon energy (36 meV in GaAs), in order to achieve intersubband emission in
the far-infrared (or terahertz) frequency range (60–300 μm). They observed that the
intersubband lifetime is increased by application of a field normal to the electron
plane. For example, application of a magnetic field enhances the emission intensity
by a factor of two at $B = 7.2$ T. Ulrich *et al.* attributed this effect to suppression of
the non-radiative intersubband transitions by Landau quantization of the in-plane
electron motion. Interestingly, they also observed a slight red-shift of the emission
peak in a magnetic field, but this was explained as an artifact of the measurement
setup. A red-shift of the emission peak, as we shall see below, is also a hallmark of
the applied field.

4.1.1. *Parallel magnetic field*

Application of an external magnetic field to the QCL to simulate a quantum-dot-like
situation in the QCL was explored by Blaser *et al.* [80]. The energy band diagram of
their QCL structure is shown in figure 5. Their experimental results were, however,
inconclusive. In particular, for a magnetic field *parallel* to the electron plane, there
were some puzzling observations. With increasing field strength, the luminescence
peak showed (a) a rapid decrease in intensity, (b) significant broadening, and (c) a
small blue-shift (figure 6). As explained below, the single-particle theoretical model
cannot explain these observations [80, 81]. This model predicts a red-shift of the
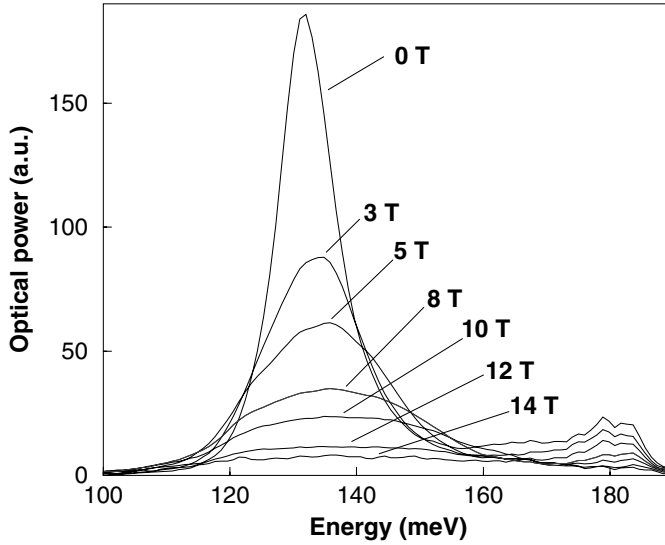emission peak that cannot be cancelled by many-body corrections [82].

Figure 6.   Observed luminescence spectra at different values of the applied parallel magnetic field (in tesla) [80].

Let us consider the situation where the magnetic field B is applied in the y-direction. With the choice of the vector potential $\mathbf{A} = (Bz, 0, 0)$, the single-electron Hamiltonian can be straightforwardly written in the form [80]

$$\mathcal{H} = -\frac{\hbar^2}{2m^*}\frac{\partial^2}{\partial z^2} + \frac{\hbar^2}{2m^*}k_y^2 + \frac{\hbar^2}{2m^*}\left(k_x^2 - \frac{2eBk_xz}{\hbar} + \frac{e^2B^2z^2}{\hbar^2}\right) + V_{\text{conf}}(z) \tag{7}$$

where $V_{\text{conf}}(z)$ is the confinement potential due to the conduction band discontinuity. The first term, associated with the magnetic field, $2eBk_xz/\hbar$, acts like an electric field, while the second term, $e^2B^2z^2/\hbar$, is quadratic in B. Since the cyclotron radius at the highest magnetic field considered for the QCL (68 Å for 14 T) is greater than the typical width of the well in the QCL (~ 50 Å), and the confinement potential is barely influenced by the two terms due to the magnetic field, the magnetic field can be considered as a perturbation [83] with the perturbation term of the Hamiltonian

$$\mathcal{H}_{\text{pert}} = \frac{1}{2m^*}\left(2\mathrm{i}eB\hbar\frac{\partial}{\partial x}z + e^2B^2z^2\right). \tag{8}$$

Considering only the first-order correction to the energy, we get

$$\mathcal{E} = \mathcal{E}_{\text{conf}}(z) + \frac{\hbar^2}{2m^*}k_y^2 + \frac{\hbar^2}{2m^*}\left(k_x - \frac{eB\langle z\rangle}{\hbar}\right)^2 + \frac{e^2B^2}{2m^*}\left(\langle z^2\rangle - \langle z\rangle^2\right) \tag{9}$$

where $\langle z\rangle_\alpha = \int \xi_\alpha(z)z\xi_\alpha(z)\,\mathrm{d}z$, $\xi_\alpha(z)$ is the electron wave function in subband α, and $\mathcal{E}_{\text{conf}}(z)$ corresponds to the energy due to the confinement potential. The third term on the right-hand side of equation (9) changes the usual dispersion in k_x to a shift of the parabola in k-space by $k_{\text{shift}} = -eB\langle z\rangle/\hbar$ (figure 7). The fourth term is the diamagnetic shift and its effect on the energy is minimal. If we disregard this diamagnetic term, the energy spectrum in the non-zero magnetic field is the same
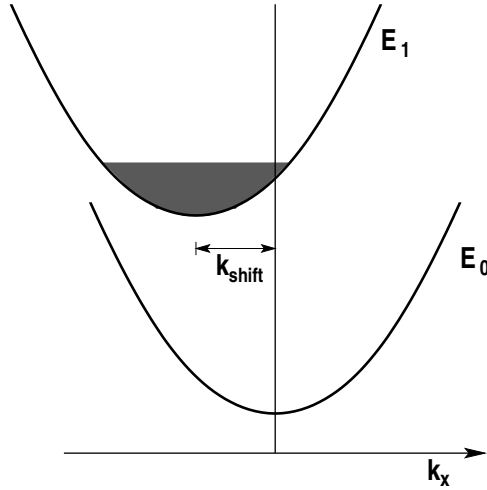
Figure 7.   The shift of electron dispersion in k-space due to the parallel field [83].

as for the zero magnetic field. The wave functions differ only by a phase factor which corresponds to a translation in k-space of the vector $(eB/\hbar\langle z\rangle_\alpha, 0)$.

The major effect of the shift of dispersion in k-space is on the emission spectra because the intensity of the optical transition from the initial state i to the final state f is proportional to the overlap between $\psi_i(k_x, k_y)$ and $\psi_f(k_x - k_B, k_y)$, where ψ_i and ψ_f are the wave functions of the initial and final system, respectively, in the absence of a magnetic field:

$$\mathcal{I}_{if} = \left| \int \psi_i^*(k_x, k_y)\psi_f(k_x - k_B, k_y)\, \mathrm{d}k_x\, \mathrm{d}k_y \right|^2. \tag{10}$$

The wave vector k_B is equal to

$$k_B = \frac{e}{\hbar c} B(\langle z\rangle_i - \langle z\rangle_f).$$

The position of the maximum of the emission line is determined mainly by the transitions from the ground state of the single-particle system. Without any disorder, the single-particle wave functions are plane waves $\psi_i(k_x, k_y) = \delta(k_x - k_{x,i}) \times \delta(k_y - k_{y,i})$, with the ground state at $k = 0$. Clearly, the allowed transitions are then only from the ground state ($k_x = 0$) of the upper subband to the excited states ($k_x = k_B$) of the lower subband, resulting in a red-shift of the emission line in a magnetic field (figure 8).

4.1.2. *Many-body effects: depolarization shift*
Because of the high density of the two-dimensional electron gas in the quantum well, many-body effects often cannot be ignored. As discussed in section 2, intersubband resonance in doped semiconductor quantum well systems is a collective mode better described as a plasmon, or charge-density excitation [20, 17]. The most obvious consequence of this collective mode is a shift of the intersubband resonance from the value of the energy separation of single-particle states. In a system like GaAs quantum wells, with almost parabolic and parallel subbands, collective effects
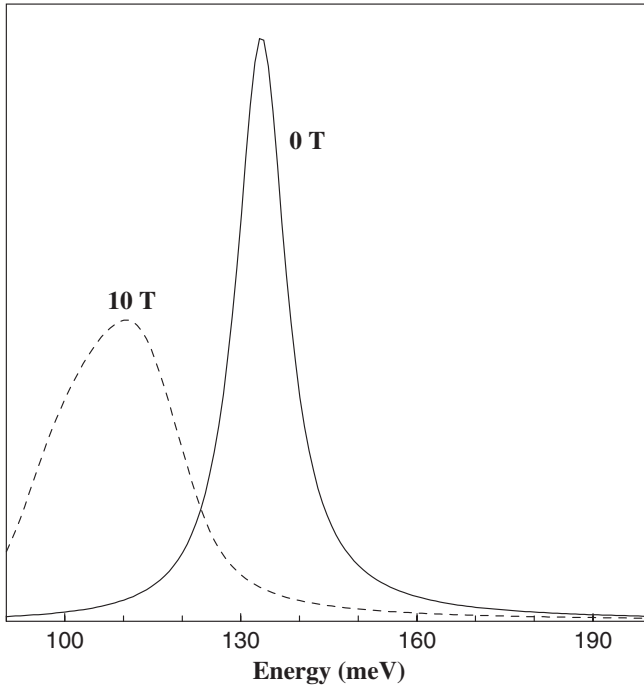
Figure 8. Luminescence spectra of a quantum cascade structure in the presence of an externally applied parallel magnetic field, but in the absence of any impurity [81].

such as dynamical screening of electrons lead to a blue-shift of the resonance—the so-called *depolarization shift* (section 2).

In its standard form, the new transition energy due to the shift of the intersubband transition [84] is

$$\tilde{E} = E_{if}^2 + E_{pl}^2$$

where the plasmon energy is obtained from

$$E_{pl}^2 = 2e^2 n_e S E_{if}/\varepsilon$$

with ε being the background dielectric constant and

$$S = \int_{-\infty}^{\infty} dz \left[\int_{-\infty}^{z} \phi_f(z')\phi_i(z')\, dz' \right]^2$$

is the depolarization integral. Results derived from the experimental parameters and inserted in the above equations indicate, however, that this collective effect on its own cannot explain the small blue-shift (instead of the expected red-shift) of the observed transition peak [85, 86].

4.1.3. *The role of disorder*

It has been demonstrated by Apalkov and Chakraborty [81] that disorder has an important effect on the emission peak in the presence of a magnetic field. Although the techniques of crystal growth have improved significantly in recent decades, interface roughness in QCL structures cannot be entirely eliminated. In a narrow

quantum well, electrons are closer to the interface and are influenced by irregularities or by the charged impurities confined at the interface. These authors studied the single-particle energy spectra and emission lines for two types of disorder potentials: for disorder due to surface roughness in quantum wells and for disorder due to doped charged impurities. The disorder potential in the first case is described by the potential $V_{\mathrm{dis},1}(x, y)$ which has zero average and Gaussian correlations [87]

$$\left\langle V_{\mathrm{dis},1}(\mathbf{r}_1) V_{\mathrm{dis},1}(\mathbf{r}_2) \right\rangle = V_0^2 \mathrm{e}^{-(\mathbf{r}_1 - \mathbf{r}_2)^2 / l_0^2}$$

where $\mathbf{r}$ is a two-dimensional vector.

In the case of a charged impurity we assume that all impurities are in the same two-dimensional plane with position z_{imp}. The potential has the form [87]

$$V_{\mathrm{dis},2}(\mathbf{r}) = -\sum_i \frac{e^2}{\varepsilon} \frac{\mathrm{e}^{-|\mathbf{r} - \mathbf{R}_i|/d_{\mathrm{sc}}}}{\sqrt{(\mathbf{r} - \mathbf{R}_i)^2 + (z - z_{\mathrm{imp}})^2}}$$

where $\mathbf{R}_i$ is a two-dimensional vector describing the position of the i-th impurity and d_{sc} is a phenomenological constant which describes the screening of impurity potential by electrons. For the results presented below, $d_{\mathrm{sc}} = 10\,\mathrm{nm}$, and the two-dimensional density of impurities is equal to $n_{\mathrm{imp}} = 2.3 \times 10^{11}\,\mathrm{cm}^{-2}$. The positions of the impurities are uncorrelated.

The emission spectra of the QCL system in the presence of a disorder potential $V_{\mathrm{dis}}(x, y)$ were calculated as follows [81]. The dispersion of the electron in the first and in the second subband (figure 6) for a given magnetic field was calculated from equation (7). Without any disorder the states are characterized by a two-dimensional momentum $\hbar(k_x, k_y)$. Taking these states as a basis, the total Hamiltonian with the given disorder potential in a square geometry of size L with periodic boundary conditions is diagonalized. The emission spectra are then obtained from

$$I(\omega) = \left\langle \sum_{if} \delta(\omega - E_i + E_f) \left| \int \chi_2(z) \chi_1(z) \mathrm{d}z \right|^2 \left| \int \psi_i^*(k_x, k_y) \psi_f(k_x, k_y)\, \mathrm{d}k_x\, \mathrm{d}k_y \right|^2 \right\rangle, \quad (11)$$

where E_i, E_f are the electron energies before and after emission, $\chi_1(z)$, $\chi_2(z)$ are envelope functions of the electron in the first and second subbands, and $\psi_i(k_x, k_y)$, $\psi_f(k_x, k_y)$ are the initial and final wave functions for a given disorder potential. The summation in equation (11) is over all final states and over occupied initial states. The number of occupied initial states is determined by $N_i = L^2/n_{\mathrm{el}}$, where $n_{\mathrm{el}} = 2.3 \times 10^{11}\,\mathrm{cm}^{-2}$ is the electron density. The angular brackets correspond to averaging over the disorder configurations.

A strong enough disorder will localize the lowest states. If the localization length is smaller than $1/k_{\mathrm{B}}$ then the overlap between the initial ground state and the final ground state is large and the transition from a ground state to a ground state (in different subbands) of the system is strong in a magnetic field and the red-shift of the emission line is suppressed.

In figure 9, the emission spectra are shown for a system with disorder. In figure 9(*a*), where the disorder is charge neutral, the solid curves correspond to $V_0 = 30\,\mathrm{meV}$ and $l_0 = 5\,\mathrm{nm}$, and the dashed curves correspond to $V_0 = 20\,\mathrm{meV}$ and $l_0 = 5\,\mathrm{nm}$. In figure 9(*b*), the disorder is due to the charged impurity, and the solid and dashed lines correspond to the separation, 3 and 4 nm, respectively,
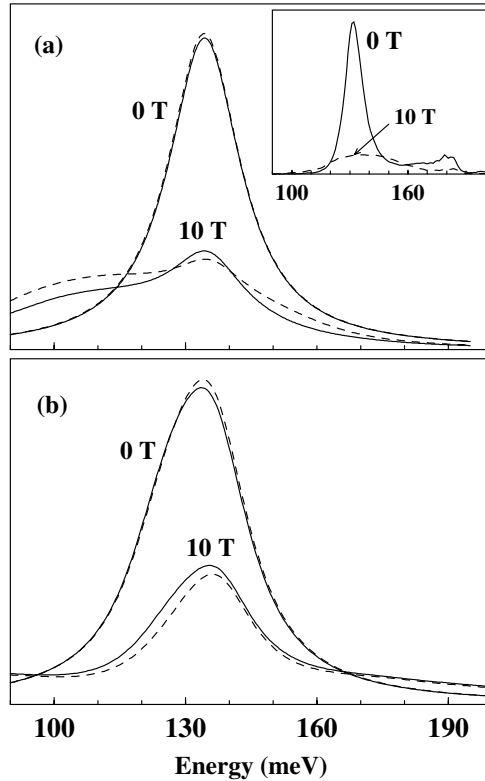
Figure 9. Luminescence spectra of a quantum cascade structure in the case of (*a*) charge-neutral impurities and (*b*) charged impurities in the presence of an externally applied parallel magnetic field. The experimental results of [80] are shown as an inset.

between the impurity plane and the 4.2 nm quantum well (figure 9). In both cases we see large suppression of the red-shift observed in figure 8. The emission line for the high magnetic field case is almost at the same energy as for the zero-field case, and in figure 9(*b*) there is a small blue shift of the peak. These results are in qualitative agreement with the experimental data of [80] and are shown as an inset in figure 9. Further, the intensity of the luminescence peak shows a rapid decrease in the presence of disorder and high fields because of the small overlap in equation (10).

The small blue-shift in figure 9(*b*) is due to the non-parabolicity of the band structure. At zero magnetic field the non-parabolicity of the band structure allows transitions from the ground state to the excited states. The magnetic field redistributes the transitions and increases the intensity of transitions into the ground state, which results in a small blue-shift.

The evolution of the emission spectra for various values of the disorder strength is shown in figure 10 for the two cases, viz. when the disorder is charge-neutral (figure 10(*a*)) and when the disorder corresponds to charged impurities (figure 10(*b*)). To study the dependence of the spectra on the disorder strength, we consider the disorder potential of the form $V_{\alpha,\mathrm{dis},1}(r) = \alpha V_{\mathrm{dis},1}(\boldsymbol{r})$ (in figure 10(*a*)) and $V_{\alpha,\mathrm{dis},2}(r) = \alpha V_{\mathrm{dis},2}(\boldsymbol{r})$ (in figure 10(*b*)), where α is the number changing the amplitude (strength) of the disorder potential. The charge-neutral disorder potential, $V_{1,\mathrm{dis},1}$, corresponds to the parameters $V_0 = 40\,\mathrm{meV}$ and $l_0 = 5\,\mathrm{nm}$, and the disorder due to
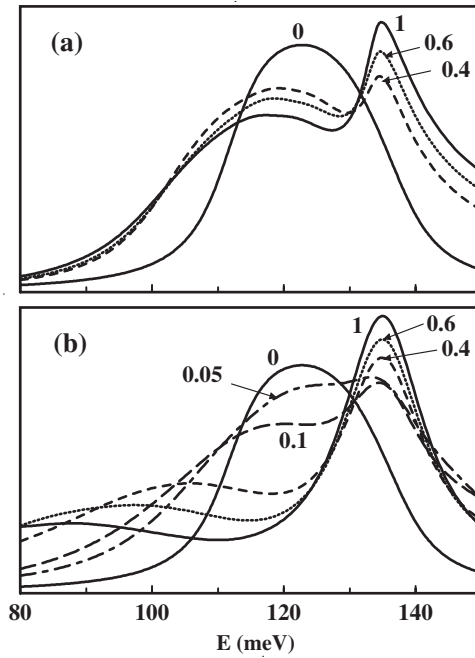
Figure 10.   Luminescence spectra of a quantum cascade structure in the case of charge-neutral impurities (*a*) and charged impurities (*b*) as a function of the strength of the disorder potential. The magnetic field is 10 T. The number near the curves is the disorder amplitude in arbitrary units.

Figure 11.   Illustration of the origin of combined intersubband–cyclotron transitions. Electrons are in the *xy*-plane while the magnetic field is tilted from the *z*-axis. The intersubband–cyclotron coupled transitions due to quantization of subbands to Landau levels (marked as 0, 1, 2, …etc.) are shown here as dash-dotted lines.

the charged impurities corresponds to the 2 nm separation between the impurity plane and the 4.2 nm quantum well. The parameter α is shown in figure 10 near the curves. The appearance of the emission line of zero-magnetic field frequency is clearly seen for a relatively small disorder strength. This line is narrow and becomes more pronounced for greater disorder. At the same time, there is a broad shoulder which is red-shifted from the narrow line and decreases in amplitude with increasing disorder.
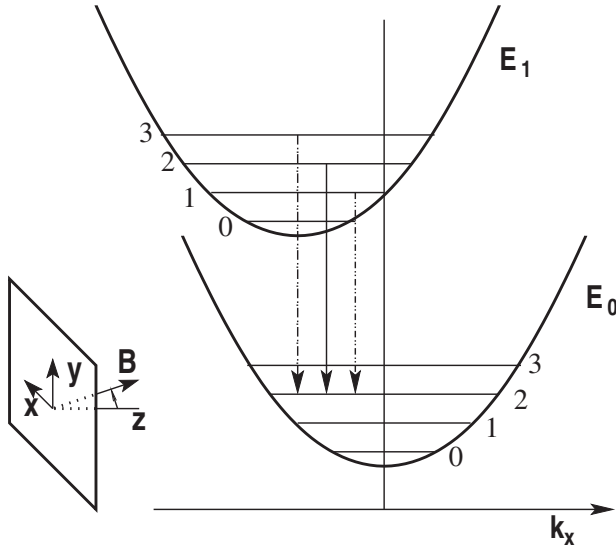
4.1.4. *Tilted magnetic field*

Instead of a parallel field, application of a *tilted* magnetic field on a QCL is expected to result in a very interesting effect first proposed by us [82]. An externally applied magnetic field that is tilted from the direction perpendicular to the electron plane provides two magnetic-field components: the parallel component of the field causes a shift in the energy dispersion in addition to a small diamagnetic shift [83, 81] as described above; the perpendicular component, on the other hand, causes quantization of the subbands. Because of the shifts of the centre of the Landau orbit in wave-vector space, *combined intersubband–cyclotron transitions* (figure 11), in addition to the usual intersubband transitions, are allowed [88–90]. Our detailed calculations presented below indicate that as the subbands quantize into discrete Landau levels, new luminescence peaks appear which correspond to these new transitions. The peaks exhibit a prominent red-shift but can be made as sharp and large as the zero-field case by tuning the applied field. The effect proposed here can be important for applications because it shows that, for a given QCL device, it is possible to shift the luminescence peak considerably by an external magnetic field.

An externally applied magnetic field tilted from the direction perpendicular to the electron plane is a well-studied problem experimentally as well as theoretically, in the context of quantum Hall effects [88, 91, 92]. For a magnetic field tilted from the z-direction the perpendicular and parallel motions of electrons are coupled and as a result transitions between different Landau levels of the ground and upper subbands become possible. The Hamiltonian of the system in a tilted field is

$$\mathcal{H} = \mathcal{H}_\perp + \mathcal{H}_\parallel + \mathcal{H}'$$

where

$$\mathcal{H}_\perp = \frac{1}{2m^*}p_z^2 + V_{\text{eff}}(z) + \frac{\hbar^2}{2m^*}\frac{z^2}{\ell_\parallel^4}$$

$$\mathcal{H}_\parallel = \frac{1}{2m^*}\left[p_x^2 + \frac{\hbar^2}{\ell_\perp^4}(x+X)^2\right]$$

$$\mathcal{H}' = \frac{\hbar}{m^*}\frac{zp_x}{\ell_\parallel^2}$$

and where $X \equiv (p_y/\hbar)\ell_\perp^2$ is the centre coordinate of the cyclotron motion and $\ell_\parallel^2 = c\hbar/eB_y$, $\ell_\perp^2 = c\hbar/eB_z$ are the magnetic lengths. Here we have chosen the Landau gauge vector potential, $\mathbf{A} = (B_y z, B_z x, 0)$. The magnetic field is therefore in the (y, z) plane and $B_y = B\sin\theta$, $B_z = B\cos\theta$, θ is the tilt angle and B is the total magnetic field [88].

The effective potential is made up of

– The confinement potential due to the discontinuity in the conduction band and the bias electric field F in the z-direction:

$$V_{\text{conf}}(z) = -eFz + \begin{cases} 0 & \text{for wells} \\ U_0 & \text{for barriers} \end{cases} \tag{12}$$

– The Hartree potential,

$$V_H = -4\pi \frac{e^2}{\epsilon} \left[\int_{-\infty}^{z} dz'(z - z')n(z') - \frac{1}{2}N_s z \right]$$

where

$$n(z) = \frac{2}{2\pi \ell_\perp^2} \sum_N \int dx\, dy\, \frac{\left|\Psi_{2,N}(x, y, z)\right|^2}{\exp(\beta(E_{2,N} - \mu)) + 1}$$

is the density distribution of electrons in the well. Here $E_{2,N}$ is the energy of the N-th Landau level in the second subband (only the second subband is occupied), and μ is the chemical potential which is related to the electron concentration per unit area

$$N_s = \frac{2}{2\pi \ell_\perp^2} \sum_N \frac{1}{\exp(\beta(E_{2,N} - \mu)) + 1}$$

where the summation is over the states which belong to the second subband.
– The exchange-correlation potential [93].

The wave functions of the Hamiltonian $\mathcal{H}_\perp$, which depends only on the z-coordinate, are obtained from

$$\mathcal{H}_\perp \psi_n = E_n \psi_n(z).$$

The solutions of this equation determine the energy levels and wave functions of the subbands. The total Hamiltonian is diagonalized by choosing the basis wave functions

$$\Psi_{n,N,X} = L^{-1/2} \exp\left(-i\frac{X}{y}\ell_\perp^2 - i\frac{z_{nn}}{\ell_\parallel^2}(x - X)\right)\xi_N(x - X)\psi_n(z)$$

$$\xi_N(x) = i^N (2^N N! \pi^{1/2} \ell_\perp)^{-1/2} H_N\left(\frac{x}{\ell_\perp}\right)\exp\left(-\frac{x^2}{2\ell_\perp^2}\right)$$

$$z_{nm} = \int dz\, \psi_n(z)\, z\, \psi_m(z) \tag{19}$$

where $H_N(x)$ is a Hermite polynomial. The matrix elements of the Hamiltonian $(n'N'X'|\mathcal{H}|nNX)$ are then calculated in this basis. The matrix is diagonal in X. To calculate the wave functions we have used three subbands and 20 Landau levels on each subband [82].

The optical spectra are calculated as follows. Optical transitions occur between Landau levels of the second and first subbands. We introduce variables that are proportional to the matrix elements of optical transitions

$$u_{N,N_1} = \frac{1}{eF} \left(\frac{2m^*}{\hbar^2}\right)^{-1/2} \frac{(1, N|\mathcal{H}^*|2, N_1)}{(E_{2,N_1} - E_{1,N})^2 - (\hbar\omega)^2} \{f(E_{2,N_1})\}^{1/2}$$

where $\mathcal{H}^*$ is the change in the Hamiltonian due to an external electric field F in the z-direction, and $f(\epsilon)$ is the Fermi distribution function. Note that we consider the first subband as empty. The emission spectrum is related to u_{N,N_1} through

$$\mathcal{I}(\omega) \propto \omega \frac{1}{2\pi\ell_\perp^2} \sum_{N, N_1} z_{1,2} \{f(E_{2,N_1})\}^{1/2} \mathrm{Im}(u_{N,N_1})$$

where ω is the frequency of the emitted photon.

The intensity of the optical emission is determined by the dipole matrix elements between initial (before emission) and final (after emission) states of the multi-electron system. In dipole transitions the transition intensity is proportional to the overlap between the (x, y)-dependent parts of the wave functions of the initial and final states. For a vanishing perpendicular magnetic field this results in conservation of the two-dimensional momentum in the optical transition. For non-zero perpendicular magnetic fields the states of the two-dimensional electrons are classified by two numbers: by the Landau level index and by a number that distinguishes the degenerate states of an electron within a Landau level, for example, by the x-component of the momentum. The energy of the single-electron system depends only on the number of the Landau level, and the wave functions are harmonic oscillator functions whose centre is determined by the x-component of the momentum. If the magnetic field is directed perpendicular to the two-dimensional layer then optical transitions are allowed only between the states with the same two-dimensional quantum numbers. In this case we will have a single line which corresponds to the optical transitions between states with the same Landau level index.

Evolution of the emission spectra as a function of the tilted magnetic field is illustrated in figure 12 where the optical spectra are shown for three values of the perpendicular component of the field and for different values of the parallel component of the field for a fixed B_{perp}. Clearly, for small B_{perp} (figure 12(a)), the emission spectra do not feel the Landau quantization and we have a single peak which broadens with increasing B_{par}. For higher fields such as $B_{\mathrm{perp}} = 5\,\mathrm{T}$ (figure 12(b)), we find new features in the emission spectra. For a small parallel field, $B_{\mathrm{par}} = 1$ T, the main transitions are between the states with the same Landau index, hence there is a single peak that corresponds to transitions from the zeroth Landau level of the second subband to that of the first subband. An increase of the parallel field makes transitions to higher Landau levels more intense. The appearance of a shoulder at $B_{\mathrm{par}} = 5\,\mathrm{T}$ corresponds to transitions to the first Landau level of the first subband. Similarly, the peaks at $B_{\mathrm{par}} = 10\,\mathrm{T}$ and $15\,\mathrm{T}$ correspond to transitions from the zeroth Landau level of the second subband to the higher Landau level of the first subband. The energy separations between the peaks are equal to the separations between Landau levels of the first subband. In figure 12(c), transitions to a non-zero Landau level become more intense and we observe an interplay between the transitions to zero and to the first Landau levels with increasing parallel field. For a small B_{par} ($B_{\mathrm{par}} = 1$ T), there is only a strong transition to the zeroth Landau level. For $B_{\mathrm{par}} = 5\,\mathrm{T}$, we observe the appearance of a small peak that corresponds to transitions to the first Landau level, and for $B_{\mathrm{par}} = 10\,\mathrm{T}$ and $15\,\mathrm{T}$, transitions to the
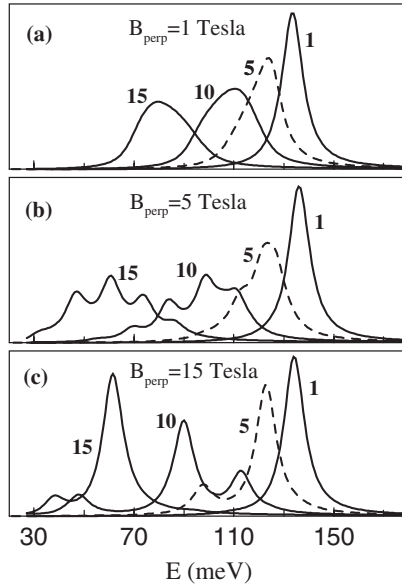
Figure 12. Luminescence spectra at various values of the parallel component of the magnetic field (numbers by the curves in tesla) for a fixed value of the perpendicular component of the field. [82].
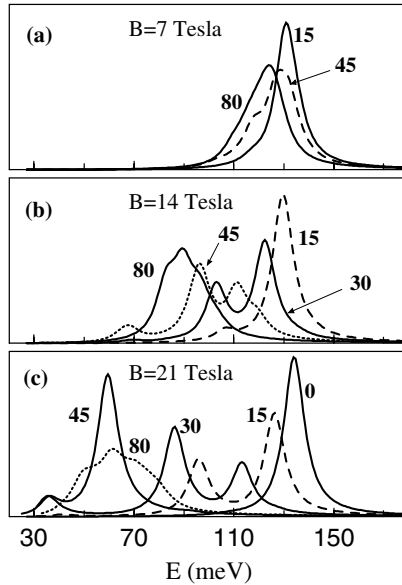
Figure 13. Luminescence spectra at various values of the tilt angle (numbers by the curves) for the total magnetic fields (*a*) $B = 7$ T, (*b*) $B = 14$ T and (*c*) $B = 21$ T [82].

first Landau level become strongest and we observe the formation of a new narrow peak that corresponds to a transition to the first Landau level.

In figure 13, emission spectra are shown for three values of the total magnetic field B and for different values of the tilt angle at a fixed B. For a small field (figure

13(a)) we have a red shift of the emission spectra with increasing parallel field (i.e. increasing tilt angle). For $\theta = 45°$ there is a weak structure resulting from the Landau quantization. At higher fields (figure 13(b),(c)), one observes the evolution of the emission spectra from a broad peak at a large angle, $\theta = 80°$ (a large parallel field and a small perpendicular field), to a single narrow peak for a small angle. In the latter case, the parallel component of the magnetic field is small and all optical transitions are transitions between the Landau levels with the same index. For an intermediate tilt angle, there are two peaks that correspond to transitions from the zeroth Landau level of the second subband to the zeroth and the first Landau levels of the first subband. The intensity of the transition to the first Landau level increases with increasing angle, which means an increase of the parallel field. It has its maximum at $\theta = 45°$ and for a total magnetic field of $B = 21\,\mathrm{T}$ one observes the formation of a strong narrow peak at $\theta = 45°$ associated with the suppression of the original peak corresponding to the transition to the zeroth Landau level of the first subband. From these results we conclude that by suitably tuning the externally applied tilted field, lasing due to coupled intersubband–cyclotron transitions that is as strong as the zero-field case (but at different energies) can be acheived. However, in the light of disorder effects discussed above, it is clear that in a QCL device magnetic field induced luminescence spectra [82] can only be observed in the absence of strong disorder, i.e. devices with high electron mobility or for wider quantum wells.

4.2. *Magneto-transport experiments and phonon relaxation*

Magneto-transport measurements on GaAs QCL [44] with a pulsed field of up to 62 T and *perpendicular* to the electron layers at liquid helium temperature have been reported recently [94, 95]. The GaAs/GaAlAs QCL structure (figure 14) had 40 periods of 47.5 nm length, and a lasing wavelength of 11.4 µm. In this experiment, a new quantum oscillation was observed in the tunnelling current that is periodic in the reciprocal magnetic field. These novel oscillations are shown to originate from resonant intersubband relaxation of electrons from the ground state of the upper subband of the central wells into an excited Landau level of the lower subbands. A
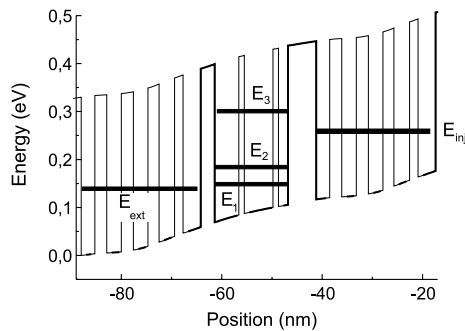
Figure 14. Electronic structure depicted along two periods of a GaAs/GaAlAs QCL under an internal bias of 117 mV. Energy levels are indicated as thick horizontal lines. The layer sequence in nm from the extractor/injector (right) towards the active region (left) is: 3.6/**1.7**/3.2/**2.2**/3.0/**2.4**/3.0/**2.4**/2.8/**5.6**/1.9/**1.1**/5.8/**1.1**/4.9/**2.8**. GaAlAs barriers are in bold with the injection one underlined. Doped wells at $6 \times 10^{17}\,\mathrm{cm}^{-3}$ and barriers at $4 \times 10^{17}\,\mathrm{cm}^{-3}$ are given within the rectangle [95].

Figure 15. (*a*) Oscillatory component of the voltage across the QCL biased at 60 mA and measured in a field of up to 62 T. The second derivative signal is drawn as the dotted line. The inset shows resonance numbers versus the inverse magnetic field, indicated by three series. (*b*) Oscillation extrema at a given bias. The dot size is related to the oscillation amplitude strength. One type of oscillation is independent of the applied bias, while the other changes roughly linearly with bias. The slope of the dashed line is equal to the cyclotron energy [95].

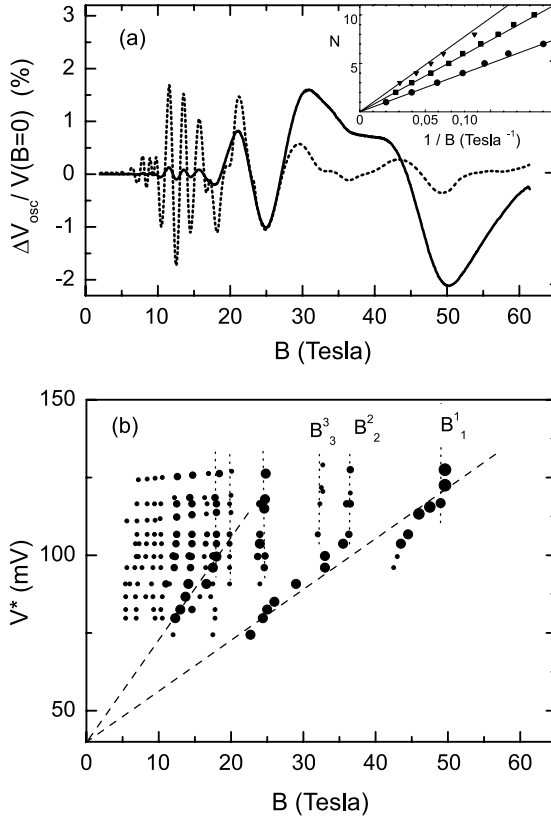remarkable feature of these results is the lack of dependence of magnetic field positions of these oscillations on the applied bias, as with in-plane magneto-phonon oscillations.

Figure 15(*b*) displays the magnetic field positions of oscillation extrema at a measured voltage bias V^* applied to the QCL structure. We observe two types of oscillations. The first one occurs mainly in the lower range of bias 75–100 mV (12–35 mA). In this case, the oscillation field positions change roughly linearly with bias as indicated by the dashed lines. The curves are drawn with cyclotron energy slopes according to the relation, $eV^* = eV_0^* + N\hbar\omega_c$ for $m^* = 0.07m_0$. In the other type of oscillations, the oscillation field positions do not change with bias as shown in figure 15(*b*). Figure 15(*a*) shows the oscillatory component of the voltage across the QCL structure where one series of peaks with the largest amplitude appears at a fundamental field near 50 T. The other two series are also visible on the second derivative curve. All these series are identified in the inset of figure 15(*a*) which plots the integer N versus the reciprocal magnetic field. We label the harmonics in the three series as B_N^i with $i = 1, 2$ and 3 indicating the lower, middle and upper curves,

respectively. The fundamental fields are obtained from the slopes at the values $B_1^1 = 50\,\text{T}$, $B_1^2 = 75.5\,\text{T}$ and $B_1^3 = 95\,\text{T}$. We can then derive the cyclotron energies $\varepsilon^{(i)} = \hbar e B_1^i / m^*$ by using the effective mass values measured in a two-dimensional GaAs electron gas in the same field range as the fundamental fields [96]. We obtain $\varepsilon^{(1)} = 72\,\text{meV}$, $\varepsilon^{(2)} = 109\,\text{meV}$, and $\varepsilon^{(3)} = 149\,\text{meV}$. Since these energy values are given by series that are insensitive to the QCL bias, they must be related to the electronic structure of the central wells. In fact, we find $\varepsilon^{(2)}$ and $\varepsilon^{(3)}$ are nearly equal to the photon energies that we measured by electroluminescence on this structure, namely 108.7 meV (laser line) and 147 meV (weak luminescence line), respectively. We may then identify the energies $\varepsilon^{(2)}$ as $E_{3,0} - E_{2,0}$ and $\varepsilon^{(3)}$ as $E_{3,0} - E_{1,0}$.[4] The resonance condition for the two series (middle and upper lines in the inset) are then expressed as $E_{3,0} - E_{2,0} = N\hbar\omega_c$ and $E_{3,0} - E_{1,0} = N\hbar\omega_c$, where $\omega_c = eB/(m^*c)$ is the cyclotron frequency in the magnetic field B. This corresponds to the elastic transition from $E_{3,0}$ into an excited Landau level of the other subbands, E_2 and E_1, respectively.

On the other hand, if one adds the LO-phonon energy (36 meV) to $\varepsilon^{(1)}$, one gets 108 meV, which is close to $E_{3,0} - E_{2,0} = 108.7\,\text{meV}$. Therefore, the resonance condition for the series corresponding to the lower curve may be $E_{3,0} - E_{2,0} - \hbar\omega_{\text{LO}} = N\hbar\omega_c$. This corresponds to an inelastic transition with LO-phonon emission into an excited Landau level of the E_2 subband. A similar inelastic transition is expected into the E_1 subband when $E_{3,0} - E_{1,0} - \hbar\omega_{\text{LO}} = N\hbar\omega_c$. In total, one expects four series arising from elastic and inelastic intersubband scattering. However, since in the QCL structure the separation of the lower subbands equals the LO-phonon energy, the elastic resonance transition from the $E_{3,0}$ into the $E_{2,N}$ subbands overlaps with the inelastic resonance transition into the $E_{1,N}$ subbands. As a result, only three oscillation series should be obtained, as was found in the experiment.

The observed tunnelling current oscillations can indeed be accounted for by resonant intersubband relaxation of electrons with both optical and acoustic phonon emission. A schematic illustration of the resonant condition for electron relaxation due to emission of LO optical phonons is shown in figure 16. Under experimental conditions, the electrons are injected in the third subband, $n = 3$. At zero magnetic field the relaxation of these electrons to the first and second subbands with emission of LO phonons is allowed. This is because electron dispersion is similar to that for continuous free particles. At non-zero magnetic field the energy spectrum in each subband becomes a discrete ladder of Landau levels. Then the emission of LO phonons, which requires energy conservation, becomes of resonant–antiresonant type. For a GaAs QCL sample (laser emission at 9.2 μm) [48], at $B = 41\,\text{T}$ the transition of electrons from the first Landau level of the third subband, i.e. from the $(3, 0)$ state, is forbidden for processes with emission of LO phonons. This is an antiresonance condition. In this case, the lifetime of the upper state of transition is increased and that increases the population inversion in the case of constant current injection. The optical gain is therefore enhanced and the threshold current is decreased. On the other hand, at $B = 47\,\text{T}$, transitions from the $(3, 0)$ state into $(1, 2)$ are allowed and the system is under resonant conditions. This is reflected in the measured light intensity [97] where the laser is found to switch off for a range of magnetic field around 47 T.

---

[4]In our notation, $E_{3,0}$ corresponds to the first Landau level of the third subband that is occupied, while $E_{2,0}, E_{1,0}$ are the empty subbands where the electron transition takes place.
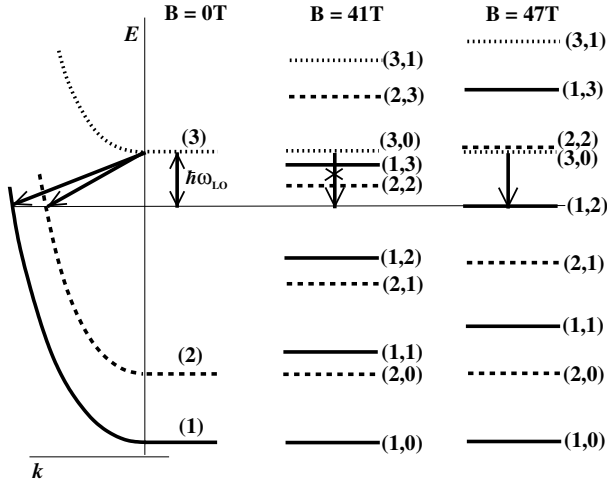
Figure 16. Energy levels of the active region (schematic). At zero magnetic field the electrons in each subband have free particle-like dispersion for in-plane motion. The magnetic field breaks the subbands into three ladders of Landau levels. Each state (n, N) is characterized by two numbers: by the subband index, n, and by the Landau level index, N. The arrows represent LO-phonon emission, allowed for $B = 0$ T and $B = 47$ T, but forbidden for $B = 41$ T. For reasons of clarity, the energy of each state at non-zero magnetic field was lowered by a value of $\hbar eB/2m^*$. Adapted from [97].

To calculate the electron relaxation rate due to emission of optical and acoustic phonons we rewrite the Hamiltonian of the one-electron system in a perpendicular magnetic field in analogy to the case of a tilted magnetic field discussed above,

$$\mathcal{H} = \mathcal{H}_1 + \mathcal{H}_2$$

where

$$\mathcal{H}_1 = \frac{1}{2m^*} p_z^2 + V_{\text{conf}}(z),$$

$$\mathcal{H}_2 = \frac{1}{2m^*} \left[p_x^2 + \frac{\hbar^2}{l_c^4} (x + X)^2 \right],$$

and l_c stands for the magnetic length, $l_c^2 = c\hbar/eB$. The vector potential was chosen in the Landau gauge, $\mathbf{A} = (0, B_y, 0)$. Here we do not take into account many-body effects and in the expression for $\mathcal{H}_1$ keep only the confinement potential.

The eigenfunctions of the total Hamiltonian $\mathcal{H}$ are the products of the eigenfunctions of the Hamiltonians $\mathcal{H}_1$ and $\mathcal{H}_2$

$$\Psi_{n,N,X}(x, y, z) = L^{-1/2} \exp\left(\frac{-iXy}{l_c^2} \right) \xi_N(x - X) \psi_n(z),$$

$$\xi_N(x) = i^N (2^N \pi^{1/2} N! l_c)^{-1/2} H_N\left(\frac{x}{l_c} \right) \exp\left(-\frac{x^2}{2l_c^2} \right)$$

where N is the Landau level number and n is the subband index.

Then the rate of electron transition (relaxation) from $E_{3,0}$ into the $E_{i,N}$ states can be calculated from equations (2.1) and (2.3)

$$\tau_{\mu,i}^{-1} = \frac{2\pi}{\hbar} \sum_{X_1,X_2} \left| \langle \Psi_{3,0,X_1} | V_{\text{int}} | \Psi_{i,N,X_2} \rangle \right|^2 \delta\big(E_{3,0} - E_{i,N} - \hbar\omega_\mu\big)$$

$$= \frac{2\pi}{\hbar} \int \frac{\mathrm{d}\boldsymbol{Q}}{(2\pi)^3} \delta(\Delta_i - \hbar\omega_\mu(Q))(1 + n_\mu(\boldsymbol{Q})) \left| M_\mu(\boldsymbol{Q}) Z_i(q_z) \right|^2 R_{0N}(q) \qquad (13)$$

where the index μ stands for optical (LO) or acoustic (A) phonons, $n_\mu(\boldsymbol{Q})$ is the phonon distribution function, $\Delta_i = E_{3,0} - E_{i,N} = E_3 - E_i - N\hbar\omega_\mathrm{c}$ is the separation between the levels, $\boldsymbol{Q} = (\boldsymbol{q}, q_z)$ is a three-dimensional vector, $\omega_{\mathrm{LO}}(Q) = \omega_{\mathrm{LO}}$, $\omega_A(Q) = sQ$, and M_μ are the matrix elements of electron–phonon interaction [98–102] (equations 2.4 and 2.5). The form factors $Z(q_z)$ and $R_{0N}(q)$ are given by the expressions

$$Z_i(q_z) = \int \mathrm{d}z \mathrm{e}^{\mathrm{i}q_z z} \psi_3(z) \psi_i(z),$$

$$R_{0N}(q) = \left| \int \mathrm{d}x \mathrm{e}^{\mathrm{i}x q_x} \xi_0^*(x) \xi_N(x - q_y) \right|^2 = \frac{1}{N!} \frac{(q l_\mathrm{c})^{2N}}{2^N} \mathrm{e}^{-(q l_\mathrm{c})^2/2}. \qquad (14)$$

Optical phonon relaxation is possible only if the separation Δ_i between the levels is equal to the optical phonon energy, $\Delta_i = \hbar\omega_{\mathrm{LO}}$. The condition for acoustic phonon resonance follows from equations (13) and (14). In fact, the expression (14) for the two-dimensional form factor gives a typical phonon momentum of the order of the inverse magnetic length, $q \sim l_\mathrm{c}^{-1}$. Then acoustic phonon resonance occurs when $\Delta_i = \hbar s/l_\mathrm{c}$ [100].

In figure 17(*a*), the total rate of acoustic phonon emission ($\tau_A^{-1} = \tau_{A,1}^{-1} + \tau_{A,2}^{-1}$) as a function of the magnetic field is shown for $N = 1$–5 in units of 10^{12} s^{-1}. In the final state the electron is in an $E_{1,N}$ or $E_{2,N}$ Landau ladder. There are sharp resonances when $E_3 - E_2$ or $E_3 - E_1$ is close to $N\hbar\omega_\mathrm{c}$. Transitions to $E_{2,3}$ and $E_{1,4}$ are almost at the same magnetic field; this is due to the particular structure of the QCL system: subband energies follow the relation $E_3 - E_2 \approx 3(E_2 - E_1)$, which results in double resonances when the energies of the levels $E_{2,3N}$ and $E_{1,4N}$ are close, where $N = 1, 2, \ldots$. To take into account the disorder effect, we have introduced a broadening of the Landau levels in Lorentz form, with a width of 2 meV and have averaged the relaxation rate over the Landau level distribution.

In figure 17(*b*), the total rate of LO phonon emission is shown as a function of the magnetic field for $N = 1$–5. Due to the particular structure of the QCL system ($E_2 - E_1 \approx \hbar\omega_{\mathrm{LO}}$), resonances due to optical phonons are almost at the same place as the resonances due to acoustic phonons (figure 17(*a*)). Finally, in figure 17(*c*) the total electron relaxation rate ($\tau^{-1} = \tau_A^{-1} + \tau_{\mathrm{LO}}^{-1}$) due to emission of acoustic and optical phonons is shown. At $B \approx 25$ T there are four resonances: two due to the acoustical phonons and the other two due to LO phonons. The model explains the observed resonance field positions fairly well. For example, the oscillation series for transitions to the E_2 subband with optical phonon emission agree within $\sim 1\%$ with the data for the B_N^1 series, and within $\sim 3\%$ with the data for the B_N^2 series (transitions to the E_1 subband). It is to be noted that the latter inelastic series coincide with the elastic series (transition into the E_2 subband) because $E_2 - E_1 = \hbar\omega_{\mathrm{LO}}$, which is unique for the sample used in [95]. This explains why there are three (and not four) series in the observed data (figure 15). For details about the experimental and theoretical results, see [95].
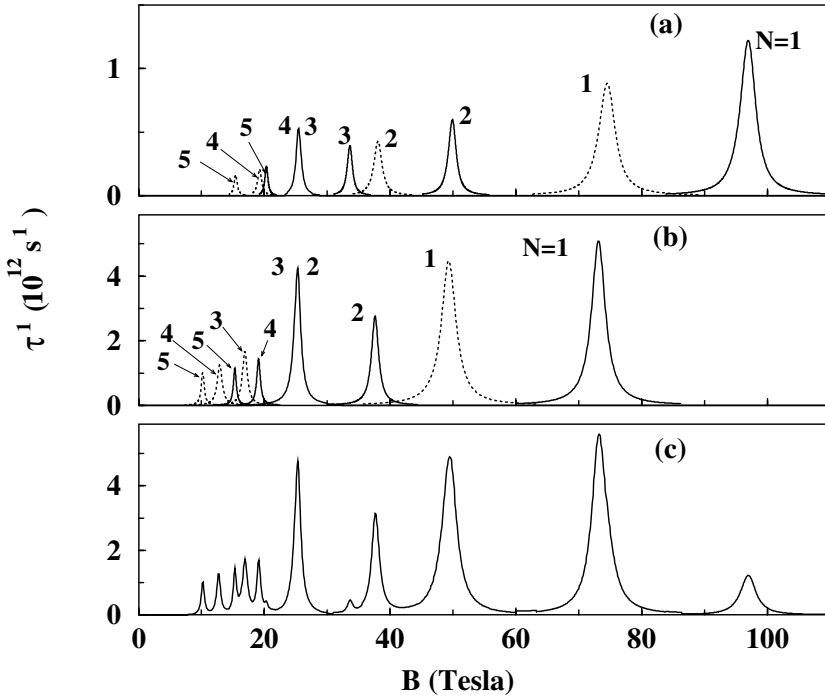
Figure 17.   Acoustic phonon (*a*) and LO phonon (*b*) emission rate in a QCL as a function
of the applied magnetic field. The electron transitions into the first subband and the
second subband are shown by solid and dotted lines, respectively. The lines marked
by two numbers (4 and 3 in (*a*) and 3 and 2 in (*b*)) are the sum of two transitions:
into (E_1, 4) and (E_2, 3) in (*a*) and (E_1, 3) and (E_2, 2) in (*b*). (*c*) The total electron
relaxation rate due to emission of acoustic or optical phonons as a function of
magnetic field.

4.3. *Magneto-optics experiment and phonon relaxation*

As discussed in the previous subsection, the magnetically induced discrete
structure of the energy spectra of electrons in QCLs strongly affects the relaxation
rate of the electrons in the active region of the QCL. The relaxation is mainly due to
the emission of LO optical phonons. Under resonant or antiresonant conditions the
phonon emission is either enhanced or inhibited. This actually modifies the lifetime
of the electrons in the excited states and results in strong oscillations of the relaxation
rate, $1/\tau_{LO}$, due to emission of LO optical phonons as a function of magnetic field
(see figure 16). Another mechanism of relaxation, which is the cornerstone of QCLs,
is due to the emission of light, i.e. photons. Because there is no resonant condition
for this relaxation mechanism (the dispersion of photons is linear rather than flat as
for optical phonons), the rate of relaxation with emission of photons, $1/\tau_{pt}$, has a
weak dependence on the applied magnetic field. As a result the intensity of light as a
function of magnetic field, which is proportional to τ_{LO}/τ_{pt}, should show pro-
nounced oscillations. Under the antiresonant condition the electron–LO-phonon
scattering time is suppressed, i.e. the electron lifetime in the excited state is long,
which results in a high intensity of light emitted by an active region of the QCL.
Conversely, under resonant conditions the lifetime of the electrons is short, and the
intensity of light is low.

From equation (13) we can conclude that the intensity P of the emitted light is proportional to

$$P \propto \left[\int \frac{\mathrm{d}\boldsymbol{Q}}{(2\pi)^3} \delta(\Delta_i - \hbar\omega_{\mathrm{LO}})(1 + n_{\mathrm{LO}})|M_{\mathrm{LO}}(\boldsymbol{Q})Z_i(q_z)|^2 R_{0N}(q) \right]^{-1}. \qquad (15)$$

Strictly speaking, we also need to include in equation (15) the electron relaxation due to emission of acoustic phonons. However, as was shown in the previous subsection (see figure 17), that relaxation mechanism has a much smaller rate compared to the optical phonon mechanism. That is, the main resonance-type features of emission spectra are well described by equation (15).

These oscillations of the dependence of the light intensity on the magnetic field were observed experimentally in [97, 103]. Here the authors used a QCL device based on GaAs/AlGaAs heterostructures, which had a similar structure as in [94, 95] (see figure 14). The observed oscillations are in good agreement with theoretical calculations of the electron–optical-phonon scattering time between different Landau levels under resonant and antiresonant conditions.

5. A brief review of quantum dots

With the advent of modern epitaxial growth techniques, researchers have acquired the ability to create structures with dimensions on the nanometre scale. One major step in these developments has been the reduction of the effective dimension of devices from three-dimensional bulk systems to two-dimensional, to one-dimensional, and finally to zero-dimensional systems. When the size of all these devices becomes comparable with the de Broglie wavelength, a consequence of the wave nature of electrons, electrons confined in these devices display quantum effects. The novel electronic and optical properties of these reduced-dimensional systems, which can be controlled to a certain extent through clever design, make these systems promising candidates for a variety of future applications that include improved semiconductor lasers and microelectronics. Quantum dots represent the ultimate reduction in the dimensionality of a semiconductor device. In these systems, electrons are confined in all directions. Therefore they have no kinetic energy (except the ubiquitous zero-point energy) and as a result they occupy spectrally sharp energy levels like those found in atoms [12].

These zero-dimensional quantum confined systems are useful for investigating the fundamental concepts of nanostructures [12, 104] as well as for its potential to operate at the level of a single electron, certainly the ultimate limit for an electronic device. With a good knowledge of their electrical and optical properties, researchers have now turned their attention on devices based on quantum dots. Some of the best examples are QD photodetectors [105–107], QD lasers [108, 109] and QD memory devices [110, 111]. Quantum dots have also found applications (or have potential applications) in fluorescence markers [112, 113], exciton storage [114, 115], a step toward smart pixels [116], quantum computing [117] and quantum cryptography [118].

5.1. *From three- to zero-dimensional systems*

There are excellent sources available in the literature on the evolution from three- to zero-dimensional systems [19, 119, 120]. These are schematically sketched in

figure 18. The energy of a free electron in the bulk is well known. It is a parabolic function of the three-dimensional wave vector. In a two-dimensional system, such as a quantum well, electron motion is confined in one dimension (say the z-direction). The electron motion is still free in the (x, y) plane and the energy is a parabolic function of the two-dimensional wave vector. In the z-direction, electron motion is quantized into discrete subbands E_i. Further confinement (lateral) of the electron motion leads to one-dimensional (quantum wire) and zero-dimensional (quantum dot) systems. In the case of a quantum dot, the energy E_{inm} is totally discrete, because just like in atoms there is no free motion with continuous energy dispersion in any direction, i.e. electrons have no kinetic energy due to their motion (there is, of course the zero-point energy).

The dimensionality of confinement significantly affects the electronic and optical properties of low-dimensional systems which in turn can be directly attributed to the influence of dimensionality on the density of states (DOS) [121]. This is defined as the number of states in the region bounded by E and $E + dE$, given that the DOS per unit length in each dimension of wave-vector space is uniform. In a three-dimensional system, $\mathcal{N}(E) = (1/2\pi)^2 (2m^*/\hbar^2)^{3/2} \sqrt{E}$ and this is shown in figure 18. In a two-dimensional system, $\mathcal{N}(E) = 1/(2\pi)(2m^*/\hbar^2)$, which means that, for a given quantum state E_n, the two-dimensional DOS is independent of E. Therefore, the cumulative DOS for a series of E_n with $n = 1, 2, 3, \ldots$ will have step-like behaviour as sketched in figure 18. In a one-dimensional system, the DOS, $\mathcal{N}(E) = (1/2\pi)(2m^*/\hbar^2)^{1/2} E^{-1/2}$, diverges as $E \to 0$, a characteristic feature of one dimension. For quantum dots, the DOS is just a set of δ functions as there is no free motion of electrons in any dimension. These are the *artificial atoms* [12, 13, 122] of modern times with a wide range of potential applications.
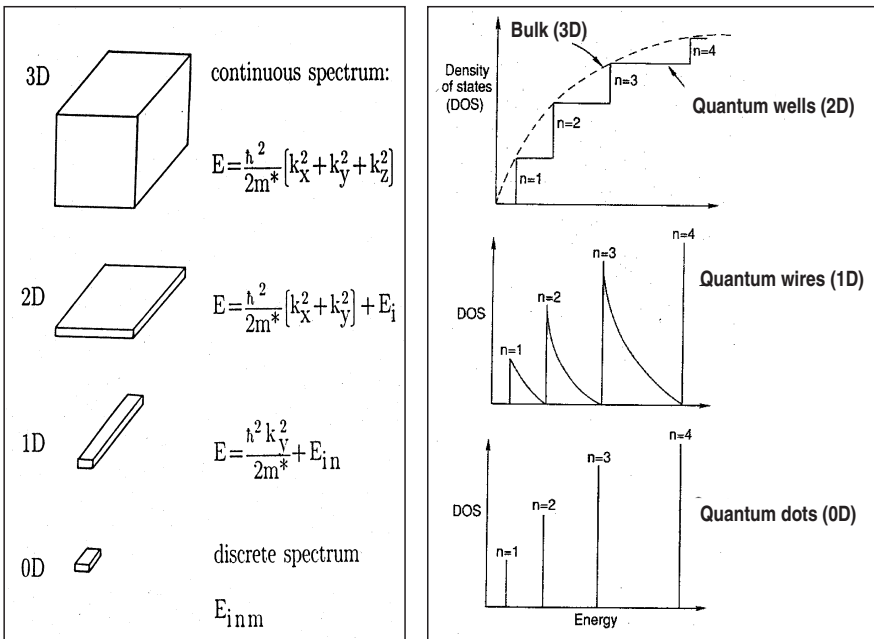

Figure 18.   Low-dimensional electron systems and the corresponding density of states.
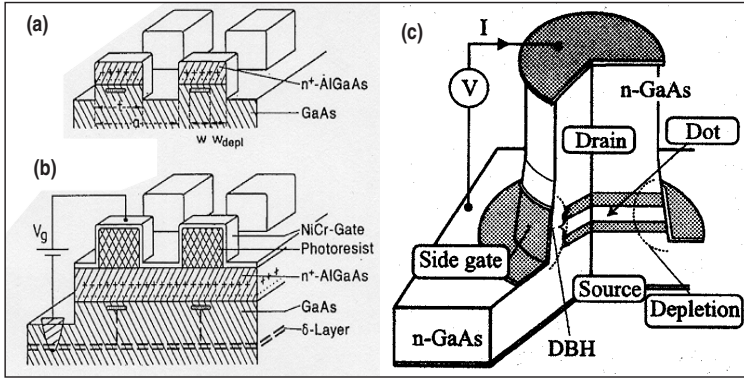
Figure 19.   Manufacture of QDs by lithographic patterning. In (*a*) QD arrays were made by the so-called 'deep-mesa etching' process. In (*b*) field-effect confined QD samples are sketched [123], and (*c*) depicts schematically a device containing a disk-shaped QD [125]. Here DBH means a double-barrier heterostructure where the dot (InGaAs) is sandwiched between two barriers (AlGaAs).

5.2. *Making the dots*

Initially, the most widely followed approach to fabricate QDs was lithographic patterning. In this process, the lateral confinement lengths were 100 nm or larger. In the quest for QDs in the range of 10 nm or less, suitable for applications in QD lasers, more and more experimental groups in recent years are turning to the self-assembly of QDs.

5.2.1. *Lithographic patterning*

In the *deep-mesa etching* of QD arrays (figure 19(*a*)), one starts with the modulation-doped AlGaAs/GaAs heterostructure. Then an array of photoresist dots is prepared by holographic double exposure [123]. Next, rectangular deep grooves are etched all the way through the GaAs cap layer, the Si-doped AlGaAs layer, and the undoped AlGaAs spacer layer into the active GaAs layer. This results in quadratic dots with rounded corners.

The field-effect QD samples were created by again starting with the GaAs heterostructure. A Si-δ-doped layer in the GaAs is deposited at a distance of 330 nm from the AlGaAs/GaAs interface, which acts as a back contact to charge the dots. On top of the heterostructure, a periodic photoresist dot array is prepared by holographic lithography. The period is 500 nm and the lateral photoresist dot sizes are about half the period with a height of ~ 100 nm. An 8 nm thick semitransparent NiCr gate of 4 nm diameter is evaporated on to the photoresist structure. Away from the gate area the electron gas is removed by etching the AlGaAs. Contacts on the δ-doped back contact led researchers to confine the electrons under the photoresist dots and also vary the number of electrons [123, 124]. The results of Heitmann *et al.* [123] on far-infrared transmission spectroscopy of QD arrays in the presence of an external magnetic field are presented as an inset in figure 20.

The vertical QD was created by Tarucha *et al.* [125] in the device shown in figure 19(*c*). The device is in the shape of a round pillar. The QD in the device is a few hundred nanometres in diameter and has a thickness of ~ 10 nm. It is sandwiched between two non-conducting (AlGaAs) barrier layers. When a negative voltage
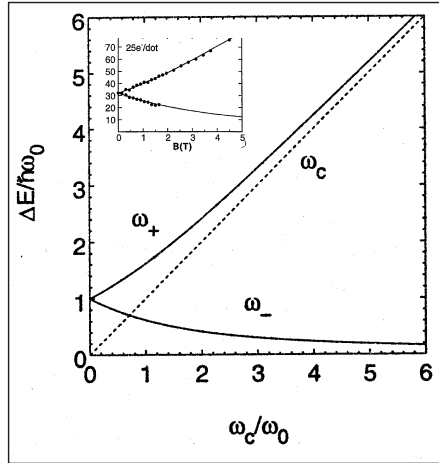
Figure 20. Dipole-allowed transition energies in the Fock–Darwin levels as a function of the applied magnetic field. In the limit of high magnetic fields, ω_+ approaches the cyclotron energy (dotted line) while ω_-, which corresponds to an edge mode, vanishes. Experimental results on the far-infrared resonance peaks versus the magnetic field [123] for QDs each containing 25 electrons are shown as an inset.

is applied to the metal that is wrapped around the pillar, the effective diameter of the dot is squeezed down to zero and as a consequence electrons leave the dot one by one.

5.2.2. *Self-assembled quantum dots*

For any practical observation of the effects of zero-dimensional confinement, one needs systems with typical sizes ~ 10 nm. In this respect, the process of lithographic patterning is not very useful because in this process the lateral QD walls are damaged and this seriously degrades the optical properties, especially when the QD dimension is ~ 10 nm. Self-assembly of the QDs (SAQDs), on the other hand, has proven to be very successful in obtaining nanostructures with dimensions even less than 10 nm, but with excellent zero-dimensional optical properties. These types of semiconductor QDs are fabricated by making use of strain-induced transformations that occur naturally during the epitaxial growth of lattice mismatched materials. In recent years, SAQDs have gained popularity because in this process well-defined QDs with sizes in the 10 nm range can be created. When a layer of semiconductor material is deposited on a substrate that has a smaller lattice constant, the growth is initially two dimensional (*wetting layer*). However, after a critical thickness of deposition, due to the presence of lattice strain, the layer can spontaneously transform to an array of three-dimensional islands (like the condensation of water droplets on a cold window), connected by the wetting layer. The dots are distributed within the plane of the wetting layer with a density of the order of 10^{10} cm^{-2}. They are remarkably uniform in size with their diameter fluctuating by $\sim 10\%$. Self-assembled QDs, such as In(Ga)As/GaAs, InP/GaInP, InAlAs/AlGaAs, InAs/InP, etc. grown by MBE have the expected zero-dimensional quantum structures [126].

The self-assembled InAs QDs generated by island growth are grown by MBE. The essential layer sequence of a device containing the SAQDs [127, 128] is sketched in figure 21. On a semi-insulating GaAs substrate with a suitable buffer of 20 nm thick n$^+$−doped Si (4×10^{18} cm^{-3}), a GaAs layer is grown and this serves as the
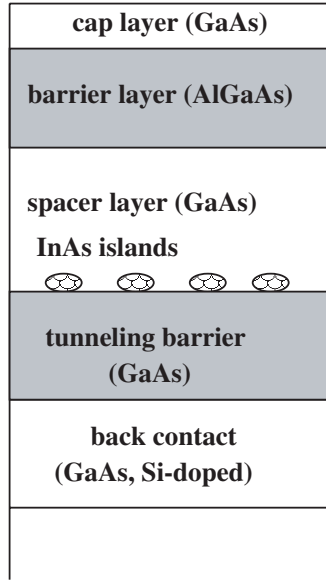
Figure 21.   Sketch of a device containing self-organized InAs quantum dots on GaAs.

back contact. On top of the undoped GaAs layer (thickness 50 nm) the InGaAs QDs are formed by growing a coherently strained InGaAs layer. The growth is interrupted when the islands form. The QD growth is followed by a thin GaAs layer, a thick AlGaAs layer ('blocking barrier') and a GaAs cap layer (figure 21). Interestingly, SAQDs have been recently modified during growth to create *nanoscopic rings* [129, 130]. FIR spectroscopy of these quantum rings revealed new modes predicted in earlier calculations [131–134].

5.3. *Shell filling in quantum dots*

In atomic physics, the chemical inertness and special stability of noble gases are explained by a mean-field approach that describes the motion of electrons bound to the three-dimensional spherically symmetric Coulomb potential of the nucleus. This potential around the atoms gives rise to the *shell structure* 1s, 2s, 2p, ... The shell filling is reflected by large maxima in the ionization energy for atomic numbers 2, 10, 18, ..., corresponding to noble gas atoms He, Ne, Ar, ... The mid-shell levels are filled according to Hund's rules, i.e. by maximizing the total electron spin for half-filled orbitals.

These electronic properties of real atoms can now be observed in semiconductor quantum dots. Impurity-free, well-defined and highly symmetric vertical quantum dots have been prepared in laboratories. These dots are so small that the dot size is comparable to the Fermi wavelength [104]. When a disk-shaped dot is laterally confined by a two-dimensional harmonic potential, the single-particle state has energy

$$E_{n,m} = (2n + |m| + 1)\hbar\omega_0,$$

where $n = 0, 1, 2, \ldots$ is the radial quantum number, $m = 0, \pm1, \pm2, \ldots$ is the angular momentum quantum number, and $\hbar\omega_0$ is the electrostatic confinement energy. Due
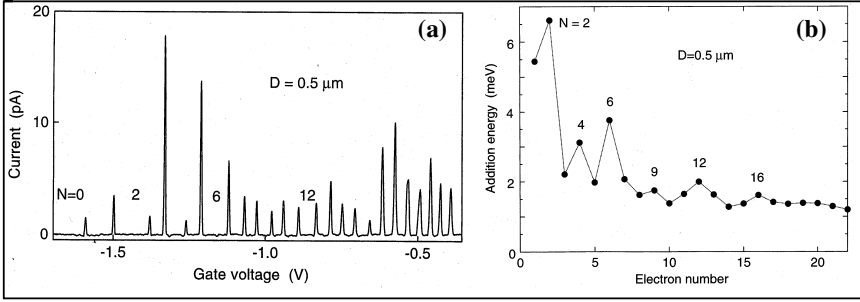
Figure 22.   (a) Current–voltage characteristic of a quantum dot with a diameter of 0.5 μm.
(b) Addition energy versus electron number in the dot [104].

to rotational symmetry of the system, these energy levels consist of sets of degenerate states that are separated by $\hbar\omega_0$ from each other. Each degenerate set can be regarded as a *shell* of an artificial atom. These states can be sequentially filled with non-interacting electrons. In the case of actual filling of electrons in the dot, this single-particle picture can be significantly modified by the electron–electron inter-action. However, if $\hbar\omega_0$ is greater than or comparable to the interaction energy, each set of degenerate states is sequentially filled by 2, 6, 12, 20, ... electrons. This sequence of electron numbers is very similar to that of atomic numbers in real atoms.

In 1996, Tarucha *et al.* [104] reported observation of Coulomb oscillations in a vertical dot (figure 19(c)). The oscillation period in their results shows a strong dependence on the number of electrons in the dot. The *addition energy*, $\mathcal{E}_{add} = \mu_{N+1} - \mu_N$, where $\mu_N = E_N - E_{N-1}$ is the chemical potential and E_N is the ground state energy of a QD with N electrons, as a function of electron number derived from figure 22(a), is shown in figure 22(b). The spacing between the current peaks in figure 22(a) reflects the energy required to add one electron in the dot. The addition energy curve shows strong peaks for 2, 6 and 12 electrons, as expected from the discussions above. However, there are also relatively large peaks for 4, 9 and 16 electrons, where the system has a stable *half-filled* shell, i.e. where electrons with only one type of spin fill the uppermost shell. Stable half-filled shells are not expected in a non-interacting picture of the dots [135]. A comprehensive review of these topics can be found in [136].

5.4. *Electron correlations: spin states*

Motivated by the results of Tarucha *et al.*, several theoretical studies of addition energy in QDs have been reported. Most of them are in good agreement with the experimental observations. The exact diagonalization method, first introduced in theoretical investigations of QDs by Maksym and Chakraborty [122], has been employed by Eto [137] for QDs in an external magnetic field and by Ezaki *et al.* [138, 139] without any magnetic field. The results are in line with the observations of Tarucha *et al.* Due to the presence of the Coulomb interaction, four-electron QDs have a spin-triplet ground state ($S_{total} = 1, S_z = -1, 0, 1$) and the observed weak peaks in the addition energy at $N = 4$ and 9 are interpreted as being due to a spin-polarized half-filled shell structure [137–140]. This is also in accordance with Hund's first rule that favours maximum-spin states for degenerate levels. Interestingly, for vertically coupled QDs, addition energy peaks at $N = 4, 9$ and 16 are conspicuously absent [141, 142]. The effects of electron correlations on the electronic states and the

conductance in vertically coupled dots have been investigated by Asano [143]. Coulomb oscillations in conductance, pairing of conductance peaks and spin blockade [144] in the weak-coupling regime of the dots, are found to be results of strong electron correlations. A three-dimensional description of the Coulomb interaction (parabolic potential in the electron plane and a finite-barrier quantum-well potential in the direction perpendicular to the plane) was found to be essential to determine single-electron conductance properties of realistic systems [145].

5.5. *Anisotropic dots*

When one breaks the circular symmetry in a QD by deforming the lateral confinement potential, the degeneracies of the single-particle levels present in a disk-shaped dot are lifted [146]. This destroys the shell structure observed in a circularly symmetric dot and modifies other atomic-like properties [147]. Even small deviations breaking the circular symmetry were found to have a dramatic effect. Exact diagonalization studies of Ezaki *et al.* [138, 139] revealed that in elliptical dots, the addition energy as a function of electron number in the dot does not exhibit any clear structure. Interestingly, in a triangular QD, Ezaki *et al.* found that there are stable states due to localization of electrons at the corners for 3, 6 and 9 electrons. In anisotropic parabolic QDs [148, 149], the calculated ground state is completely spin polarized up to 12 electrons, while the spin configuration of a small dot obeys Hund's rule. The calculated capacitance [150, 151], $C = e^2/[\mu(N) - \mu(N-1)]$, showed characteristic oscillation as a function of electron numbers: the local maximum corresponds to the closed-shell structure and the local minimum to the open-shell structure. The shell structure is also reflected in the calculated chemical potential.

5.6. *Influence of an external magnetic field*

The application of an external magnetic field perpendicular to the dot plane is a very powerful tool with which one can identify the quantum number of states in the quantum dots. The best way to begin describing the magnetic field effects is to introduce the Fock diagram.

5.6.1. *The Fock diagram*

The Schrödinger equation for an electron confined by a harmonic potential in the presence of an externally applied magnetic field was solved by Fock in 1928 [152, 12], and later by Darwin [153]. The energy eigenvalues in this case are given by

$$E_{nm} = (2n + |m| + 1)\hbar\Omega - \tfrac{1}{2}\hbar\omega_c \tag{16}$$

where $\Omega^2 = \left[\omega_0^2 + 1/4\omega_c^2\right]$, ω_0 is the frequency of the harmonic confinement potential and ω_c is the cyclotron frequency. The energies are plotted in figure 23 as a function of the magnetic field. In the limit of zero confinement these Fock–Darwin states approach the Landau states.

Dipole-allowed transitions among these energy levels will have energies

$$\Delta E_\pm = \hbar\Omega \pm \tfrac{1}{2}\hbar\omega_c \tag{17}$$

and are plotted in figure 20. Various experiments on QDs have been able to map the Fock–Darwin energy levels in the QDs. As an example, in figure 24 we present the results of magneto-tunnelling experiments by Schmidt [124] on double-barrier
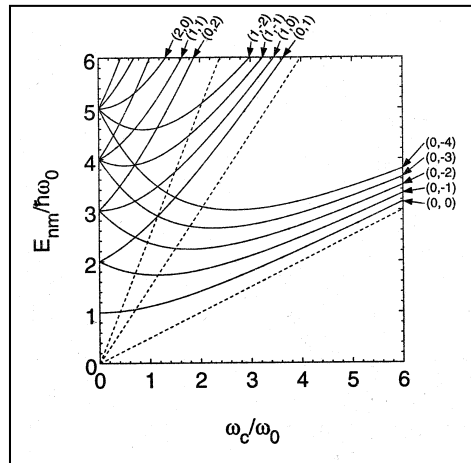
Figure 23.   Energy levels of the non-interacting electrons in a parabolic confinement
potential as a function of the applied magnetic field (Fock–Darwin levels). The dotted
lines denote the Landau level energies $(N + \frac{1}{2})\hbar\omega_c$, $N = 0, 1, 2, \ldots$.

resonant-tunnelling structures [12]. The grey-scale plot in figure 24 depicts the
differential conductance $G = \mathrm{d}I/\mathrm{d}V$, derived from the measured $I(V)$ characteristics
as a function of bias voltage and magnetic field (step 0.1 T). It is indeed fascinating
to observe how the energy spectrum of an *ideal* quantum mechanical model system
derived by Fock more than 70 years ago is now made visible in semiconductor
nanostructures.

5.6.2. *The no-correlation theorem*

The energy levels of many-electron (interacting) dots are quite complicated
because of the interplay between the confinement potential and the interelectron
interactions. Interestingly, experimentally observed far-infrared spectra were inde-
pendent of the electron number and clearly showed the relation given by figure 20
which is valid for non-interacting electrons. This puzzle was resolved by Maksym
and Chakraborty [122] who showed that, for a parabolically confined dot, the far-
infrared excites only the centre-of-mass motion of the system and the centre-of-mass
energy is identical to the single-electron energy E_{nm} [155].

This interesting result is strictly valid for a parabolic confinement potential.
The spectra deviate from figure 20 when the confinement potential is different from
a harmonic potential. That is the case, for example, when the couplings of the
neighbouring dots are taken into account, or the dots are created with other forms of
confinement potentials [12, 156, 157].

5.6.3. *Correlation effects and magic numbers*

Maksym and Chakraborty [122] were the first to point out that the interaction
between electrons in a QD subjected to an external magnetic field has a dramatic
effect on their energy spectrum. For a few electrons in a QD, numerical studies
indicated that physically observable ground states occur only at certain magic values
of the total angular momentum, which is a good quantum number in a circularly
symmetric dot. Therefore, as one sweeps the magnetic field, the system jumps from
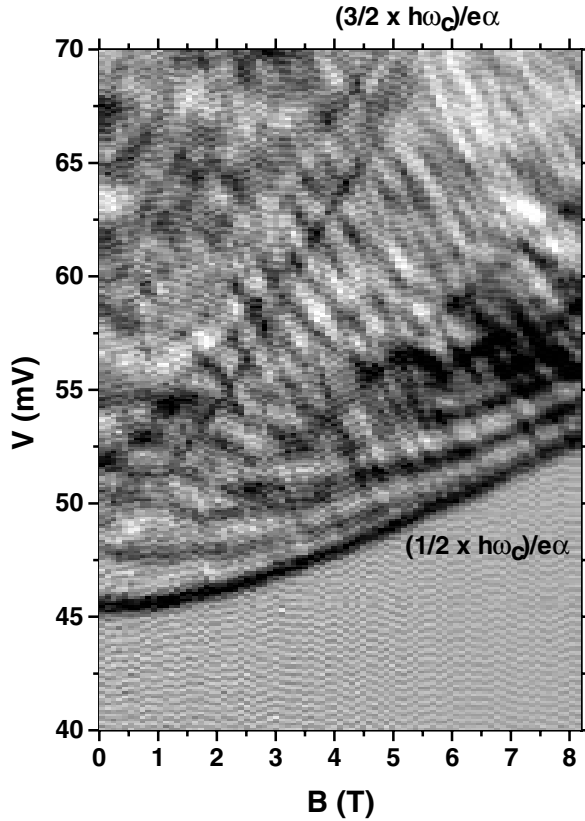one angular momentum ground state to another. This discrete jump leads to

Figure 24. Experimental determination of the Fock–Darwin energy levels: grey-scale plot of differential conductance as a function of magnetic field and bias voltage [124]. The location of the lowest Landau level energy ($\frac{1}{2}\hbar\omega_c$) and the second Landau level energy ($\frac{3}{2}\hbar\omega_c$) are also indicated.

oscillations in the thermodynamic properties of the dots as a function of the applied magnetic field. For example, theoretical studies indicated that in the low magnetic field regime, both the spin and angular momentum of the ground state vary discontinuously with magnetic field [158, 159]. At these particular values of the magnetic field, the low-temperature magnetization also varies discontinuously [158].

Going back to the non-interacting system, the Fock–Darwin states can be pictured as states localized on rings [160] whose radius R is given by

$$R^2 \sim 2\lambda^2(2n + |m| + 1)$$

where $\lambda = \hbar/2m^*\Omega$ sets the length scale. Large angular momentum therefore implies a large confinement energy and small angular momentum implies a large repulsive energy. The magic angular momenta are a consequence of the competition between these effects.

5.6.4. *Spin transitions*

Spin transitions in quantum dots deserve special mention here. They are a direct consequence of interacting electron states in a magnetic field. The spin transitions

were predicted by Maksym and Chakraborty [158] for three or four electrons in a parabolic quantum dot. Similar transitions in a two-electron QD were predicted independently by Wagner *et al.* [159]. Subsequently, experiments on capacitance [161] and tunnelling [162] provided evidence for the existence of such transitions.

5.7. *Quantum dots in novel systems*

In addition to the QDs described above, work on luminescence properties of semiconductor nanocrystals, and the so-called core-shell nanocomposites [163, 164], has seen very rapid developments. Recently, these nanocrystal QDs have found important applications in biology, where they are coupled to biological molecules for use in ultrasensitive biological detection at the single-dot level [112, 113].

Quantum dots have also been created in single-wall carbon nanotubes (CNs) [165–171]. Transport measurements on individual single-wall CNs have exhibited Coulomb blockade oscillations in linear conductance versus the gate voltage. Similarly, Coulomb diamonds are clearly observed in the differential conductance versus the gate voltage results. These are the clear signatures of the formation of QDs [12] in the nanotubes.

5.8. *Potential applications of quantum dots*

Although quantum dots initially emerged essentially as a laboratory for exploring fundamental phenomena in quantum mechanics, it was soon realized that these systems would have enormous application potential in our endless quest for miniaturization of electronic systems. After all, QDs represent the ultimate reduction in dimensionality of a semiconductor device. Interest in QDs stems from their potential to operate at the level of a single electron, which is certainly the limit for an electronic device. In what follows, we will briefly discuss some of the important applications of quantum dots that have already been achieved.

5.8.1. *Single-electron transistors (SETs)*

These are created to transfer individual electrons around a circuit at a well-defined rate [172–174]. An essential feature of the SET is the *Coulomb blockade* of single-electron tunnelling. This effect originates from the charging energy associated with transport of electrons to very small conducting islands. Coulomb blockade oscillations are observed as periodic resonance peaks in the conductance through these small islands, or quantum dots. Each peak corresponds to the addition of one electron to the dot (see section 5.3). These devices might find use in single-electron memory if the SET can be made to operate reliably at room temperature [172].

5.8.2. *Single-photon detectors*

SETs have been used recently to detect single photons in the infrared [175] and far-infrared [176] regions, and in the latter case, with unprecedented sensitivity. The FIR region covers the vibrational spectra of molecules in liquids and gases and therefore the single photon detector, which also measures the wavelength of the photon, turns out to be an important tool for FIR spectroscopy. An externally applied magnetic field was used to tune the energy so that when the cyclotron energy equals the photon energy, the photon is absorbed and an electron is excited into the higher energy level. The SET is used to detect that photo-excited electron.

Shields *et al.* [177] developed a single-photon detector based on quantum dot arrays to detect individual photons at visible or near-infrared wavelengths. Their

device was a GaAs/AlGaAs field-effect transistor containing a layer of InAs QDs separated from a 2DEG in the GaAs channel by a thin AlGaAs barrier. Charge carriers photo-excited by incident light are trapped by the dots which alters the conductivity of the 2DEG and is measured by the device.

5.8.3. *Single-photon emitters*

In classical light sources which usually contain a macroscopic number of emitters, the emitted photons obey Poisson statistics. However, creating a light source that will emit *one and only one* photon within a short time interval, on demand, is highly desirable in quantum information science [178]. For a secure key distribution in quantum cryptography, a single-photon light source is crucial. In order to demonstrate single-photon generation, various experimental groups have reported photon correlation measurements, in particular, the normalized second-order correlation function $g^{(2)}(\tau)$ defined by

$$g^{(2)}(\tau) = \langle I(t)I(t+\tau)\rangle / \langle I(t)\rangle^2$$

where $I(t)$ is the emission intensity at time t [179]. For a truly single-photon source, the correlation between successive photons emitted is zero at $\tau = 0$. This effect is known as antibunching. This is in contrast to the case of a coherent light source, where the correlation is independent of τ, and thermal (Gaussian) light, which shows an increase in correlation (bunching) at $\tau = 0$. Observations of photon antibunching have been reported in a wide variety of systems: single atoms [180] (resonance fluorescence of a low density vapor of Na atoms), a single trapped Mg^+ ion [181], single molecules [182], CdSe/ZnS nanocrystals [183], epitaxially grown self-assembled CdSe/Zn(S,Se) quantum dots for temperatures up to 200 K [184], a single nitrogen vacancy centre in diamond [185, 186], single-photon emission due to single electron–hole pairs photo-excited in a single quantum dot [187, 188], and most recently, in self-assembled QDs [189–194, 179]. A measured value of $g^{(2)}(0)$ as low as 0.05 has been reported [189], thereby making a strong case for self-assembled InAs QDs as ideal sources for single-photon emission.

5.8.4. *Quantum-dot lasers*

Semiconductor lasers have profoundly affected almost every aspect of our present-day life [195]. They are most commonly used in optical-data storage, optical communications, in CD players, as bar-code readers, laser printers, laser pointers, and in many other devices. In recent years, there has been very rapid progress in quantum-dot laser research [108]. They are of considerable contemporary interest because they offer the potential to yield superior properties compared to conventional bulk or quantum-well lasers [196, 197]. The atom-like density of states in quantum dots associated with strong confinement of electrons and holes have led to the expectation [196, 197] that there will be a great reduction of threshold current density which should also have a very weak temperature dependence. In addition, they would emit light at wavelengths that are not determined by the bandgap energy, but rather by the energy levels of the dots. This would offer the flexibility to tune the wavelength of the QD laser. Developments of self-organizing growth techniques that allow the formation of a high density of quantum dots with nanometre dimensions rapidly enhanced the development of QD laser research, where the performance is now comparable to that of quantum-well lasers [198, 199].

Using self-assembled quantum dots, low-threshold QD edge-emitting lasers have been fabricated [200]. Some of the milestones for QD laser achievements are:

– Room-temperature operation from a InGaAs/GaAs QD laser [201] emitting in the ground state at 1.31 μm wavelength with a threshold current density of 270 A/cm^2.
– Lasing in a InP/GaInP QD laser emitting in the visible part of the spectrum [202] (690–705 nm) with a threshold current density of 172 A/cm^2.
– High-power InGaAs QD laser operation at 1100 nm [203].
– QD vertical-cavity surface-emitting laser, using QDs in the active region, with room-temperature lasing operation [204].
– Inserting an InAs QD array in a InGaAs quantum well the QD emission wavelength can be controllably varied from 1.1 to 1.3 μm by changing the In content in the quantum well [205].
– High-performance QD lasers near 1.3 μm [206, 207] have a higher photoluminescence efficiency as compared to GaInNAs quantum wells [208].

The QD laser is a very active area of research [108, 209–212].

6. Quantum cascade transitions in quantum-dot structures

After a brief review of the properties of QDs and the physical properties of the QCT, we are now ready to discuss the nature of QCTs in a quantum-dot cascade structure (QDCS). In the following sections, we describe in detail the available theoretical results of the QCT in a cascade structure containing either rectangular or parabolic quantum dots in the active layers. The primary goal here is to explore the physical properties that might guide future experimental efforts. The main emphasis of these studies is the influence of the dot size and the number of electrons in the dot on luminescence spectra of a QDCS [213], with or without an applied magnetic field. One advantage of the quantum-dot cascade structure, for theoretical studies, over the quantum-well cascade structure is that, for few electrons in the QD, most of the physical properties can be calculated exactly, albeit numerically [12].

In section 6.5, we shall briefly discuss the experimental attempts reported so far on mid-infrared luminescence from devices that contain self-assembled QDs with or without a cascade scheme.

6.1. *Quantum dots versus quantum wells*

A quantum dot (QD) version of the QW cascade laser has been proposed by several authors [214–217] where theoretical estimates indicate that, unlike the QW cascade laser, non-radiative decay by phonon emission can be eliminated. Since the non-radiative rate of decay due to phonon emission in QWs is about 3000 times the radiative decay rate [1], elimination of phonon decay is vital for radiative efficiency. The essential difference between QD and QW lasers is that in the former system the excited and ground state electronic levels represent truly discrete states [12, 213], while in the latter each represents the bottom of a continuous band of states.

In the QDCS the rate of radiative decay may dominate the non-radiative rate. Since the excited and ground states of the coupled dots are discrete levels, non-radiative decays will involve emission of a phonon at the difference energy. In general, phonon energies form a continuous band so that such one-phonon decays are allowed. However, if the difference energy is larger than the largest phonon

energy (e.g. the optical phonon energy at $\hbar\omega_{LO} = 36\,\text{meV}$ in GaAs), then no single phonon can carry away all the electronic energy. Multiphonon decay processes are still allowed but the rate of these is negligible (except in certain narrow energy bands [218]). The dominant decay mechanism in dots can therefore be photon emission with a consequent enhancement in overall efficiency.

The size of each of the coupled dots is strongly constrained by the requirement that the energy difference between the excited and ground states exceeds the optical-phonon energy $\hbar\omega_{LO}$. Specifically, the energy difference between the two lowest states of one of the dots in isolation must exceed $\hbar\omega_{LO}$. The resulting maximum dot size L can be estimated from the energy spacing in a square well of size L:

$$\frac{3\pi^2\hbar^2}{2m^*L^2} > \hbar\omega_{LO}.$$

For GaAs, with an effective mass $m^* = 0.067m$, the above condition implies that dots need to be smaller than $L \simeq 20\,\text{nm}$ in all three dimensions [215].

It is expected that the LO-phonon-assisted relaxation time will be increased substantially if the electrons that are relaxing are confined in a quantum dot [22, 219]. One can then overcome the problem of radiative efficiency by replacing the QWs in the active region of a QC structure by quantum dots. It is also expected that the threshold current density of a QDCS would be orders of magnitude lower than that of a QW cascade structure (14 kA/cm^2 [1]). In addition, if kT is smaller than the level spacings in the dot, the lasing operation would be essentially temperature independent. As we mentioned above there were a few papers published earlier on QDCS [214–217]. The main aim of those papers, however, was to investigate the QDCS design and other device characteristics which would lead to improved efficiency of the lasing, rather than the physical properties of QDCSs. Little is known about the effect of quantum dots on the physical properties of the QCT. In the remaining sections, we present our current theoretical understanding of QDCSs and hope that this will motivate experimentalists to explore this system in the near future.

6.2. QCT with rectangular dots

In the theoretical model of a QDCS, we require that in addition to the confinement of electrons in the z-direction due to conduction band discontinuity, there is also confinement of electron motion in the plane. As we discussed in sections 5.3–5.5, the physics of quantum dots depends on the choice of confinement potentials. In this section we present the results for rectangular dots. The physics of the QCT in a system containing parabolic dots will be discussed in section 6.2. The single-electron Hamiltonian for rectangular confinement in a QDCS is

$$\mathcal{H}' = \frac{p_x^2}{2m^*} + \frac{p_y^2}{2m^*} + V_{\text{plane}}(x, y) + \frac{p_z^2}{2m^*} + V_{\text{conf}}(z) \tag{18}$$

where the confinement potential in the z-direction (figure 25) is given in equation (12), m^* is energy dependent due to band non-parabolicity, $m^* = m_e^*\left(1 + 2Em_e^*\gamma/\hbar^2\right)$, and U_0 is the conduction band discontinuity [213]. The eigenfunctions and eigenvalues of the single-electron Hamiltonian [18] are obtained from

$$\Psi_{nmk} = \varphi_{n,k}(x)\varphi_{m,k}(y)\chi_k(z)$$

where

$$\left[\frac{p_x^2}{2m^*} + V_{\text{plane}}(x)\right]\varphi_{n,k}(x) = E_n\varphi_{n,k}(x) \tag{19}$$

$$\left[\frac{p_z^2}{2m^*} + V_{\text{conf}}(z)\right]\chi_k(z) = \tilde{E}_k\chi_k(z)$$

$$E_{nmk} = E_{n,k} + E_{m,k} + \tilde{E}_k, \tag{20}$$

and $V_{\text{plane}}(x) = 0$ for $-L/2 < x < L/2$ and $V_{\text{plane}}(x) = U_0$ for $|x| > L/2$. Although $V_{\text{plane}}(x, y)$ is not equal to $V_{\text{plane}}(x) + V_{\text{plane}}(y)$ in the region $|x + y| > L$, the approximation $V_{\text{plane}}(x, y) = V_{\text{plane}}(x) + V_{\text{plane}}(y)$ makes only a small correction to the exact result for emission spectra. Because of the band non-parabolicity the electron mass depends on the total energy $m^*(E_{nmk})$. (In the calculations that follow, we consider only the main contribution due to $\tilde{E}_k$, i.e. the mass depends only on $\tilde{E}_k$ in equations (19) and (20). This approximation simplifies the analysis but will only result in small changes in the final energies.) In what follows, we consider only two subbands in the z-direction ($k = 1, 2$) and for a given k all possible states in the (x, y) plane with the condition $E_{nmk} < U_0$.

The solutions of equation (19) are the usual cos (sin)-type

$$\varphi_{n,k}(x) = \mathcal{N}\begin{cases} \begin{matrix}\cos\\\sin\end{matrix}\left(\sqrt{2m_{\text{w}}E_n}L/2\right) \\ \times e^{-\sqrt{2m_{\text{b}}(U_0-E_n)}(X-L/2)}, & x > L/2 \\ \begin{matrix}\cos\\\sin\end{matrix}\left(\sqrt{2m_{\text{w}}E_n}x\right), & |x| < L/2 \\ \begin{matrix}\cos\\-\sin\end{matrix}\left(\sqrt{2m_{\text{w}}E_n}L/2\right) \\ \times e^{-\sqrt{2m_{\text{b}}(U_0-E_n)}(X+L/2)}, & x < -L/2 \end{cases}$$

where $m_{\text{w}}(m_{\text{b}})$ is the electron effective mass in the well (barrier). The energy E_n was calculated numerically from

$$\tan\kappa = \sqrt{\frac{m_{\text{w}}}{m_{\text{b}}}}\sqrt{\frac{\gamma^2 - \kappa^2}{\kappa^2}}, \quad \text{for even solutions}$$

$$\tan\kappa = -\sqrt{\frac{m_{\text{b}}}{m_{\text{w}}}}\sqrt{\frac{\kappa^2}{\gamma^2 - \kappa^2}}, \quad \text{for odd solutions}$$

where $\kappa^2 = E_n(L^2/2)m_{\text{w}}$, $\gamma^2 = U_0(L^2/2)m_{\text{w}}$. Solutions of equation (20) are obtained numerically for the two lowest states (subbands) shown in figure 25. Due to the $x \leftrightarrow y$ symmetry, some of the levels are two-fold degenerate (for example, $E_{122} = E_{212}$).

From the single-electron basis functions, we construct the N-electron basis

$$\Phi_{n_i m_i k_i}(\mathbf{r}_1, \cdots, \mathbf{r}_N) = \mathcal{A}\,\Psi_{n_1 m_1 k_1}(\mathbf{r}_1)\sigma_1 \cdots \Psi_{n_N m_N k_N}(\mathbf{r}_N)\sigma_N \tag{21}$$

where, as usual, σ_i is the spin part of the wave function [$\sigma_i = \binom{1}{0}$ or $\binom{0}{1}$] and $\mathcal{A}$ is the antisymmetrization operator. The total many-electron Hamiltonian is written as
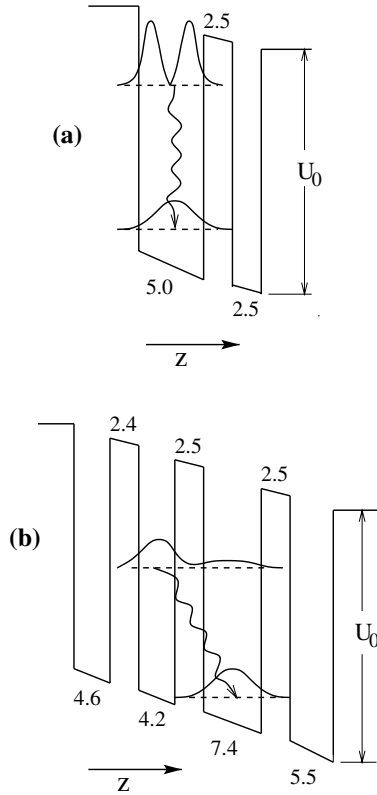
Figure 25. Energy band diagram (schematic) of the active region of a quantum cascade structure: (*a*) vertical lasing transition under an average applied electric field of 85 kV/cm and (*b*) diagonal transition under a field of 55 kV/cm. The relevant wave functions (moduli squared) as well as the quantum cascade transitions are also shown schematically. The numbers (in nm) are the well ($Ga_{0.47}In_{0.53}As$) and barrier ($Al_{0.48}In_{0.52}As$) widths. For vertical transitions, these parameters are taken from [216, 217]. Material parameters considered in this work are: electron effective mass m_e^* ($Ga_{0.47}In_{0.53}As$) = 0.043 m_0, m_e^*($Al_{0.48}In_{0.52}As$) = 0.078 m_0, conduction band discontinuity, $U_0 = 520$ meV, non-parabolicity coefficient, $\gamma_w = 1.3 \times 10^{-18}$ m^2 for the well and $\gamma_b = 0.39 \times 10^{-18}$ m^2 for the barrier [213].

$$\mathcal{H} = \sum_{i=1}^{N} \mathcal{H}'_i + \sum_{i<j}^{N} V(|\mathbf{r}_i - \mathbf{r}_j|) \tag{22}$$

where $\mathcal{H}'$ is given by equation (18). For interelectron interactions we consider the Coulomb interaction

$$V(|\mathbf{r}_i - \mathbf{r}_j|) = \frac{e^2}{\varepsilon|\mathbf{r}_i - \mathbf{r}_j|}, \tag{23}$$

where ε is the background dielectric constant. The Hamiltonian matrix is then calculated on that basis (21). The single-electron Hamiltonian makes only a diagonal contribution while the interaction term gives non-diagonal contributions

$$\langle n_{i_1} m_{i_1} k_{i_1}; n_{i_2} m_{i_2} k_{i_2} | V | n_{j_1} m_{j_1} k_{j_1}; n_{j_2} m_{j_2} k_{j_2} \rangle$$

$$= \mathrm{Tr}_\sigma \int \mathrm{d}\mathbf{r}_1 \mathrm{d}\mathbf{r}_2 \, \mathcal{A} \Big[\Psi^*_{n_{i_1} m_{i_1} k_{i_1}}(\mathbf{r}_1)\sigma_{i_1} \Psi^*_{n_{i_2} m_{i_2} k_{i_2}}(\mathbf{r}_2)\sigma_{i_2} \Big]$$

$$\times V(|\mathbf{r}_1 - \mathbf{r}_2|) \, \mathcal{A} \Big[\Psi^*_{n_{j_1} m_{j_1} k_{j_1}}(\mathbf{r}_2)\sigma_{j_1} \Psi^*_{n_{j_2} m_{j_2} k_{j_2}}(\mathbf{r}_1)\sigma_{j_2} \Big].$$

The eigenvalues and eigenfunctions were calculated by exact (numerical) diagonalization of the Hamiltonian matrix. As the many-body Hamiltonian also has $x \leftrightarrow y$ symmetry some of the states are two-fold degenerate.

In the initial state (before optical emission) all the electrons are in the second subband, $k = 2$. In the final state (after optical emission) one electron is in the first subband, $k = 1$, and all other electrons are in the second subband, $k = 2$. The intensity of optical transitions is found from the expression

$$\mathcal{I}_{if}(\omega) = \frac{1}{Z} \sum_{if} \delta(\omega - E_i + E_f) \bigg| \int \chi_1(z) \, z \, \chi_2(z) \, \mathrm{d}z \int \Phi^*_i(x_1 y_1, \cdots, x_N y_N)$$

$$\times \Phi_f(x_1 y_1, \cdots, x_N y_N) \, \mathrm{d}x_1 \, \mathrm{d}y_1 \cdots \mathrm{d}x_N \, \mathrm{d}y_N \bigg|^2 \exp(-\beta E_i) \qquad (24)$$

where $Z = \sum_i \mathrm{e}^{-\beta E_i}$ is the partition function and $\beta = 1/kT$. In all our computations, we take $T = 20$ K.

The energy levels and possible optical transitions for the non-interacting systems are sketched in figure 26. Clearly, there are two types of transitions for the non-interacting electron system: (a) from the one-particle ground state of the second subband to the one-particle ground state of the first subband, and (b) from the one-particle excited state of the second subband to the one-particle excited state of the first subband. These are the transitions between states with the same quantum number in the (x, y) plane. The energies of these transitions are different due to band non-parabolicity. The non-parabolicity can also allow transitions between states with different quantum numbers in the (x, y) plane but the intensity of these transitions is very small because the non-parabolicity has a small effect on the electron wave functions. Therefore, we can safely assume that the optical transitions are allowed only between states with the same quantum numbers in the (x, y) plane. One also notices from figure 26 that optical transitions to the ground state of the final non-interacting system are forbidden for $N > 2$.

6.2.1. *Vertical transitions*

In figure 27, the optical spectra are shown for vertical transitions (figure 25(a)) and for two sizes of quantum dots: $L = 20$ and 40 nm, and for different numbers of electrons in the quantum dot. In all these cases the first moment of the emission spectra for the interacting system is almost the same as that for the non-interacting system. This is because in the case of vertical transitions Coulomb interaction between the electrons in the second subband and those in the second and the first subbands is almost the same (electrons are localized in the same quantum well in the z-direction). The Coulomb interaction between electrons is about half the energy separation between the one-electron states in the (x, y) plane for $L = 20$ nm and is of the same order as the energy separation between xy levels for $L = 40$ nm. That is why
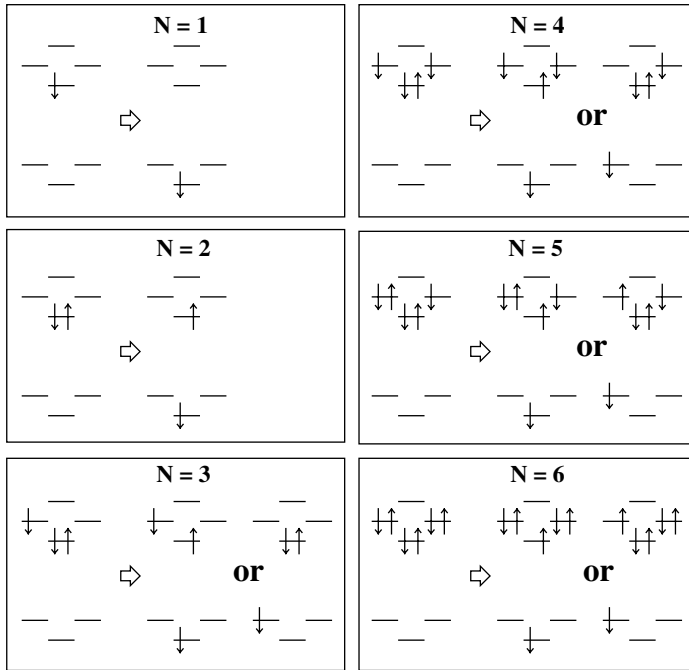
Figure 26. Energy levels and spin configurations and the allowed optical transitions (schematic) for quantum dots with non-interacting electrons. Here, ↑ denotes electrons with spin up and ↓ with spin down.

the interaction is more important for $L = 40$ nm. For the two-electron system there is a small blue-shift of the emission line due to the interaction which increases with an increase of the size of the quantum well. In addition, there is also a small red satellite at $L = 40$ nm. For the six-electron system, the interaction results in a redistribution of the intensities between peaks: the higher energy peak becomes more intense than that for the lower energy. For three, four and five electrons in a non-interacting system, we have a degenerate initial state. The degeneracy is lifted by the interaction and for the four-electron system the initial ground state is partially polarized as expected from Hund's rules. The interaction also results in the appearance of satellites and at the same time the separation between the main peaks becomes smaller for the interacting system than for the non-interacting case.

6.2.2. *Diagonal transitions*

In figure 28 optical spectra are presented for diagonal optical transitions (figure 25(*b*)) and for two sizes of quantum dots: $L = 10$ and 20 nm, and for different numbers of electrons. Interestingly, we notice the behaviour characteristics of fully filled shells for two and six electrons. The Coulomb interaction is about twice as small as the separations between shell levels in the (x, y) plane for $L = 20$ nm and about six times smaller for $L = 10$ nm. For the two-electron system, we have a single line for both non-interacting and interacting systems. For the six-electron system and $L = 10$ nm, the emission spectra have the same two-peak structure as that of the non-interacting system. For $L = 10$ nm there is a small redistribution of intensities between the peaks while there is an additional line for $L = 20$ nm. For two, three and four electrons in the dot, the interaction results in splitting of lines of the
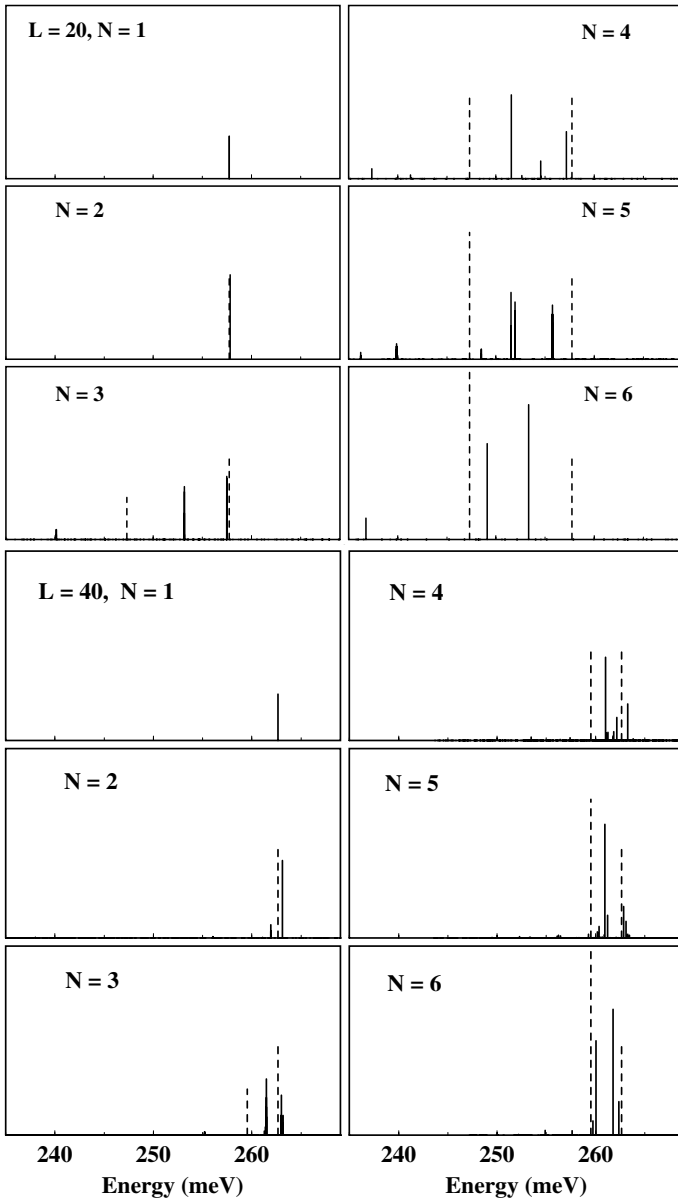
Figure 27.   Luminescence spectra of a quantum-dot cascade structure and *vertical* optical
         transitions for various values of the dot size (*L* in nm) and number of electrons (*N*) in
         the dot. The dashed lines correspond to luminescence of non-interacting electron
         systems [213].

corresponding non-interacting systems. With increasing size of the quantum dots the
lower-energy lines become more intense.

As the Coulomb interaction between electrons in the second subband is about
twice as large as the Coulomb interaction between electrons in the second and in the
first subbands we have a highly non-symmetric system and as a result there is a *large
blue-shift* in all cases, compared to the non-interacting system. This blue-shift
decreases with increasing size of the quantum dots. Further, the blue-shift increases
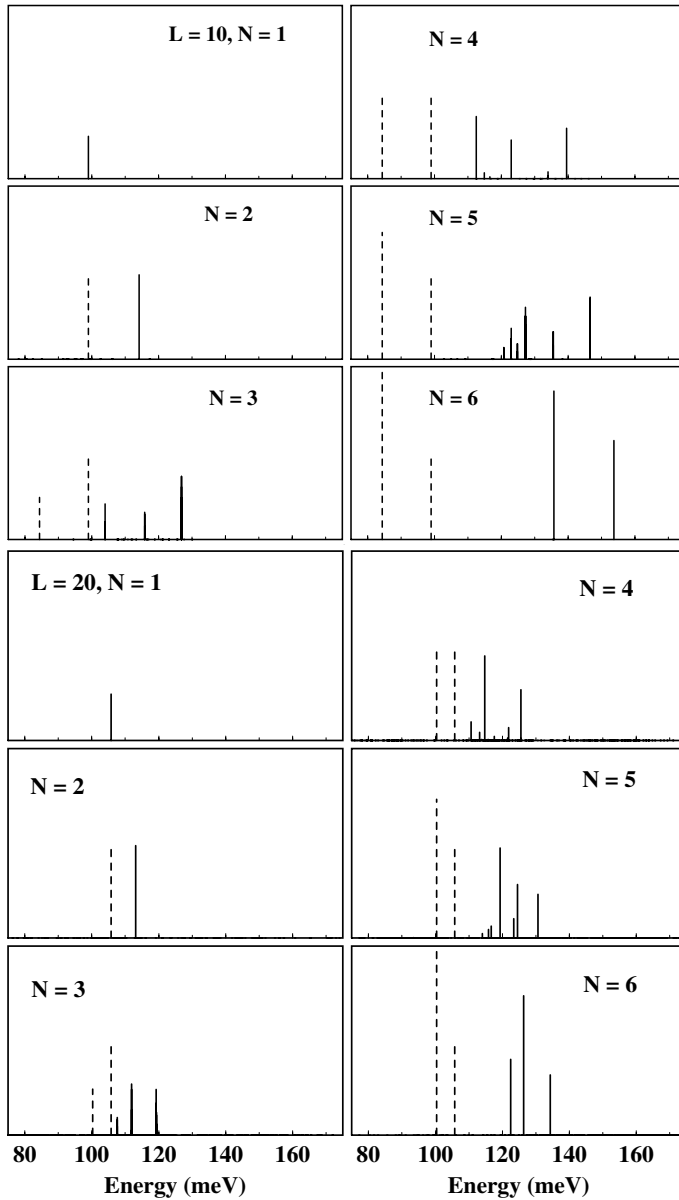
Figure 28. Luminescence spectra of a quantum-dot cascade structure and *diagonal* optical transitions for various values of the dot size (*L* in nm) and number of electrons (*N*) in the dot. The dashed lines correspond to luminescence of non-interacting electron systems [213].

with increasing number of electrons. For $L = 10$ nm, there is a blue-shift of the emission line of about 55 meV when the electron number is increased from one to six.

To summarize, the luminescence spectra of a quantum-dot cascade structure suitable for vertical or diagonal transitions reveal a lot of interesting properties that should be explored in future experiments. The spectra as a function of the dot size

and electron numbers in the dot reflect the atom-like character due to the presence of quantum dots. Most interestingly, a significant amount of blue-shift in the emission spectra can be achieved by increasing the electron population in the quantum dots as well as by decreasing the size of the dots. This is most clearly seen for the diagonal transitions. This opens up the possibility of tuning the emission frequency for diagonal transitions by changing the number of electrons in quantum dots and/or decreasing the size of the dots.

6.3. QCT in a parabolic dot

As mentioned above, most quantum dot studies to date are for a parabolic confinement potential (isotropic as well as anisotropic) that turned out to be more appropriate for observing the shell structure and the influence of shape and size of the dot on the electronic states. QD cascade structures, although not yet achieved in the laboratory, might be more efficient than present-day quantum-well cascade structures [215–217]. Knowledge of their physical properties might be useful in future development of this nanostructured light source.

The single-electron Hamiltonian for our system is the same as equation (18). All material parameters of our model of QDCS are given in figure 25(*b*), where we show one active region of the QC structure reported by Blaser *et al.* [80]. The structure emits at a wavelength of 10.5 μm, depending upon the electric field and temperature [80]. For our present work, details of the structure are not important and the most relevant system for us is the active region of figure 25(*b*). The confinement potential in the (x, y)-plane that creates the QDs is taken to be of the form

$$V_{\text{plane}}(x, y) = \tfrac{1}{2}m^*\left(\omega_x^2 x^2 + \omega_y^2 y^2\right) \tag{25}$$

where ω_x and ω_y are the confinement energies in the x- and y-directions, respectively, corresponding to the oscillator lengths $l_x = (\hbar/m^*\omega_x)^{1/2}$ and $l_y = (\hbar/m^*\omega_y)^{1/2}$. For an N-electron system, we also take into account the Coulomb interaction (equation (23)) between the electrons. We restrict the single-electron basis to 18 lowest states and numerically obtain the eigenstates of the N-electron system with $N = 2$–9. We analyse the shape, size and electron number dependence on the luminescence spectra of the QDCS.

For a non-parabolic quantum dot the degeneracy of the levels is lifted. The emission picture is shown schematically in figure 29. It is easy to see from the figure that for one and two electrons there is only one line, for three and four electrons the second line emerges, and for five and six electrons the emission spectra consists of three peaks. The separation between the lines is determined only by non-parabolicity.

Just like the shell filling of quantum dots discussed in sections 5.3–5.5, in our quantum-dot cascade structure we have also found peaks in addition energy as a function of the number of electrons [220]. In figure 30, addition energies of circular and elliptical dots are presented. For small circular quantum dots ($l_x = l_y = 5$ nm) there are sharp peaks at $N = 2$ and 6 as expected. There are also peaks at $N = 4$ and 9 where the total spin is equal to 1 and 3/2, respectively. Because these peaks result from the interelectron interaction their strength is much smaller than those at $N = 2$ and 4. Shell filling and Hund's rule peaks are also observed in the larger dot ($l_x = l_y = 10$ nm). For elliptical dots there are no peaks corresponding to Hund's rule ($N = 9$). All peaks in this case correspond to shell filling at even values of electron number ($N = 2$, 4, 6 and 8).
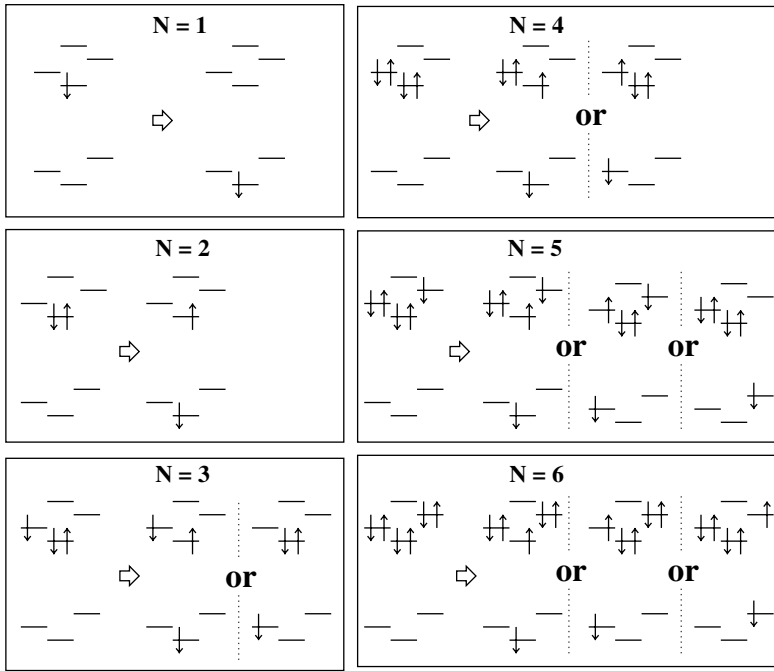
Figure 29. Energy levels and spin configurations and the allowed optical transitions (schematic) for quantum dots with non-interacting electrons in a parabolic QDCS. Here, ↑ denotes electrons with spin up and ↓ with spin down.

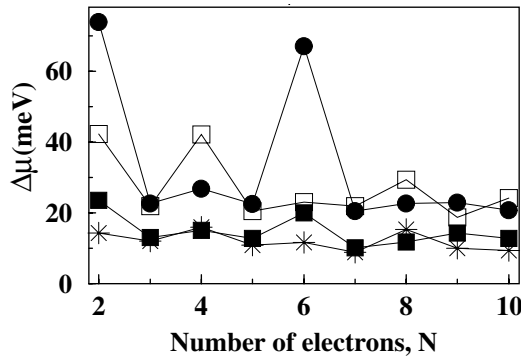Figure 30. Addition energies of circular and elliptical quantum dots in the QC structure. Here the symbols indicate: • for $l_x = l_y = 5$ nm, □ for $l_x = 5$ nm, $l_y = 7$ nm, ■ for $l_x = l_y = 10$ nm, ⋆ for $l_x = 10$ nm, $l_y = 14$ nm.

During the optical transition in the active region of a QDCS, in the initial state (before optical emission) all electrons are in the second subband. In the final state (after optical emission) one electron is in the first subband, and all other electrons are in the second subband. The intensity of optical transitions is calculated from equation (24). In all our computations, we take $T = 20$ K. To take into account disorder in the system we introduce the spreading of each emission line in the Lorentz form so that the final intensity is

$$\mathcal{I}(\omega) = \int d\omega_1 \mathcal{I}_{if}(\omega_1) \frac{\Delta}{\pi[\Delta^2 + (\omega - \omega_1)^2]}. \tag{26}$$

The parameter Δ in our calculation is taken to be $\Delta = 2\,\text{meV}$.

In figures 31 and 32, we present the luminescence spectra of our QC structures with circular and elliptic quantum dots with different numbers of electrons in the active region [220]. The emission spectra for the non-interacting system are shown by dotted lines. For smaller quantum dots the emission lines of the non-interacting system have some internal structure that is entirely due to the non-parabolicity. The non-parabolicity also gives a small red-shift to the emission line of the non-interacting system. For large quantum dots there is a single line for each number of electrons in the non-interacting system, because non-parabolicity in this case becomes less important due to the smaller values of confinement energies ω_x and ω_y. The electron–electron interaction results in a huge blue-shift of the emission spectra compared to the results for non-interacting electrons. The blue-shift becomes smaller for larger quantum dots and also decreases for elliptic dots. This is due to smaller interaction between the electrons when the spreading of the electron wave function in the (x, y) plane becomes larger. The interaction between the electrons also changes the shape of the emission line. This becomes more important for smaller quantum dots (figure 31). For larger quantum dots (figure 32) the disorder makes the emission line almost single-peaked, especially for large electron numbers when the interaction between the electrons becomes smaller.

It is also clear that for smaller quantum dots the change of the shape of the dots changes the shape of the emission line considerably. But for larger dots the shape of the emission line is less sensitive to the shape of the quantum dots and the line has almost a single peak both for circular and elliptic dots. Although the ground state of the electron system in the initial state obeys Hund's rule for circular dots (for $N = 4$ and 9) we did not find any singularity in emission spectra due to electron shell filling.

To summarize, the intersubband luminescence peaks of the QDC structure are rather insensitive to the shell effect of the QDs in the active region. For smaller (and circular) QDs, the peaks exhibit a huge blue-shift as the electron number is increased, which is entirely due to the electron–electron interaction. The blue-shift is smaller for larger and non-circular dots. For large dots, the shape of the emission line has a weak dependence on the shape of the quantum dots.

6.4. *Magnetic field effects on intersubband transitions*

Magnetic field effects on intersubband transitions in QDs embedded in a QC structure were investigated recently by us [221]. It should be pointed out that this effect differs significantly between quantum wells and quantum dots. For a quantum well in a perpendicular magnetic field, the subbands quantize into a ladder of Landau levels and only cyclotron transitions are possible (unless of course one applies a parallel field or a magnetic field that is tilted [17, 82] from the direction normal to the electron plane; see section 4.1.4). On the other hand, in quantum dots confinement and a magnetic field lead to Fock–Darwin energy levels at low fields [12, 13], and cyclotron transitions appear only at very high fields where the Fock–Darwin levels merge to form the Landau levels [12, 13, 152, 153] (see section 5.6.1).

We have considered the parabolically confined QDCSs described earlier. Accordingly, the single-electron Hamiltonian has the form

Figure 31. Luminescence spectra of a quantum cascade structure with circular ($l_x = l_y = 5$ nm) and elliptical ($l_x = 5$, $l_y = 7$ nm) quantum dots containing $N = 2$–9 electrons in the active region.

$$\mathcal{H}' = \mathcal{H}_z + \mathcal{H}_x + \mathcal{H}_y + \mathcal{H}_{xy}, \tag{27}$$

where

$$\mathcal{H}_x = \frac{p_x^2}{2m^*} + \frac{m^*}{2}\left(\omega_x^2 + \frac{1}{4}\omega_c^2\right)x^2,$$

$$\mathcal{H}_y = \frac{p_y^2}{2m^*} + \frac{m^*}{2}\left(\omega_y^2 + \frac{1}{4}\omega_c^2\right)y^2,$$

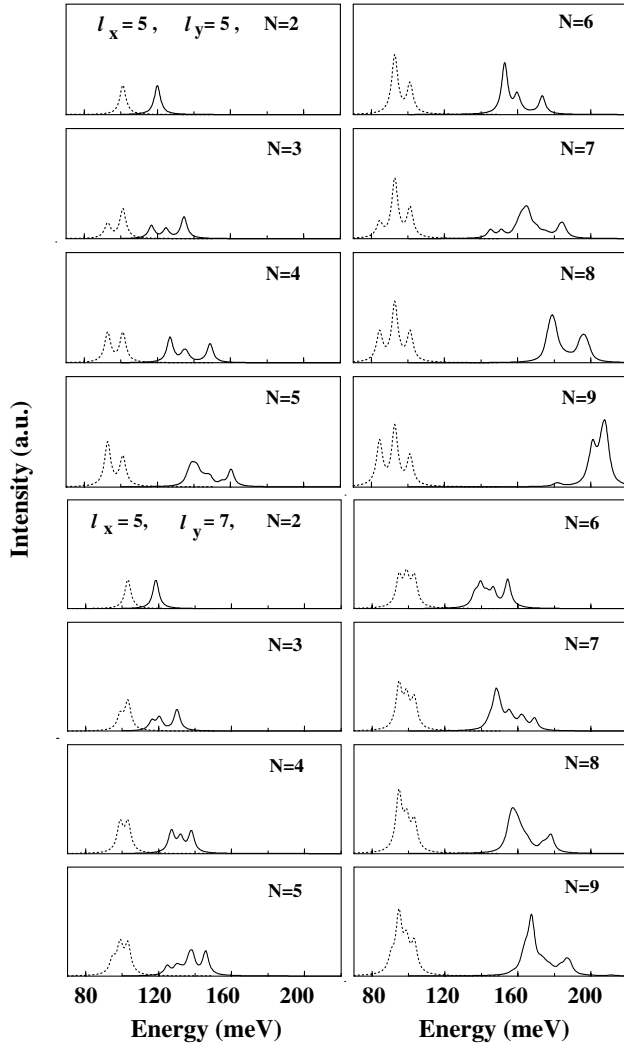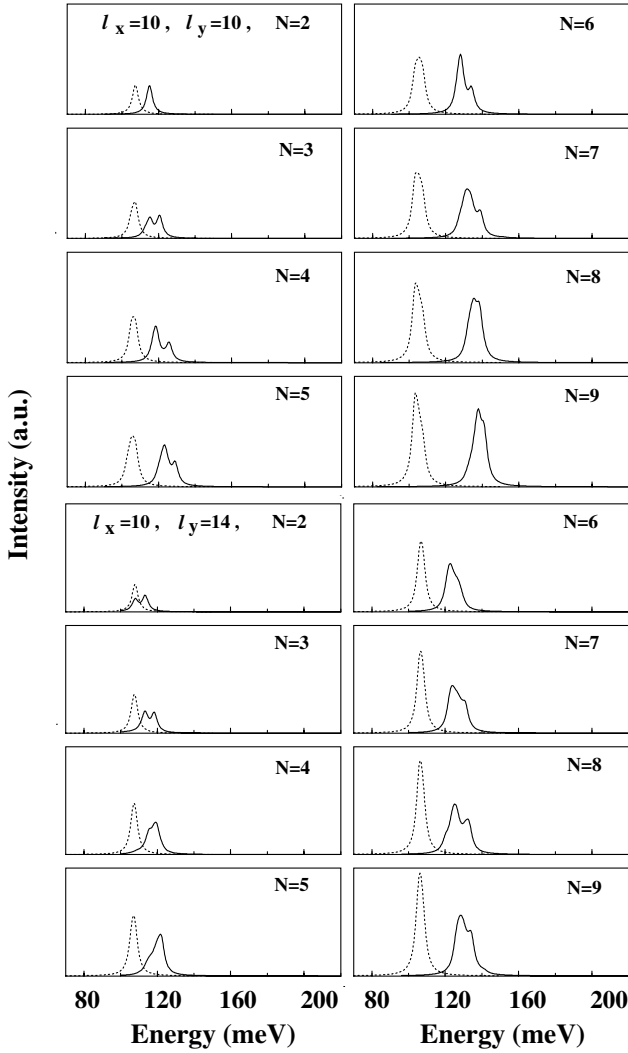$$\mathcal{H}_z = \frac{p_z^2}{2m^*} + V_{\mathrm{conf}}(z),$$

and

Figure 32. Luminescence spectra of a quantum cascade structure with circular ($l_x = l_y = 10$ nm) and elliptical ($l_x = 10$, $l_y = 14$ nm) quantum dots containing $N = 2$–9 electrons in the active region.

$$\mathcal{H}_{xy} = \tfrac{1}{2}\omega_c \big(xp_y - yp_x\big).$$

Here $\omega_c = eB/(m^*c)$ is the cyclotron frequency in a magnetic field B applied perpendicular to the QD plane (along the z-direction).

As a first step we calculate the eigenfunctions and eigenvalues of the single-electron Hamiltonian $\mathcal{H}_x + \mathcal{H}_y + \mathcal{H}_z$. The eigenfunctions are the product of eigenfunctions of corresponding one-dimensional Hamiltonians,

$$\Psi_{nmk} = \varphi_{x,n}(x)\varphi_{y,m}(y)\chi_k(z),$$

where $\varphi_{x,n}(x)$ and $\varphi_{x,n}(x)$ are eigenfunctions of harmonic oscillators with frequencies $(\omega_x^2 + \omega_c^2/4)^{1/2}$ and $(\omega_x^2 + \omega_c^2/4)^{1/2}$, respectively. The subband functions $\chi_k(z)$ are calculated numerically. Then for each subband k, we diagonalize the Hamiltonian

$\mathcal{H}_{xy}$ in a subspace $\varphi_{x,n}(x)\varphi_{y,m}(y)$, where n and m are less than 20. As a result, we find the eigenfunctions, $\Psi_{j,k}(x, y, z)$, and eigenstates, $E_{j,k}$, of the single-electron Hamiltonian (18). In our calculations that follow, we consider only two subbands in the z-direction ($k = 1, 2$) and for a given k all possible states in the xy-plane with the condition $E_{jk} < U_0$.

From the single-electron basis functions, we construct the N-electron (spinless) basis

$$\Phi_{n_i m_i k_i}(\mathbf{r}_1, \cdots, \mathbf{r}_N) = \mathcal{A}\, \Psi_{n_1 m_1 k_1}(\mathbf{r}_1) \cdots \Psi_{n_N m_N k_N}(\mathbf{r}_N) \tag{28}$$

where $\mathcal{A}$ is the antisymmetrization operator. The total many-electron Hamiltonian is written as

$$\mathcal{H} = \sum_{i=1}^{N} \mathcal{H}'_i + \sum_{i<j}^{N} V(|\mathbf{r}_i - \mathbf{r}_j|)$$

where $\mathcal{H}'$ is given by equation (27). For interelectron interactions we consider the Coulomb interaction $V(|\mathbf{r}_i - \mathbf{r}_j|) = e^2/\varepsilon|\mathbf{r}_i - \mathbf{r}_j|$, where ε is the background dielectric constant. The Hamiltonian matrix is then calculated in the basis (28). The eigenvalues and eigenfunctions were calculated by exact (numerical) diagonalization of the Hamiltonian matrix.

In the initial state (before optical emission) all electrons are in the second subband, $k = 2$. In the final state (after optical emission) one electron is in the first subband, $k = 1$, and all other electrons are in the second subband, $k = 2$. The intensity of optical transitions is calculated from equation (24).

In figure 33 the lowest energy gap of a circular ($l_x = l_y$) quantum dot containing two electrons is shown for different values of the oscillator strength and the magnetic field. Results in the left column correspond to a system of interacting electrons while those in the right column are for non-interacting systems. Similar results are also shown in figure 34 for elliptical quantum dots ($l_x \neq l_y$). From the analysis of the figures one can extract the following characteristic features of interacting systems:

(i) The effect of interaction on the energy spectra becomes more pronounced for larger quantum dots. This is due to the fact that compared to the typical interaction energy, the characteristic interlevel separation in the non-interacting system decreases more rapidly with increasing size of the quantum dot. In other words, this means that the ratio of the typical interaction energy to the typical interlevel separation in the non-interacting system increases with the size of the quantum dots.

(ii) At a given value of the magnetic field the interelectron interactions tend to suppress the excitation gaps. The strength of this suppression is a non-monotonic function of the magnetic field.

To analyse the luminescence spectra of quantum dot systems we consider one important characteristic of the optical spectra: the height of the emission line, i.e. the maximum of the emission line. In figure 35 the maximum of the emission spectra as a function of the applied magnetic field is shown for circular and elliptical quantum dots. Comparing figures 33–35 we can conclude that there are some correlations between energy spectra (more specifically, the energy gaps) and emission spectra (the maximum of the lines) in interacting quantum dot systems. (i) If the energy gaps
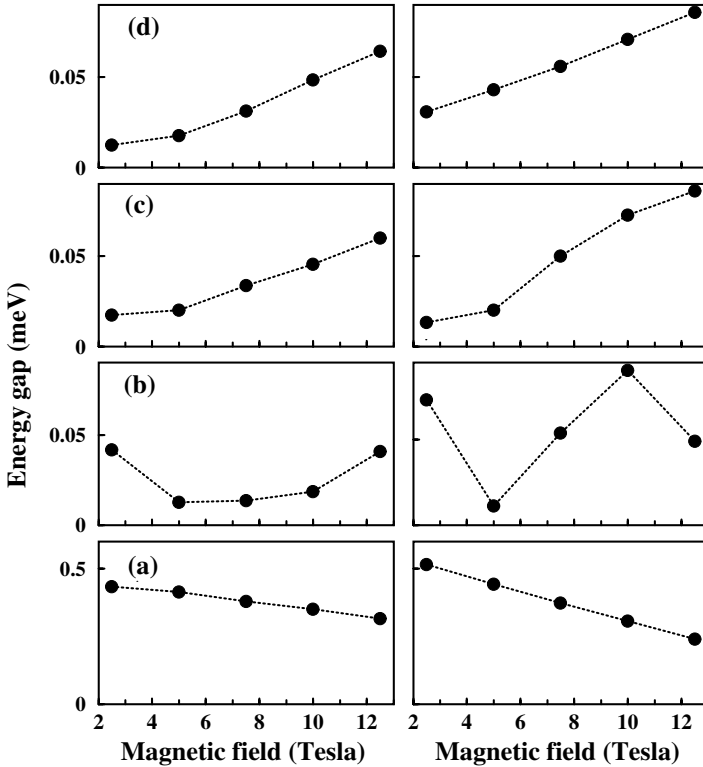
Figure 33.   Lowest energy gap of a two-electron circular ($l_x = l_y$) quantum dot versus the applied magnetic field. The quantum dot sizes (in nanometres) considered here are (5,5) (*a*), (10,10) (*b*), (15,15) (*c*) and (20,20) (*d*). The left column corresponds to interacting systems while the right one is for non-interacting systems.

are relatively large and, as a result, have a weak dependence on the magnetic field, then the emission spectra also weakly depend on the magnetic field. Indeed, for quantum dots of small size ($l_x = l_y = 5$ nm), the maximum of the emission lines is almost independent of the magnetic field (figure 35). This is in agreement with the energy spectra of a circular dot (figure 33(*a*)), where a large gap is present at all values of magnetic field. (ii) A non-monotonic dependence of the maximum of the emission line on the magnetic field is observed whenever the energy gap shows a strong non-monotonic dependence on the magnetic field. As an example, consider the formation of the cusp-like behaviour in the emission line (figure 35) at a magnetic field close to 5 T. This cusp is observed for a size of quantum dot of about 15 nm. Interestingly, there is a minimum of the energy gap at $B = 5$ T for the $l_x = 10$ nm, $l_y = 15$ nm system. This minimum corresponds to the minimum (cusp) in figure 35. At the same time the energy gap for a circular dot ($l_x = 10$ nm, $l_y = 10$ nm) has a weak dependence on the magnetic field which corresponds to the almost monotonic field dependence in figure 35. With a further increase in size of the dots the dependence of the energy gap on magnetic field becomes more monotonic and the cusps disappear.

To understand the correlation between the energy and emission spectra we should emphasize the specific feature of the system under consideration, which is that the main transitions are transitions between the ground state of the initial
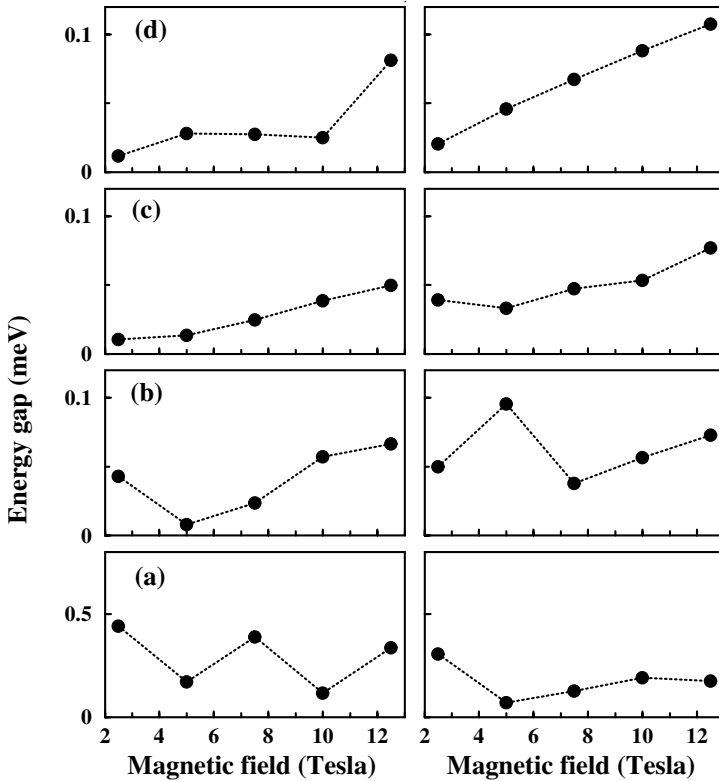
Figure 34. Lowest energy gap of a two-electron non-circular ($l_x \neq l_y$) quantum dot. The dot sizes (in nanometres) are: (5,10) (*a*), (10,15) (*b*), (15,20) (*c*) and (20,25) (*d*). The left column corresponds to interacting systems while the right one is for non-interacting systems.

system and the excited states of the final system. This can be seen from an analysis of the non-interacting system. For a non-interacting two-electron system, electrons in the initial state occupy the two lowest Fock–Darwin states (figure 36) (see also section 5.6) of the second subband. Transitions are allowed only to the excited state of the final system, where the electron in the second subband is in the ground Fock–Darwin state and the electron in the first subband is in the first excited Fock–Darwin state. The transition to the ground state, in which both electrons are in the ground Fock–Darwin state of the corresponding subband, is forbidden. This transition is allowed only due to the non-parabolicity of the energy spectra, and therefore its probability is very low. It is easy to show that the height of the emission peak for the non-interacting system does not depend on the magnetic field.

The interelectron interaction mixes the energy states both in the initial and in the final non-interacting systems. As a result the emission peak becomes broad and has a lower height compared to that for the non-interacting system. If the electron–electron interaction in the initial and in the final systems were the same then the antisymmetric many-electron states would be identical in the initial and the final systems, and as a result, the height of the emission peak would not depend on the magnetic field. In the present case, interactions between the electrons in the initial system (electrons are in the same subband) and in the final system (electrons are in
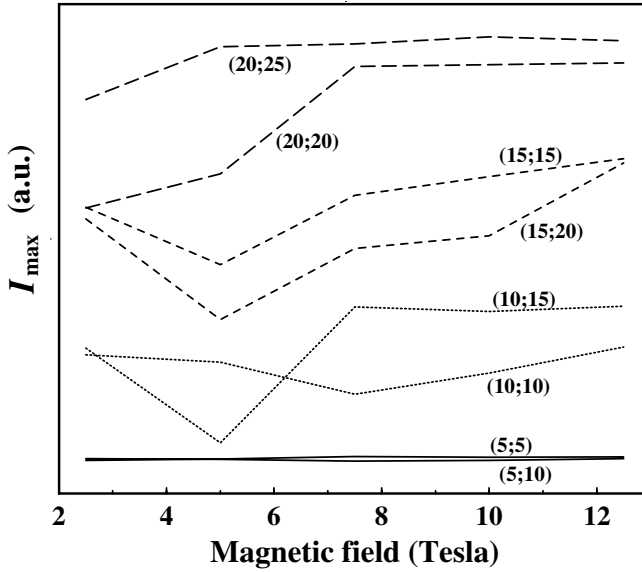
Figure 35.   The emission peak as a function of magnetic field for circular and non-circular
              quantum dots. The numbers next to the lines in the figure correspond to the size of
              the dot (l_x, l_y).

different subbands) are different. If this difference has a weak effect on the many-electron states then the height of the emission peak has a weak dependence on the magnetic field. Conversely, the height of the emission peak has a strong magnetic field dependence if the states of the many-electron system are very sensitive to the interelectron interaction. This sensitivity is partially determined by the energy gaps in the non-interaction system. This is the origin of the correlation between the emission peaks and energy spectra.

   To summarize, the calculated emission spectra for quantum dots containing a few interacting electrons embedded in a quantum cascade structure indicate that the behaviour of the emission peaks as a function of the applied magnetic field directly reflects the field dependence of the low-lying energy gap of the quantum dot structure.

6.5. *Mid-IR luminescence from a QD cascade device*

   As we discussed in earlier sections, electron energy levels in a QD are fully discrete and hence one exploits the optical transitions between conduction confined states or valence confined states. These transitions are usually referred to as intraband or intersublevel transitions [105, 127]. Mid-IR luminescence from inter-sublevel transitions in unipolar devices that contain self-assembled InAs quantum dots has been reported recently [222]. In these devices, the QDs were not expected to contain more than one electron, and were grown in a resonant tunnelling structure where electrons are injected into the excited QD state from one side while the other side of the resonant tunnelling structure contains a six-period superlattice of GaAs wells and AlGaAs barriers. The superlattice was designed to have two minibands and acts as an electron filter that prevents electrons from escaping from the dot. Before it can escape from the dot, an electron must first make a transition to a lower
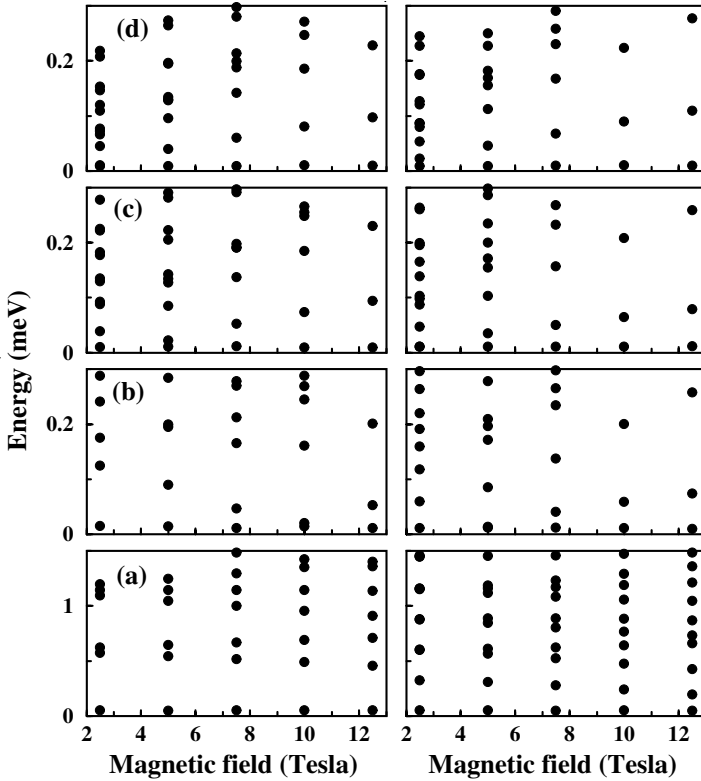
Figure 36. The Fock–Darwin energy spectra (see Section 5.6.1) of a two-electron quantum dot in the cascade structure (QDCS). The quantum dot sizes (in nanometres) considered here are (5,5) (*a*), (10,10) (*b*), (15,15) (*c*) and (20,20) (*d*). The left column corresponds to a circular dot while the right one is for a non-circular dot: (*a*) (5,10), (*b*) (10,15), (*c*) (15,20), and (*d*) (20,25).

state in the dot and if that state is aligned with the lower-energy miniband, it can tunnel out of the dot. Electroluminescence (EL) and photoluminescence (PL) experiments were performed on these devices to explore mid-IR photons generated from electron intersublevel transitions [222] occurring in the structure discussed above. The spectra from these two experiments indicate that different sizes of dots contribute to the two experiments: EL experiments involve smaller QDs with larger energy gaps, while larger dots contribute to the PL spectra. There was no cascading effect involved in this transition process. Mid-IR electroluminescence from a cascade of coupled GaAs quantum wells (in GaAs/AlGaAs) and self-assembled AlInAs quantum dot layers in the active region and injection superlattices [48] has also been reported [223]. This marks the beginning of experimental activities on the quantum-dot cascade structure.

7. Summary and open questions

The purpose of this review is to highlight the interesting physical aspects of quantum cascade transitions in nanostructured systems. Quantum engineering using

ultrathin semiconductor layers grown by molecular beam epitaxy allows one to design and observe quantum phenomena on a nanometre scale. The quantum cascade laser is a brilliant outcome of this quantum engineering in the rapidly developing field of nanoscale science and technology. Driven by several emerging real-world applications, QCL science and technology have been developing at a phenomenal rate. The wavelength tunability coupled with its high power (due to the cascade scheme) has made QCL a very useful tool for gas-sensing applications. Investigation of the physical properties of the QCT, which is the source for this laser, is truly fascinating. Theoretical studies indicate that the application of a magnetic field that is parallel, tilted or perpendicular to the electron plane causes novel transitions, or oscillations in tunnelling currents that are due to electron relaxation by emission of optical or acoustic phonons. Similarly, theoretical work on a quantum-dot cascade structure has shown its necessity in avoiding the major non-radiative relaxation mechanism for electrons, namely, LO-phonon emission. Theoretical investigations of the optical properties indicate a large blue-shift of the luminescence peak that is entirely due to electron–electron interaction within the dot. The luminescence is also influenced by the shape and size of the dot in the active region. In a magnetic field, the spectra reflect the behaviour of the low-lying excitations in a quantum dot. Given the rapid developments in quantum dot physics one expects that this new system will be fabricated in the near future.

Investigation of the physical properties of the QCT is still in its infancy. It should be amply evident from this review that several aspects of this unique transition need to be more thoroughly explored. These include:

– The role of disorder: a better quantitative account of the disorder effect is required in order to understand the observed absence of the expected red-shift when a magnetic field is applied parallel to the electron plane. More experimental work on these problems would be helpful in developing a more realistic theoretical picture of the potential fluctuations caused by the impurities.
– Theoretical work is needed on the role of various non-radiative mechanisms in the context of QCT. This might shed new light on various relaxation modes in analogous coupled quantum-well systems.
– New experiments on magnetic field effects (perpendicular as well as tilted) are required.

Finally, there is the challenge of placing ultrasmall quantum dots in the active regions of the QCL. The first such attempt that exploits intersublevel transitions in a device containing self-assembled QDs has already been reported and hopefully many more will follow. Theoretical results discussed here indicate a brilliant future for such a system with excellent tuning possibilities over a wide range of energy, by altering the shape, size and the number of electrons within the dot. Properties of quantum dots with or without an applied magnetic field seem to influence the quantum cascade transitions profoundly and would require further investigation.

In this review, we have not attempted to cover topics associated with the fabrication, design, efficiency and various other aspects of the laser. These and other topics can be found in several excellent articles by the inventors of this laser [14, 69, 70].

Acknowledgements

References

[1] FAIST, J., CAPASSO, F., SIVCO, D. L., SIRTORI, C., HUTCHINSON, A. L., and CHO, A. Y., 1994, *Science*, **264**, 553.

[2] FAIST, J., CAPASSO, F., SIRTORI, C., SIVCO, D. L., and SIVCO, A. Y., 2000, *Semiconductors and Semimetals*, **66**, 1.

[3] FAIST, J., CAPASSO, F., SIRTORI, C., SIVCO, D. L., HUTCHINSON, A. L., and CHO, A. Y., 1995, *Appl. Phys. Lett.*, **66**, 538.

[4] FAIST, J., CAPASSO, F., SIRTORI, C., SIVCO, D. L., HUTCHINSON, A. L., and CHO, A. Y., 1995, *Appl. Phys. Lett.*, **67**, 3057.

[5] FAIST, J., CAPASSO, F., SIVCO, D. L., HUTCHINSON, A. L., CHU, S. G., and CHO, A. Y., 1998, *Appl. Phys. Lett.*, **72**, 680.

[6] GMACHL, C., CAPASSO, F., TREDICUCCI, A., SIVCO, D. L., HUTCHINSON, A. L., and CHO, A. Y., 1998, *Electron Lett.*, **34**, 1103.

[7] FAIST, J., CAPASSO, F., SIRTORI, C., SIVCO, D. L., BAILLARGEON, J. N., HUTCHINSON, A. L., and CHO, A. Y., 1996, *Appl. Phys. Lett.*, **68**, 3680.

[8] FAIST, J., SIRTORI, C., CAPASSO, F., SIVCO, D. L., BAILLARGEON, J. N., HUTCHINSON, A. L., and CHO, A. Y., 1998, *IEEE Photon. Technol. Lett.*, **10**, 1100.

[9] GMACHL, C., FAIST, J., BAILLARGEON, J. N., CAPASSO, F., SIRTORI, C., SIVCO, D. L., CHU, S. N. G., and CHO, A. Y., 1997, *IEEE Photon. Technol. Lett.*, **9**, 1090.

[10] GMACHL, C., CAPASSO, F., FAIST, J., HUTCHINSON, A. L., TREDICUCCI, A., SIVCO, D. L., BAILLARGEON, J. N., CHU, S. N. G., and CHO, A. Y., 1998, *Appl. Phys. Lett.*, **72**, 1430.

[11] SLIVKEN, S., HUANG, Z., EVANS, A., and RAGEZHI, M., 2002, *Appl. Phys. Rev. Lett.*, **80**, 4091.

[12] CHAKRABORTY, T., 1999, *Quantum Dots* (Amsterdam: Elsevier).

[13] CHAKRABORTY, T., 1992, *Comments Condens. Matter Phys.*, **16**, 35.

[14] GMACHL, C., CAPASSO, F., SIVCO, D. L., and CHO, A. Y., 2001, *Rep. Prog. Phys.*, **64**, 1533.

[15] LEVINE, B. F., 1993, *J. Appl. Phys.*, **74**, R1.

[16] WANG, K. L., and KARUNASIRI, R. P. G., 1993, in *Semiconductor Quantum Wells, and Superlattices for Long-Wavelength Infrared Detectors*, M. O. Manasreh (Ed.) (Artech House).

[17] HELM, M., 2000, *Semiconductors, and Semimetals*, **62**, 1.

[18] WEST, L. C., and EGLASH, S. J., 1985, *Appl. Phys. Lett.*, **46**, 1156.

[19] CHALLIS, L. J., 1992, *Contemporary Phys.*, **33**, 111.

[20] ANDO, T., FOWLER, A. B., and STERN, F., 1982, *Rev. Mod. Phys.*, **54**, 437.

[21] BLOSS, W. L., 1989, *J. Appl. Phys.*, **66**, 3639.

[22] FERREIRA, R., and BASTARD, G., 1989, *Phys. Rev. B*, **40**, 1074.

[23] SEILMEIER, A., HÜBNER, H.-J., ABSTREITER, G., WEIMANN, G., and SCHLAPP, W., 1987, *Phys. Rev. Lett.*, **59**, 1345.

[24] TATHAM, M. C., RYAN, J. F., and FOXON, C. T., 1989, *Phys. Rev. Lett.*, **63**, 1637.

[25] FAIST, J., CAPASSO, F., SIRTORI, C., SIVCO, D. L., HUTCHINSON, A. L., CHU, S. N. G., and CHO, A. Y., 1993, *Appl. Phys. Lett.*, **63**, 1354.

[26] LEE, S.-C., and GALBRAITH, I., 1999, *Phys. Rev. B*, **59**, 15796.

[27] SLUTZKY, M., ENTIN-WOHLMAN, O., BERK, Y., and PALEVSKI, A., 1996, *Phys. Rev. B*, **53**, 4065.

[28] OBERLI, D. Y., WAKE, D. R., KLEIN, M. V., KLEM, J., HENDERSON, T., and MORKOÇ, H., 1987, *Phys. Rev. Lett.*, **59**, 696.

[29] LEE, S.-C., GALBRAITH, I., and PIDGEON, C. R., 1995, *Phys. Rev. B*, **52**, 1874.

[30] MURDIN, B. N., HEISS, W., LANGERAK, C. J. G. M., LEE, S.-C., GALBRAITH, I., STRASSER, G., GORNIK, E., HELM, M., and PIDGEON, C. R., 1997, *Phys. Rev. B*, **55**, 5171.

[31] DÜR, M., GOODNICK, S. M., and LUGLI, P., 1996, *Phys. Rev. B*, **54**, 17794.
[32] KÖHLER, R., IOTTI, R. C., TREDICUCCI, A., and ROSSI, F., 2001, *Appl. Phys. Lett.*, **79**, 3920.
[33] KÖHLER, R., TREDICUCCI, A., BELTRAM, F., BEERE, H. E., LINFIELD, E. H., DAVIES, A. G., RITCHIE, D. A., IOTTI, R. C., and ROSSI, F., 2002, *Nature*, **417**, 156.
[34] ROCHAT, M., AJILI, L., WILLENBERG, H., FAIST, J., BEERE, H., DAVIES, A. G., LINFIELD, E. H., and RITCHIE, D., 2002, *Appl. Phys. Lett.*, **81**, 1381.
[35] KAZARINOV, R. F., and SURIS, R. A., 1971, *Sov. Phys. Semicond.*, **5**, 707.
[36] CAPASSO, F., MOHAMMED, K., and CHO, A. Y., 1986, *IEEE J. Quantum Electron.*, **22**, 1853.
[37] FAIST, J., CAPASSO, F., SIVCO, D. L., HUTCHINSON, A. L., SIRTORI, C., CHU, S. N. G., and CHO, A. Y., 1994, *Appl. Phys. Lett.*, **65**, 2901.
[38] SIRTORI, C., CAPASSO, F., FAIST, J., and SCANDOLO, S., 1994, *Phys. Rev. B*, **50**, 8663.
[39] STRASSER, G., KRUCK, P., HELM, M., HEYMAN, J. N., HVOZDARA, L., and GORNIK, E., 1997, *Appl. Phys. Lett.*, **71**, 2892.
[40] LI, Y. B., COCKBURN, J. W., SKOLNICK, M. S., BIRKETT, M. J., DUCK, J. P., GREY, R., and HILL, G., 1997, *Electron. Lett.*, **33**, 1874.
[41] KRUCK, P., STRASSER, G., HELM, M., HVOZDARA, L., and GORNIK, E., 1998, *Physica E*, **2**, 449.
[42] GAUTHIER-LAFAYE, O., BOUCAUD, P., JULIEN, F. H., PRAZERES, R., GLOTIN, F., ORTEGA, J.-M., Thierry-MIEG, V., PLANEL, R., LEBURTON, J. P., and BERGER, V., 1997, *Appl. Phys. Lett.*, **70**, 3197.
[43] GAUTHIER-LAFAYE, O., JULIEN, F. H., CABARET, S., LOURTIOZ, J. M., STRASSER, G., GORNIK, E., HELM, M., and BOIS, P., 1999, *Appl. Phys. Lett.*, **74**, 1537.
[44] SIRTORI, C., KRUCK, P., BARBIERI, S., COLLOT, P., NAGLE, J., BECK, M., FAIST, J., and OESTERLE, U., 1998, *Appl. Phys. Lett.*, **73**, 3486.
[45] KEIGHTLEY, P. T., WILSON, L. R., COCKBURN, J. W., SKOLNICK, M. S., CLARK, J. C., GREY, R., HILL, G., and HOPKINSON, M., 2000, *Physica E*, **7**, 8.
[46] HVOZDARA, L., GIANORDOLI, S., STRASSER, G., SCHRENK, W., UNTERRAINER, K., GORNIK, E., MURTHY, CH. S. S. S., KRAFT, M., PUSTOGOW, V., and MIZAIKOFF, B., 2000, *Physica E*, **7**, 37.
[47] KRUCK, P., PAGE, H., SIRTORI, C., BARBIERI, S., STELLMACHER, M., and NAGLE, J., 2000, *Appl. Phys. Lett.*, **76**, 3340.
[48] PAGE, H., BECKER, C., ROBERTSON, A., GLASTRE, G., ORITZ, V., and SIRTORI, C., 2001, *Appl. Phys. Lett.*, **78**, 3529.
[49] HELM, M., and UNTERRAINER, K. (Eds), 2000, Proceedings of the Fifth International Conference on Intersubband Transitions in Quantum Wells, *Physica E*, **7**.
[50] CAPASSO, F., TREDICUCCI, A., GMACHL, C., SIVCO, D. L., HUTCHINSON, A. L., CHO, A. Y., and SCAMARCIO, G., 1999, *J. Selected Topics in Quant. Electron.*, **5**, 792.
[51] TREDICUCCI, A., CAPASSO, F., GMACHL, C., SIVCO, D. L., HUTCHINSON, A. L., CHO, A. Y., FAIST, J., and SCAMARCIO, G., 1998, *Appl. Phys. Lett.*, **72**, 2388.
[52] TREDICUCCI, A., GMACHL, C., CAPASSO, F., SIVCO, D. L., HUTCHINSON, A. L., and CHO, A. Y., 1999, *Appl. Phys. Lett.*, **74**, 638.
[53] STRASSER, G., GIANORDOLI, S., HVOZDARA, L., SCRENK, W., UNTERRAINER, K., and GORNIK, E., 1999, *Appl. Phys. Lett.*, **75**, 1345.
[54] ANDERS, S., SCHRENK, W., GORNIK, E., and STRASSER, G., 2002, *Appl. Phys. Lett.*, **80**, 1864.
[55] YANG, R. Q., YANG, B. H., ZHANG, D., LIN, C.-H., MURRY, S. J., WU, H., and PEI, S. S., 1997, *Appl. Phys. Lett.*, **71**, 2409.
[56] YANG, B. H., ZHANG, D., YANG, R. Q., LIN, C.-H., MURRY, S. J., and PEI, S. S., 1998, *Appl. Phys. Lett.*, **72**, 2220.
[57] BRADSHAW, J. L., YANG, R. Q., BRUNO, J. D., PHAM, J. T., and WORTMAN, D. E., 1999, *Appl. Phys. Lett.*, **75**, 2362.
[58] YANG, R. Q., BRUNO, J. D., BRADSHAW, J. L., PHAM, J. T., and WORTMAN, D. E., 2000, *Physica E*, **2**, 69.
[59] OLAFSEN, L. J., AIFER, E. H., VURGAFTMAN, I., BEWLEY, W. W., FELIX, C. L., MEYER, J. R., ZHANG, D., LIN, C.-H., and PEI, S. S., 1998, *Appl. Phys. Lett.*, **72**, 2370.
[60] OHTANI, K., and OHNO, H., 1999, *Appl. Phys. Lett.*, **74**, 1409.

[61] GMACHL, C., TREDICUCCI, A., SIVCO, D. L., HUTCHINSON, A. L., CAPASSO, F., and CHO, A. Y., 1999, *Science* **286**, 749.

[62] GMACHL, C., SIVCO, D. L., BAILLARGEON, J. N., HUTCHINSON, A. L., CAPASSO, F., and CHO, A. Y., 2001, *Appl. Phys. Lett.*, **79**, 572.

[63] ULBRICH, N., SCARPA, G., BÖHM, G., ABSTREITER, G., and AMANN, M.-C., 2002, *Appl. Phys. Lett.*, **80**, 4312.

[64] BORMANN, I., BRUNNER, K., HACKENBUCHNER, S., ZANDLER, G., ABSTREITER, G., SCHMULT, S., and WEGSCHEIDER, W., 2002, *Appl. Phys. Lett.*, **80**, 2260.

[65] ULRICH, J., KREUTER, J., SCHRENK, W., STRASSER, G., and UNTERRAINER, K., 2002, *Appl. Phys. Lett.*, **80**, 3691.

[66] IOTTI, R. C., and ROSSI, F., 2001, *Phys. Rev. Lett.*, **87**, 146603.

[67] CAPASSO, F., GMACHL, C., TREDICUCCI, A., HUTCHINSON, A. L., SIVCO, D. L., and CHO, A. Y., 1999, *Opt. Photonics News*, **10**, 31.

[68] GMACHL, C., CAPASSO, F., KOHLER, R., TRDICUCCI, A., HUTCHINSON, A. L., SIVCO, D. L., BAILLARGEON, J. N., and CHO, A. Y., 2000, *IEEE Circuits & Devices*, **16**, 10.

[69] CAPASSO, F., GMACHL, C., SIVCO, D. L., and CHO, A. Y., 1999, *Phys. World*, **12**, 27.

[70] CAPASSO, F., GMACHL, C., SIVCO, D. L., and CHO, A. Y., 2002, *Phys. Today*, MAY, p. 34.

[71] WEBSTER, C. R., FLESCH, G. J., SCOTT, D. C., SWANSON, J., MAY, R. D., WOODWARD, W. S., GMACHL, C., CAPASSO, F., SIVCO, D. L., BAILLARGEON, J. N., HUTCHINSON, A. L., and CHO, A. Y., 2001, *Appl. Opt.*, **40**, 321.

[72] BEWLEY, W. W., LEE, H., VURGAFTMAN, I., MENNA, R. J., FELIX, C. L., MARTINELLI, R. U., STOKES, D. W., GARBUZOV, D. Z., MEYER, J. R., MAIOROV, M., CONNOLY, J. C., SUGG, A. R., and OLSEN, G. H., 2000, *Appl. Phys. Lett.*, **76**, 256.

[73] LANE, B., WU, Z., STEIN, A., DIAZ, J., and RAZEGHI, M., 1999, *Appl. Phys. Lett.*, **74**, 3438.

[74] MENZEL, L., KOSTEREV, A. A., CURL, R. F., TITTEL, F. K., GMACHL, C. CAPASSO, F., SIVCO, D. L., BAILLARGEON, J. N., HUTCHINSON, A. L., CHO, A. Y., and URBAN, W., 2001, *Appl. Phys. B*, **72**, 859.

[75] MARTINI, R., GMACHL, C., FALCIGLIA, J., CURTI, F. G., BETHEA, C. G., CAPASSO, F., WHITTAKER, E. A., PAIELLA, R., TREDICUCCI, A., HUTCHINSON, A. L., SIVCO, D. L., and CHO, A. Y., 2001, *Electron. Lett.*, **37**, 191.

[76] BLASER, S., HOFSTETTER, D., BECK, M., and FAIST, J., 2001, *Electron. Lett.*, **37**, 778.

[77] BLANK, A., and FENG, S., 1993, *J. Appl. Phys.*, **74**, 4795.

[78] KASTALSKY, A., and EFROS, A. L., 1991, *J. Appl. Phys.*, **69**, 841.

[79] ULRICH, J., ZOBL, R., UNTERRAINER, K., STRASSER, G., and GORNIK, E., 2000, *Appl. Phys. Lett.*, **76**, 19.

[80] BLASER, S., DIEHL, L., BECK, M., and FAIST, J., 2000, *Physica E*, **7**, 33.

[81] APALKOV, V. M., and CHAKRABORTY, T., 2001, *Appl. Phys. Lett.*, **78**, 697.

[82] APALKOV, V. M., and CHAKRABORTY, T., 2001, *Appl. Phys. Lett.*, **78**, 1973.

[83] BEINVOGL, W., KAMGAR, A., and KOCH, J. F., 1976, *Phys. Rev. B*, **14**, 4274.

[84] WARBURTON, R. J., GAUER, C., WIXFORTH, A., KOTTHAUS, J. P., BRAR, B., and KROEMER, H., 1996, *Superlattices, and Microstructures*, **19**, 365.

[85] BLASER, S., 2001, private communication.

[86] DIEHL, L., 1999, Diploma Thesis, University of Neuchâtel.

[87] SCHÖL, E. (Ed.), 1998, *Theory of transport properties of semiconductor nanostructures* (Dordrecht: Kluwer Academic Publishers).

[88] CHAKRABORTY, T., and PIETILÄINEN, P., 1995, *The Quantum Hall Effects*, 2nd edn (New York: Springer).

[89] ANDO, T., 1979, *Phys. Rev. B*, **19**, 2106.

[90] BEINVOGL, W., and KOCH, J. F., 1978, *Phys. Rev. Lett.*, **40**, 1736.

[91] CLARK, R. G., HAYNES, S. R., SUCKLING, A. M., MALLETT, J. R., WRIGHT, P. A., HARRIS, J. J., and FOXON, C. T., 1989, *Phys. Rev. Lett.*, **62**, 1536.

[92] EISENSTEIN, J. P., STÖRMER, H. L., PFEIFFER, L., and WEST, K. W., 1989, *Phys. Rev. Lett.*, **62**, 1540.

[93] CEPERLEY, D. M., and ALDER, B. J., 1980, *Phys. Rev. Lett.*, **45**, 566.

[94] SMIRNOV, D., LE'OTIN, J., DRACHENKO, O., GALIBERT, J., PAGE, H., and SIRTORI, C., 2001 *Physica B*, **298**, 348.

[95] SMIRNOV, D., DRACHENKO, O., LEOTIN, J., PAGE, H., BECKER, C., SIRTORI, C., APALKOV, V., and CHAKRABORTY, T., 2002, *Phys. Rev. B*, **66**, 125317.

[96] NAJDA, S. P., TAKEYAMA, S., MIURA, N., PFEFFER, P., and ZAWADZKI, W., 1989, *Phys. Rev.* **40**, 6189.

[97] BECKER, C., SIRTORI, C., DRACHENKO, O., RYLKOV, V., SMIRNOV, D., and LEOTIN, J., 2002, *Appl. Phys. Lett.*, **81**, 2941.

[98] GANTMAKHER, V. F., and LEVINSON, Y. B., 1987, *Carrier Scattering in Metals, and Semiconductors* (Amsterdam: North-Holland).

[99] BENEDICT, K. A., HILLS R. K., and MELLOR, C. J., 1999, *Phys. Rev. B*, **60**, 10984.

[100] MAKSYM, P. A., 1992, in *High Magnetic Fields in Semiconductor Physics III*, edited by G. Landwehr (Springer).

[101] MORI, N., and ANDO, T., 1989, *Phys. Rev. B*, **40**, 6175.

[102] BOCKELMANN, U., and BASTARD, G., 1990, *Phys. Rev. B*, **42**, 8947.

[103] SMIRNOV, D., BECKER, C., DRACHENKO, O., RYLKOV, V. V., PAGE, H., LEOTIN, J., and SIRTORI, C., 2002, *Phys. Rev. B*, **66**, 121305 (R).

[104] TARUCHA, S., AUSTING, D. G., HONDA, T., VAN DER HAGE, R., and KOUWENHOVEN, L. P., 1997, JPN. *J. Appl. Phys.*, **36**, part I, 3917.

[105] MAIMON, S., FINKMAN, E., BAHIR, G., SCHACHMAN, S. E., GARCIA, J. M., and PETROFF, P. M., 1998, *Appl. Phys. Lett.*, **73**, 2003.

[106] JIMENEZ, J. L., FONSECA, L. R. C., BRADY, D. J., LEBURTON, J. P., WOHLERT, D. E., and CHENG, K. Y., 1997, *Appl. Phys. Lett.*, **71**, 3558.

[107] KIM, S., MOHSENI, H., ERDTMANN, M., MICHEL, E., JELEN, C., and RAZEGHI, M., 1998, *Appl. Phys. Lett.*, **73**, 963.

[108] GRUNDMANN, M., 2000, *Physica E*, **5**, 167.

[109] BIMBERG, D., GRUNDMANN, M., and LEDENTSOV, N. N., 1999, *Quantum Dot Heterostructures* (Wiley).

[110] YUSA, G., and SAKAKI, H., 1997, *Appl. Phys. Lett.*, **70**, 345.

[111] FINLEY, J. J., SKALITZ, M., ARZBERGER, M., ZRENNER, A., BÖHM, G., and ABSTREITER, G., 1998, *Appl. Phys. Lett.*, **73**, 2618.

[112] BRUCHEZ JR., M., MORONNE, M., GIN, P., WEISS, S., and ALIVISATOS, A. P., 1998, *Science* **281**, 2013.

[113] CHAN, W. C. W., and NIE, S., 1998, *Science* **281**, 2016.

[114] LUNDSTROM, T., SCHOENFELD, W., LEE, H., and PETROFF, P. M., 1999, *Science* **286**, 2312.

[115] SCHOENFELD, W. V., LUNDSTROM, T., PETROFF, P. M., and GERSHONI, D., 1999, *Appl. Phys. Lett.*, **74**, 2194.

[116] WELKER, M., KNÜPFER, B., MALZER, S., DÖHLER, G. H., GULDEN, K. H., MOSER, M., and RIEL, P., 1997, *Appl. Phys. Lett.*, **71**, 3561.

[117] LOSS, D., and DIVINCENZO, D. P., 1998, *Phys. Rev. A*, **57**, 120.

[118] MOLOTKOV, S. N., and NAZIN, S. S., 1996, *JETP Lett.*, **63**, 687.

[119] WEISBUCH, C., and VINTER, B., 1991, *Quuantum Semiconductor Structure* (Academic Press).

[120] DAVIES, J. H., 1998, *The Physics of Low-Dimensional Semiconductors* (Cambridge University Press).

[121] KELLY, M. J., and NICHOLAS, R. J., 1985, *Rep. Prog. Phys.*, **48**, 1702.

[122] MAKSYM, P. A., and CHAKRABORTY, T., 1990, *Phys. rev. Lett.*, **65**, 108.

[123] GUDMUNDSSON, V., BRATAAS, A., GRAMBOW, P., MEURER, B., KURTH, T., and HEITMANN, D., 1995, *Phys. Rev. B*, **51**, 17744.

[124] KOTTHAUS, J., and HEITMANN, D., 1993, *Phys. Today*, JUNE, p. 56.

[125] TARUCHA, S., AUSTING, D. G., HONDA, T., VAN DER HAGE, R. J., and KOUWENHOVEN, L. P., 1996, *Phys. Rev. Lett.*, **77**, 3613.

[126] LEONARD, D., KRISHNAMURTHY, M., REAVES, C. M., DENBAARS, S. P., and PETROFF, P. M., 1993, *Appl. Phys. Lett.*, **63**, 3203.

[127] MEDEIROS-RIBEIRO, G., LEONARD, D., and PETROFF, P. M., 1995, *Appl. Phys. Lett.*, **66**, 1767.

[128] MILLER, B. T., HANSEN, W., MANUS, S., LUYKEN, R. J., LORKE, A., KOTTHAUS, J. P., HUANT, S., MEDEIROS-RIBEIRO, G., and PETROFF, P. M., 1997, *Phys. Rev. B*, **56**, 6764.
[129] LORKE, A., and LUYKEN, R. J., 1998, *Physica B*, **256**, 424.
[130] LORKE, A., LUYKEN, R. J., GOVOROV, A. O., KOTTHAUS, J. P., GARCIA, J. M., and PETROFF, P. M., 2000, *Phys. Rev. Lett.*, **84**, 2223.
[131] HALONEN, V., PIETILINEN, P., and CHAKRABORTY, T., 1996, *Europhys. Lett.*, **33**, 377.
[132] NIEMELÄ, K., PIETILÄINEN, P., HYVÖNEN, P., and CHAKRABORTY, T., 1996, *Europhys. Lett.*, **36**, 533.
[133] CHAKRABORTY, T., and PIETILÄINEN, P., 1989, *Phys. Rev. B*, **39**, 7971.
[134] CHAKRABORTY, T., and PIETILÄINEN, P., 1990, *Phys. Rev. B*, **41**, 10862.
[135] KOUWENHOVEN, L. P., OOSTERKAMP, T. H., TARUCHA, S., AUSTING, D. G., and HONDA, T., 1998, *Physica B*, **249-251**, 191.
[136] KOUWENHOVEN, L. P., AUSTING, D. G., and TARUCHA, S., 2001, *Rep. Prog. Phys.*, **64**, 701.
[137] ETO, M., 1997, *Jpn. J. Appl. Phys.*, **36**, 3924.
[138] EZAKI, T., MORI, N., and HAMAGUCHI, C., 1997, *Phys. Rev. B*, **56**, 6428.
[139] EZAKI, T., SUGUMOTO, Y., MORI, N., and HAMAGUCHI, C., 1998, *Physica B*, **249-251**, 238.
[140] TANAKA, Y., and AKERA, H., 1997, *J. Phys. Soc. Jpn.*, **66**, 15.
[141] AUSTING, D. G., HONDA, T., MURAKI, K., TOKURA, Y., and TARUCHA, S., 1998, *Physica B*, **249-251**, 206.
[142] TAMURA, H., 1998, *Physica B*, **249-251**, 210.
[143] ASANO, Y., 1998, *Phys. Rev. B*, **58**, 1414.
[144] WEINMANN, D., HAUSLER, W., and KRAMER, B., 1995, *Phys. Rev. Lett.*, **74**, 984.
[145] RONTANI, M., ROSSI, F., MANGHI, F., and MOLINARI, E., 1998, *Appl. Phys. Lett.*, **72**, 957.
[146] MADHAV, A. V., and CHAKRABORTY, T., 1994, *Phys. Rev. B*, **49**, 8163.
[147] AUSTING, D. G., SASAKI, S., TARUCHA, S., REIMANN, S. M., KOSKINEN, M., and MANNINEN, M., 1999, *Phys. Rev. B*, **60**, 11514.
[148] FUJITO, M., NATORI, A., and YASUNAGA, H., 1996, *Phys. Rev. B*, **53**, 9952.
[149] NATORI, A., SUGIMOTO, Y., and FUJITO, M., 1997, *Jpn J. Appl. Phys.*, **36**, 3960.
[150] MACUCCI, M., HESS, K., and IAFRATE, G. J., 1993, *Phys. Rev. B*, **48**, 17354.
[151] MACUCCI, M., 1997, *Physica E*, **1**, 7.
[152] FOCK, V., 1928, *Z. Physik*, **47**, 446.
[153] DARWIN, C. G., 1930, *Proc. Cambridge Philos. Soc.*, **27**, 86.
[154] SCHMIDT, T., 1997, Dissertation, Max Planck Institute, Stuttgart.
[155] PEETERS, F. M., 1990, *Phys. Rev. B*, **42**, 1486.
[156] DEMEL, T., HEITMANN, D., GRAMBOW, P., and PLOOG, K., 1990, *Phys. Rev. Lett.*, **64**, 788.
[157] CHAKRABORTY, T., HALONEN, V., and PIETILÄINEN, P., 1991, *Phys. Rev. B*, **43**, 14289.
[158] MAKSYM, P. A., and CHAKRABORTY, T., 1992, *Phys. Rev. B*, **45**, 1947.
[159] WAGNER, M., MERKT, U., and CHAPLIK, A. V., 1992, *Phys. Rev. B*, **45**, 1951.
[160] MAKSYM, P. A., 1993, *Physica B*, **184**, 385.
[161] ASHOORI, R. C., STORMER, H. L., WEINER, J. S., PFEIFFER, L. N., BALDWIN, K. W., and WEST, K. W., 1993, *Phys. Rev. Lett.*, **71**, 613.
[162] SU, B., GOLDMAN, V. J., and CUNNINGHAM, J. E., 1992, *Phys. Rev. B*, **46**, 7644.
[163] YOFFE, A. D., 2001, *Adv. Phys.*, **50**, 1.
[164] ALIVISATOS, A. P., 1995, *MRS Bull.*, **20**, 23.
[165] TANS, S. J., DEVORET, M. H., DAI, H., THESS, A., SMALLEY, R. E., GEERLIGS, L. J., and DEKKER, C., 1997, *Nature*, **386**, 474.
[166] COBDEN, D. H., BOCKRATH, M., CHOPRA, N. G., ZETTL, A., McEUEN, P. L. RINZLER, A., THESS, A., and SMALLEY, R. E., 1998, *Physica B*, **249-251**, 132.
[167] CHICO, L., SANCHO, M. P. L., and MUNOZ, M. C., 1998, *Phys. Rev. Lett.*, **81**, 1278.
[168] KONG, J., ZHOU, C., YENILMEZ, E., and DAI, H., 2000, *Appl. Phys. Lett.*, **77**, 3977.
[169] PARK, J., and McEUEN, P. L., 2001, *Appl. Phys. Lett.*, **79**, 1363.
[170] ISHIBASHI, K., SUZUKI, M., IDA, T., and AOYAGI, Y., 2001, *Appl. Phys. Lett.*, **79**, 1864.
[171] NYGARD, J., and COBDEN, D. H., 2001, *Appl. Phys. Lett.*, **79**, 4216.
[172] THORNTON, T. J., 1994, *Rep. Prog. Phys.*, **57**, 311.

[173] KOUWENHOVEN, L. P., MARCUS, C. M., McEUEN, P. L., TARUCHA, S., WESTERVELT, R. M., and WINGREEN, N. S., 1997, in *Mesoscopic Electron Transport*, edited by SOHN, L. L. *et al.* (Dordrecht: Kluwer).

[174] KLEIN, D. L., ROTH, R., LIM, A. K., ALIVISATOS, A. P., and McEUEN, P. L., 1997, *Nature*, **389**, 699.

[175] CLELAND, A. N., ESTEVE, D., URBINA, C., and DEVORET, M. H., 1992, *Appl. Phys. Lett.*, **61**, 2820.

[176] KOMIYAMA, S., ASTAFIEV, O., ANTONOV, V., KUTSUWA, T., and HIRAI, H., 2000, *Nature*, **403**, 405.

[177] SHIELDS, A. J., O'SULLIVAN, M. P., FARRER, I., RITCHIE, D. A., HOGG, R. A., LEADBEATER, H. L., NORMAN, C. E., and PEPPER, M., 2000, *Appl. Phys. Lett.*, **76**, 3673.

[178] BOUWMEESTRE, D., EKERT, A., and ZEILINGER, A., 2000, *The Physics of Quantum Information* (Springer).

[179] CHAKRABORTY, T., PEETERS, F., and SIVAN, U. (Eds.), 2002, *Nano-Physics & Bio-Electronics: A New Odyssey* (Amsterdam: Elsevier), Chapter 4.

[180] KIMBLE, H. J., DAGENAIS, M., and MANDEL, L., 1977, *Phys. Rev. Lett.*, **39**, 691.

[181] DIEDRICH, F., and WALTHER, H., 1987, *Phys. Rev. Lett.*, **58**, 203.

[182] BASCHE, T., MOERNER, W. E., ORRIT, M., and TALON, H., 1992, *Phys. Rev. Lett.*, **69**, 1516.

[183] MICHLER, P., IMAMOGLU, A., MASON, M. D., CARSON, P. J., STROUSE, G. F., and BURATTO, S. K., 2000, *Nature*, **406**, 968.

[184] SEBALD, K., MICHLER, P., PASSOW, T., HOMMEL, D., BACHER, G., and FORCHEL, A., 2002, *Appl. Phys. Lett.*, **81**, 2920.

[185] KURTSIEFER, C., MAYER, S., ZARDA, P., and WEINFURTER, H., 2000, *Phys. Rev. Lett.*, **85**, 290.

[186] BROURI, R., BEVERATOS, A., POIZAT, J.-P., and GRANGIER, P., 2000, *Opt. Lett.*, **25**, 1294.

[187] SANTORI, C., PELTON, M., SOLOMON, G., DALE, Y., and YAMAMOTO, Y., 2001, *Phys. Rev. Lett.*, **86**, 1502.

[188] ZWILLER, V., BLOM, H., JONSSON, P., PANEV, N., JEPPESEN, S., TSEGAYE, T., GOOBAR, E., PISTOL, M. E., SAMUELSON, L., and BJÖRK, G., 2001, *Appl. Phys. Lett.*, **78**, 2476.

[189] BECHER, C., KIRAZ, A., MICHLER, P., IMAMOGLU, A., SCHOENFELD, W. V., PETROFF, P. M., ZHANG, L., and HU, E., 2001, *Phys. Rev. B*, **63**, 121312.

[190] MICHLER, P., KIRAZ, A., BECHER, C., SCHOENFELD, W. V., PETROFF, P. M., ZHANG, L., HU, E., and IMAMOGLU, A., 2000 *Science* **290**, 2282.

[191] BECHER, C., KIRAZ, A., MICHLER, P., SCHOENFELD, W. V., PETROFF, P. M., ZHANG, L., HU, E., and IMAMOGLU, A., 2002, *Physica E*.

[192] YUAN, Z., KARDYNAL, B. E., STEVENSON, R. M., SHIELDS, A. J., LOBO, C. J., COOPER, K., BEATTLE, N. S., RITCHIE, D. A., and PEPPER, M., 2002, *Science* **295**, 102.

[193] STEVENSON, R. M., THOMPSON, R. M., SHIELDS, A. J., FARRER, I., LOBO, C. J., RITCHIE, D. A., LEADBEATER, M. L., and PEPPER, M., 2002, *Physica E*.

[194] THOMPSON, R. M., STEVENSON, R. M., SHIELDS, A. J., FARRER, I., LOBO, C. J., RITCHIE, D. A., LEADBEATER, M. L., and PEPPER, M., 2001, *Phys. Rev. B*, **64**, 201302.

[195] ALFEROV, ZH. I., 1996, *Physica Scripta T*, **68**, 32.

[196] ARAKAWA, Y., and SAKAKI, H., 1982, *Appl. Phys. Lett.*, **40**, 939.

[197] ASADA, M., MIYAMOTO, Y., and SUEMATSU, Y., 1986, *IEEE J. Quantum Electron.*, QE-**22**, 1915.

[198] MANZ, Y. M., SCHMIDT, O. G., and EBERL, K., 2000, *Appl. Phys. Lett.*, **76**, 3343.

[199] MUKAI, K., NAKATA, Y., OTSUBO, K., SUGAWARA, M., and YOKOYAMA, N., 2000, *Appl. Phys. Lett.*, **76**, 3349.

[200] KIRSTAEDTER, N., LEDENTSOV, N. M., GRUNDMANN, M., BIMBERG, D., USTINOV, V. M., RUVIMOV, S. S., MAXIMOV, M. V., KOP'EV, P. S., ALFEROV, ZH. I., RICHTER, U., WERNER, P., GÖSELE, U., and HEYDENREICH, J., 1994, *Electron. Lett.*, **30**, 1416.

[201] HUFFAKER, D. L., PARK, G., ZOU, Z., SHCHEKIN, O. B., and DEPPE, D. G., 1998, *Appl. Phys. Lett.*, **73**, 2564.

[202] RIEDL, T., FEHRENBACHER, E., HANGLEITER, A., ZUNDEL, M. K., and Eberl. K., 1998, *Appl. Phys. Lett.*, **73**, 3730.

[203] HEINRICHSDORFF, F., RIBBAT, Ch., GRUNDMANN, M., and BIMBERG, D., 2000, *Appl. Phys. Lett.*, **76**, 556.

[204] SAITO, H., NISHI, K., OGURA, I., SUGOU, S., and SUGIMOTO, Y., 1996, *Appl. Phys. Lett.*, **69**, 3140.

[205] USTINOV, V. M., MALEEV, N. A., ZHUKOV, A. E., KOVSH, A. R., EGOROV, A. YU., LUNEV, A. V., VOLOVIK, B. V., KRESTNIKOV, I. L., MUSIKHIN, YU. G., BERT, N. A., KOP'EV, P. S., ALFEROV, ZH. I., LEDENTSOV, N. N., and BIMBERG, D., 1999, *Appl. Phys. Lett.*, **74**, 2815.

[206] QIU, Y., GOGNA, P., FOROUHAR, S., STINTZ, A., and LESTER, L. F., 2001, *Appl. Phys. Lett.*, **79**, 3570.

[207] SHCHEKIN, O. B., and DEPPE, D. G., 2002, *Appl. Phys. Lett.*, **80**, 3277.

[208] MARKUS, A., FIORE, A., GANIERE, J. D., OESTERLE, U., CHEN, J. X., DEVEAUD, B., ILEGEMS, M., and RIECHERT, H., 2002, *Appl. Phys. Lett.*, **80**, 911.

[209] HARRIS, L., MOWBRAY, D. J., SKOLNICK, M. S., HOPKINSON, M., and HILL, G., 1998, *Appl. Phys. Lett.*, **73**, 969.

[210] GRUNDMANN, M., WEBER, A., GOEDE, K., USTINOV, V. M., ZHUKOV, A. E., LEDENSTOV, N. N., KOP'EV, P. S., and ALFEROV, ZH. I., 2000, *Appl. Phys. Lett.*, **77**, 4.

[211] SELLIN, R. L., RIBBAT, CH., GRUNDMANN, M., LEDENTSOV, N. N., and BIMBERG, D., 2001, *Appl. Phys. Lett.*, **78**, 1207.

[212] LINDER, K. K., PHILLIPS, J., QASAIMEH, O., LIU, X. F., KRISHNA, S., BHATTACHARYA, P., and JIANG, J. C., 1999, *Appl. Phys. Lett.*, **74**, 1355.

[213] APALKOV, V. M., and CHAKRABORTY, T., 2001, *Appl. Phys. Lett.*, **78**, 1820.

[214] LEE, S. J., and KHURGIN, J. B., 1996, *Appl. Phys. Lett.*, **69**, 1038.

[215] WINGREEN, N. S., and STAFFORD, C. A., 1997, *IEEE J. Quantum Electron.*, **33**, 1170.

[216] HSU, C. F., O, J. S., ZORY, P. S., and BOTEZ, D., 1997, *Proc. SPIE*, **3001**, 271..

[217] HSU, C. F., O, J. S., ZORY, P. S., and BOTEZ, D., 2000, *IEEE J. Select. Topics Quantum Electron.*, **5**, 491.

[218] INOSHITA, T., and SAKAKI, H., 1994, *Solid-State Electron.*, **37**, 1175.

[219] HEITZ, R., KALBURGE, A., XIE, Q., GRUNDMANN, M., CHEN, P., HOFFMANN, A., MADHUKAR, A., and BIMBERG, D., 1998, *Phys. Rev. B*, **57**, 9050.

[220] APALKOV, V. M., and CHAKRABORTY, T., 2002, *Physica E*, **14**, 294.

[221] CHAKRABORTY, T., and APALKOV, V. M., 2002, *Physica E*, **16**, 253.

[222] WASSERMAN, D., and LYON, S. A., 2002, *Appl. Phys. Lett.*, **81**, 2848.

[223] ULBRICH, N., BAUER, J., SCARPA, G., BOY, R., SCHUH, D., ABSTREITER, G., SCHMULT, D., and WEGSCHEIDER, W., 2003, to be published